UCLA
UCLA Electronic Theses and Dissertations

Title
Cross Amyloid interfaces of Amyloid Beta

Permalink
https://escholarship.org/uc/item/8f31v82p

Author
Griner, Sarah Lorraine

Publication Date
2019

Peer reviewed|Thesis/dissertation

eScholarship.org Powered by the California Digital Library
University of California

UNIVERSITY OF CALIFORNIA

Los Angeles

Cross Amyloid interfaces of Amyloid Beta

A dissertation submitted in partial satisfaction of the

requirements for the degree Doctor of Philosophy

in Biochemistry & Molecular Biology

by

Sarah Lorraine Griner

2019

© Copyright by

Sarah Lorraine Griner

2019

ABSTRACT OF THE DISSERTATION

Cross Amyloid interfaces of Amyloid Beta

by

Sarah Lorraine Griner

Doctor of Philosophy in Biochemistry & Molecular Biology

University of California, Los Angeles, 2018

Professor David S. Eisenberg, Chair

The pathological aggregation of proteins into amyloid fibrils is the hallmark for a variety of diseases. The fibrils are morphologically similar- long unbranched filaments displaying a characteristic cross-β structure- despite sometimes large sequence differences, and distinct pathological symptoms. While each amyloid disease is commonly linked to a main misfolded protein, progression of some amyloid diseases affects progression of others. In Alzheimer's disease (AD), accumulation of amyloid (Aβ) in the brain is thought to occur at the earliest stages of the disease and drive pathogenesis. However, formation of neurofibrillary tangles containing another amyloid protein, tau, correlates much better with cognitive loss. Patients with AD also carry a significant risk for developing type-II diabetes, in which fibrils of human islet amyloid polypeptide (hIAPP) deposit in the kidneys.

The common amyloid aggregation motif has posed the hypothesis that one amyloid protein could directly nucleate another via cross-amyloid interactions. To elucidate the molecular basis for these interactions, we used a pioneer method, microcrystal electron diffraction, to determine atomic structures of potential cross-seeding regions of Aβ. We found that fibrils of structurally

similar 11-residue segments from hIAPP and Aβ induce amyloid formation of both parent proteins through self- and cross-seeding. Structure-based inhibitors designed for the hIAPP segment were able to reduce cytotoxicity of both proteins. Additionally, we designed inhibitors for second potential cross-seeding region of Aβ. While reducing Aβ aggregation and toxicity as designed, the inhibitor also reduces Aβ-mediated tau aggregation, and moreover reduces aggregation and self-seeding of tau fibrils. Using mutagenesis and structural alignment, we find that tau and Aβ may contain similar interfaces. Fully understanding cross-amyloid interfaces could provide insight into disease progression and potentially also lead to therapeutic targets.

The dissertation of Sarah Lorraine Griner is approved.

Joseph Ambrose Loo

Robert Thompson Clubb

Feng Guo

Pascal Francois Egea

David S. Eisenberg, Committee Chair

University of California, Los Angeles

2019

Dedicated to my parents,
and my husband Chris, who moved here for me despite the general lack of rain

TABLE OF CONTENTS

List of Figures……vii

List of Tables……viii

Acknowledgements……ix

Vita……xi

Publications……xii

Overview ……1

Chapter 1 Structure based inhibitors of Amyloid Beta core suggest a common interface with Tau ……3

Supplemental information……40

References……54

Chapter 2 Common Fibrillar Spines of Amyloid-β and human Islet Amyloid Polypeptide Revealed by Micro Electron Diffraction and Inhibitors Developed Using Structure-Based Design……62

Supplemental information……96

References……107

LIST OF FIGURES

Chapter 1:

Figure 1.1. MicroED structure of segment Aβ 16-26 D23N from microcrystals ……8

Figure 1.2. Development of inhibitors of Aβ fibril formation using structure-based design against Aβ 16-26 D23N ……11

Figure 1.3. Designed inhibitors reduce aggregation of Aβ1-42. ……14

Figure 1.4. Inhibitors bind and block toxicity of aggregated Aβ1-42……17

Figure 1.5. Tau aggregation is seeded by Aβ and reduced by structure-based inhibitors**.** ……19

Figure 1.6. Aβ inhibitors also reduce fibril formation and seeding by tau40. ……22

Figure 1.7. Peptide inhibitors reduce seeding by crude brain-extract from tauopathy donor tissue……25

Figure 1.8. Crystal packing of the Aβ 16-26 D23N atomic structure……42

Figure 1.9. Extended Toxicity data of inhibitors of Aβ fibril formation ……43

Figure 1.10. Peptide inhibitors D1a, D1c, D1e, and D1f are less effective ate reducing fibril formation of Aβ1-42……44

Figure 1.11. Representative Sensorgram of D1d SPR……45

Figure 1.12. Extended ThT data of Tau seeding experiment ……46

Figure 1.13. Extended Tht and Toxicity data against tau mutants and other amyloid proteins ……47

Figure 1.14. The spines of Aβ 16-26 D23N and tau are structurally similar ……49

Chapter 2:

Figure 2.1. Sequence alignment of amyloid-β1-42 (Aβ1-42) and hIAPP……65

Figure 2.2. MicroED structure of segment Aβ 24–34 WT from microcrystals……67

Figure 2.3. Aβ 24-34 WT is cytotoxic to N2a cells, a mouse neuroblastoma cell line. ……70

Figure 2.4. The spines of Aβ 24-34 WT and hIAPP 19-29 S20G are structurally similar. ……73

Figure 2.5. Development of inhibitors using structure-based design against hIAPP 19-29 S20G ….75

Figure 2.6. Cross-amyloid efficacy of inhibitors developed with structure-based design against hIAPP 19-29 S20G ……77

Figure 2.7. Other peptide inhibitors developed against hIAPP 19-29 S20G reduce cytotoxicity ……..80

Figure 2.8. Model of an Aβ 24-34 WT and hIAPP 19-29 S20G hetero-assembly, which may explain how full-length Aβ and hIAPP cross-seed ……83

Figure 2.9. Crystal packing of the Aβ 24–34 WT atomic structure reveals two interfaces ……100

Figure 2.10. Fibrillar forms of Aβ 24-34 WT and hIAPP 19-29 S20G are cytotoxic to N2a cells. ……101

Figure 2.11. Extended ThT assay data. ……102

Figure 2.12. Other inhibitors developed with structure-based design against the hIAPP 19-29 S20G structure also reduce cytotoxicity of hIAPP 19-29 S20G.……103

Figure 2.13. Inhibitors are not cytotoxic and they do not form fibrils ……104

Figure 2.14. Peptide inhibitors p14 and p15 are specific for the design target and they do not reduce fibril formation of two other amyloid proteins, transthyretin (TTR) and tau.……105

Figure 2.15. Quantification of antibody-binding experiments ……106

LIST OF TABLES

Chapter 1:

Table 1.1. Statistics of MicroED data collection and atomic refinement.……9

Table 1.2. Computed binding properties of designed inhibitors to amyloid-beta $_{16}$KLVFFAEN$_{23}$…..50

Chapter 2:

Table 2.1. Statistics of MicroED data collection and atomic refinement ……68

Table 2.2. Computed binding properties of designed inhibitors to hIAPP 19-29 S20G……98

Table 2.3. Aβ 24-34 WT and IAPP 19-29 S20G heterozipper and homozipper model Rosetta interaction energies……99

ACKNOWLEDGEMENTS

First of all, I would like to thank Dr. David Eisenberg for welcoming me into his lab. This project would have been impossible without his support, and confidence in my abilities. David allowed me the freedom and resources to take the quest of identifying toxic structures of Abeta into a reality. Thank you David, for standing by me throughout all of my challenges.

I 'd like to thank my committee for their time and mentorship. Thank you for listening to my ideas helping guide my experiments in a logical way to what I hoped to scientifically accomplish. Thank you, Feng Guo, Pascal Egea, Rob Clubb, Joe Loo, and David Eisenberg.

Much of this work would have been impossible if not for an extraordinary crystallography team. Tamir Gonen and Jose Rodriguez were instrumental to this work. Without their expertise in microED and willingness to collect data, determining the structures that the rest of my work is built upon would not have been possible. I'd like to thank Michael Sawaya, and Duilio Cascio for help with structure determination and modeling, and Michael Collazo for setting up more crystal trays for me than I would care to admit.

I would especially like to thank Pascal Krotee, who was my co-author on the Aβ-IAPP project. Her work on the related hIAPP structure and willingness to collaborate allowed my work a much more interesting conclusion than it could have ever had on its own. She is an extremely thoughtful scientist and pushed me to explore cross-amyloid interactions.

I'd like to thank Paul Seidler, Jeannette Bowler, Kevin Murray, Shruti Sahay, and Peter Yang for their help on the Aβ-tau project. This project was challenging in so many ways, thank you for bringing expertise to experiments that I knew needed to be done, but could not accomplish on my own.

UCLA, in particular, the Eisenberg lab was a wonderful place to spend my graduate career. I met so many talented scientists and all around amazing people. Each has influenced my scientific growth in ways big and small. I'd like to thank Dan Anderson for all of the instrument guidance over the years, as well as keeping the lab safe and functional.

I'd like to thank my collaborators. Stephan Philipp in the Glabe lab enhanced my projects using a panel of conformational antibodies. I would also like to thank the Diamond lab for supplying tau biosensor cells. The Stroud lab, Linse Lab, and Diamond Light source all welcomed me to their crystallization facilities.

I'd like to acknowledge a few people that have helped me develop into the scientist I am today. Arthur Glasfeld introduced me to the basics of crystallography, and took me on my first synchrotron trip. Bob Stroud introduced me to the larger structural biology community continues to be a wonder mentor.

Lastly, I would like to thank my husband and my community of non-scientist friends. Thank you for always supporting me, even when I did a poor job of explaining what I was working on.

VITA

Education

Reed College Portland, OR — May 2005
B.A. in Chemistry
Thesis: Structural Studies on the Metal Binding Site of MntR
Advisor: Prof. Arthur Glasfeld

Research and Work Experience

Graduate researcher, Eisenberg Lab, UCLA	Aug 2012 – Jun 2018
Teaching Assistant, Biochemical Methods II	Jan 2013 - Dec 2013
Staff Research Associate, Stroud Lab, UCSF	Dec 2005 – July 2011
Student researcher, Glasfeld Lab, Reed College	May 2004 – Aug 2005
Teaching and Laboratory Assistant, Organic Chemistry	Aug 2003-Dec 2004
Teaching Assistant, Introductory Chemistry	Aug. 2004-May 2005

PUBLICATIONS

Krotee P*, **Griner SL***, Sawaya MR, Cascio D, Rodriguez JA, Shi D, Philipp S, Murray K, Saelices L, Lee J, Seidler P, Glabe CG, Jiang L, Gonen T, Eisenberg DS. Common fibrillar spines of amyloid-β and human islet amyloid polypeptide revealed by microelectron diffraction and structure based inhibitors. J Biol Chem. 2018 Feb 23;293(8):2888-2902. *Authors contributed equally to this work

Krotee P, Rodriguez JA, Sawaya MR, Cascio D, Reyes FE, Shi D, Hattne J, Nannenga BL, Oskarsson ME, Philipp S, **Griner S**, Jiang L, Glabe CG, Westermark GT, Gonen T, Eisenberg DS. Atomic structures of fibrillar segments of hIAPP suggest tightly mated β-sheets are important for cytotoxicity. Elife. 2017 Jan 3;6. pii: e19273.

Galilee M, Britan-Rosich E, **Griner SL**, Uysal S, Baumgärtel V, Lamb DC, Kossiakoff AA, Kotler M, Stroud RM, Marx A, Alian A. The Preserved HTH-Docking Cleft of HIV-1 Integrase is Functionally Critical. Structure. 2016 Nov 1;24(11):1936-1946

Tochowicz A, Dalziel S, Eidam O, O'Connell JD 3rd, **Griner S**, Finer-Moore JS, Stroud RM. Development and Binding Mode Assessment of N-[4-[2-Propyn-1-yl[(6S)-4,6,7,8-tetrahydro-2-(hydroxymethyl)-4-oxo-3H-cyclopenta[g]quinazolin-6-yl]amino]benzoyl]-L-γ-glutamyl-D-glutamic Acid (BGC 945), a Novel Thymidylate SynthaseInhibitor That Targets Tumor Cells. J Med Chem. 2013 Jun 21. ;56(13):5446-55.

McGuire AM, Cuthbert BJ, Ma Z, Grauer-Gray KD, Brunjes Brophy M, Spear KA, Soonsanga S, Kliegman JI, **Griner SL**, Helmann JD, Glasfeld A. Roles of the A and C sites in the manganese-specific activation of MntR. Biochemistry. 2013 Jan 29;52(4):701-13.

Wu S, Avila-Sakar A, Kim J, Booth DS, Greenberg CH, Rossi A, Liao M, Li X, Alian A, **Griner SL**, Juge N, Yu Y, Mergel CM, Chaparro-Riggers J, Strop P, Tampé R, Edwards RH, Stroud RM, Craik CS, Cheng Y. Fabs enable single particle cryoEM studies of small proteins. Structure. 2012 Apr 4;20(4):582-92

Alian A, **Griner SL**, Chiang V, Tsiang M, Jones G, Birkus G, Geleziunas R, Leavitt AD, Stroud RM. Catalytically-active complex of HIV-1 integrase with viral DNA substrate binds anti-integrase drugs. Proc Natl Acad Sci U S A. 2009 May 19;106(20):8192-7.

Alian A, DeGiovanni A, **Griner SL**, Finer-Moore JS, Stroud RM. Crystal structure of an RluF-RNA complex: a base-pair rearrangement is the key to selectivity of RluF for U2604 of the ribosome. J Mol Biol. 2009 May 15;388(4):785-800.

Alian A, Lee TT, **Griner SL**, Stroud RM, Finer-Moore J. Structure of a TrmA-RNA complex: A consensus RNA fold contributes to substrate selectivity and catalysis in m5U methyltransferases. Proc Natl Acad Sci U S A. 2008 May 13;105(19):6876-81.

Kliegman JI, **Griner SL**, Helmann JD, Brennan RG, Glasfeld A. Structural basis for the metal-selective activation of the manganese transport regulator of Bacillus subtilis. Biochemistry. 2006 Mar 21;45(11):3493-505.

Overview

The work contained in this dissertation started with a very daunting idea to identify toxic structures of Aβ. This task had two main challenges to overcome. First, Aβ aggregates are heterogeneous, ranging from transient oligomers to deposited fibers. Secondly, the mechanism of toxicity is unknown. This lead me to focus on a small part of what could constitute a toxic structure: the cross-amyloid interface. Herein, I describe my findings on cross-amyloid interfaces of Aβ, identified using MicroED and structure-based inhibitors.

Chapter one is a manuscript which has been submitted to *eLife* for publication. This paper describes peptide based inhibitors designed against a structure of the amyloid beta core with both fibril and oligomeric elements. These inhibitors are effective against Aβ and tau mediated seeding of tau, suggesting that the two could share a common interface which is involved in cross-seeding.

This project started with very small crystals of Aβ 16-26 D23N, which did not yield diffraction data until Jose Rodriguez proposed trying a new method. He, Johan Hattne, and Tamir Gonen collected the MicroED diffraction data. I solved the Aβ 16-26 D23N with Michael Sawaya and Duilio Cascio. From this structure, I manually designed inhibitors, and enlisted the help of Kevin Murray to computationally design inhibitors. I assayed the inhibitors effects on aggregation by ThT, and EM, and made samples for Jeannette Bowler to test on N2a cells, and analyzed those results. Shruti Satay tested binding by SPR.

This project became a whole lot more involved when while testing the inhibitors for Aβ specificity, it became clear that they were also effective against tau aggregation. Paul Seidler provided me with tau protein to perform all of the aggregation assays and cross-

seeding assays. Paul tested my Aβ fibrils for seeding in tau biosensor cells. From there, we designed a number of experiments, which Paul carried out, to test the inhibitors on homo- and hetero-typic seeding, and against brain derived extract. Peter Yang created the mutant constructs of tau, and performed the associated biosensor seeding experiment, from which we used to determine tau interface sensitivities to the inhibitors, and I used as a basis for structural alignment.

Chapter two is the manuscript version of an article published in JBC which describes a structural model of Aβ and hIAPP cross-seeding, elucidated from microED structures and structure based inhibitors. We found that Aβ and hIAPP share a structurally similar interface, which appears to be sufficient to seed amyloid formation in both. Inhibitors designed against the hIAPP interface reduce cytotoxicity of both parent proteins. This work was co-first authored by myself and Pascal Krotee. I was responsible for the Aβ aspects of this project. I crystallized, solved and analyzed Aβ 24-34 WT with the help of Michael Sawaya and Duilio Cascio. Jose Rodriguez, Dan Shi, and Tamir Gonen collected the MicroED diffraction data. I performed the Aβ and alpha synuclein aggregation assays, prepared Aβ samples for toxicity and dot blot assays. I performed and analyzed all of the cross-seeding experiments. Pascal designed and screened inhibitors with the help of Lin Jiang, performed structural alignments, cultured cells, executed and analyzed toxicity experiments, performed hIAPP aggregation assays. Kevin Murray and Michael Sawaya assisted us with structural overlays and hetero-zipper modeling. Pascal and I wrote the manuscript together. This work was later highlighted in a special Amyloid issue of JBC, and chosen to be its cover image.

Chapter One

Structure based inhibitors of Amyloid Beta core suggest a common interface with Tau

ABSTRACT

Alzheimer's disease (AD) pathology is characterized by plaques of amyloid beta (Aβ) and neurofibrillary tangles of tau. Aβ aggregation is thought to occur at early stages of the disease, and ultimately gives way to the formation of tau tangles which track with cognitive decline. Here, we report the crystal structure of an Aβ core segment determined by MicroED and in it, note characteristics of both fibrillar and oligomeric structure. Using this structure, we designed peptide-based inhibitors that reduce Aβ aggregation and toxicity of already-aggregated species. Unexpectedly, we also found that these inhibitors reduce the efficiency of Aβ-mediated tau aggregation, and moreover reduce aggregation and self-seeding of tau fibrils. The ability of these inhibitors to interfere with both Aβ and tau seeds suggests these fibrils share a common epitope, and supports the hypothesis that cross-seeding is one mechanism by which amyloid is linked to tau aggregation and could promote cognitive decline.

INTRODUCTION

Although Alzheimer's disease (AD) is the most prevalent form of dementia, there are limited treatments to alleviate symptoms and none that halt its progression. Histological features of AD are extracellular senile plaques of amyloid beta (Aβ) and intracellular neurofibrillary tangles of tau (1, 2). While Aβ aggregation is thought to occur at the early stages of AD, tau aggregation correlates better to disease progression, with characteristic spreading along linked brain areas, and severity of symptoms correlating to the number of observed inclusions (3–8) . Structural information about the aggregated forms of Aβ and

tau is accumulating, but to date this knowledge has not led to successful chemical interventions (9)

A link between the appearance of Aβ and tau pathologies has been noted in transgenic mouse models generated by crossing or co-expressing mutant Aβ and mutant tau, but the mechanism is not yet understood at the molecular level (10). By injecting Aβ seeds derived from synthetic peptide, transgenic mouse or AD patient tissue, tau pathology can be found both at the site of injection, and also in functionally connected brain areas (11–13). Tau aggregation has also been reported to follow Aβ seeding in 3D neuronal stem cell cultures that express early onset hereditary mutations to drive overproduction and aggregation of Aβ (14). In spite of these observations, the molecular linkage of Aβ to tau remains unresolved. Proposed hypotheses include Aβ causing downstream cellular changes that trigger tau phosphorylation and eventual aggregation, and/or a direct interaction and seeding of tau by aggregated Aβ (15, 16).

Several lines of evidence support the direct interaction model, although questions still remain; for example, how such an interaction could occur since Aβ plaques deposit extracellularly, while tau neurofibrillary tangles are intracellular. One possible model for intracellular aggregation could be that Aβ is cleaved from APP inside endosomes, and then exported (17). Another model proposes that smaller diffusible Aβ oligomers are the toxic species (18–20); indeed oligomers of Aβ isolated from AD serum are sufficient to induce tau aggregation (21). Aβ has also been found co-localize intra-neuronally with tau as well as at synaptic terminals, with increased interactions correlating with disease progression (5). Furthermore, soluble and insoluble complexes of Aβ bound to tau have been detected in AD tissue extracts (5, 22). *In vitro*, soluble complexes of Aβ and tau have been found to

promote aggregation of tau(22), while another study found that Aβ fibrils can seed tau (23). Taking the evidence together, we hypothesize that cross-seeding of tau by Aβ promotes tangle formation in AD, which could be prevented not only by inhibiting Aβ aggregation, but also by disrupting the binding site of Aβ with tau.

A number of interaction sites have been proposed on both proteins. In Aβ, both the amyloid core KLVFFA, along with region spanning the carboxy terminal residues were found to bind tau (22). Conversely peptides from regions of tau in exons 7 and 9, well as aggregation prone sequences VQIINK and VQIVYK located at the beginning of repeat 2 (R2) and repeat 3 (R3) of the microtubule domain (K18), respectively, were found to bind Aβ (22). A computational seeding model predicts that the amyloid core of Aβ can form intermolecular β-sheet interactions with VQIINK or VQIVYK (24).

On this basis, we hypothesized that an inhibitor capable of targeting the amyloid core, which itself is an important sequence for Aβ aggregation (25–27), might block both Aβ aggregation and tau seeding by Aβ. However, this segment has been observed in multiple conformations in steric zipper structures (28) and fiber models (29–33), impeding structure-based inhibitor design. In an effort to characterize a toxic conformation of this sequence, we focused our efforts on determining the structure of the segment 16-26, containing the Iowa early onset hereditary mutation, D23N (34). Based on this structure, we designed several inhibitors and found that they indeed blocked aggregation of Aβ, prevented cross-seeding of tau by Aβ, and surprisingly, also blocked tau homotypic seeding. We suggest that the efficacy of these structure-based inhibitors against both proteins, but not other amyloid fibrils, implies there is a similar binding interface displayed on both Aβ and tau aggregates, supporting the cross-amyloid cascade hypothesis in AD.

RESULTS

Atomic structure of $A\beta_{16\text{-}26}$ D23N determined using MicroED

With crystals only a few hundred nanometers thick, we used micro-electron diffraction (MicroED) to determine the structure of Aβ residues 16-26 containing the hereditary mutation D23N, (Figure 1A), KLVFFAENVGS. The structure revealed pairs of anti-parallel β-sheets each composed of ~4000 strands, stacked into a fibril that spans the entire length of the crystal. Neighboring sheets are oriented face to back (Figure 1B, Table 1) defining a Class 7 steric zipper motif. In addition, the three C-terminal residues adopt an extended, non-β conformation which stabilizes the packing between steric zippers (Figure 8—Supplemental). The sheet-sheet interface is strengthened by interdigitating side chains, Lys 16, Val18, Phe20, Glu22 from the face of one strand, and Leu17, Phe19, and the N-terminus from the back of the other. The zipper has an extensive interface with a high shape complementarity of 0.76 and a total buried solvent accessible surface area of 258 Å2.

This structure is partly identical to that of a shorter peptide segment, Aβ16-21, KLVFFA (crystal form-I) (28), which we used successfully as a search model for molecular replacement. Both the longer and shorter segments have class 7 symmetry. However, the two segments differ in registry. The shorter segment maintains an in-register hydrogen bonding pattern while the longer segment is out-of-register. That is, the strands of Aβ16-26 are tilted away from perpendicular to the fibril axis—a departure from canonical cross-β architecture.

The antiparallel architecture and lack of registration of Aβ16-26 suggest this "fibrillar" assembly has some characteristics of an amyloid oligomer. Structural studies of amyloid oligomers most frequently reveal anti-parallel β sheet architecture (35–37),

whereas most fibril structures have revealed parallel (29, 30, 33, 38), with the exception of some short segments of Aβ (39) and the early onset hereditary mutation D23N which leads to anti-parallel fiber deposition in plaques (31, 40). Thus, the out-of-register stacking of anti-parallel β strands has been proposed to be the defining trait of toxic oligomers (36, 41). The segment Aβ16-22 has been proposed to be able to form such oligomers in silica (42). Thus, the structures of Aβ16-21 and Aβ16-26 may offer clues to designing inhibitors that impede both fibrillar and oligomeric assemblies.

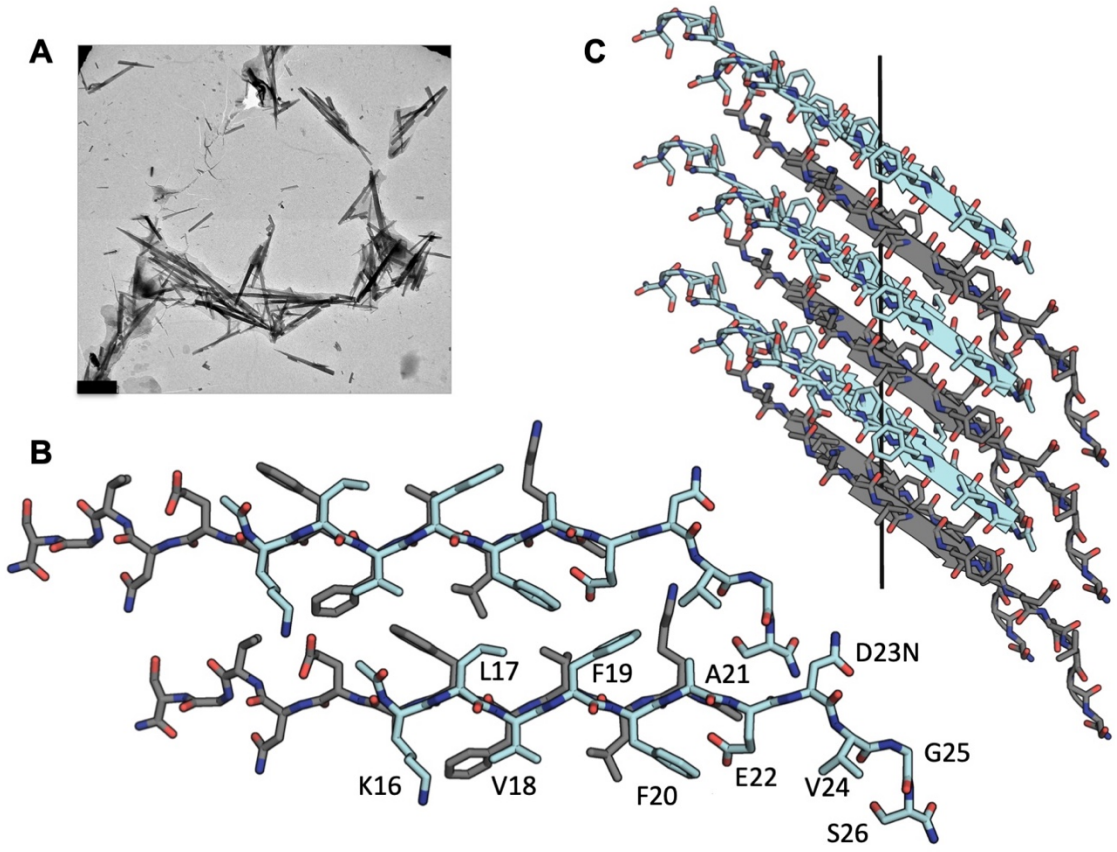


Figure 1. MicroED structure of segment Aβ 16-26 D23N from microcrystals. **A**. Electron micrograph of 3D crystals used for data collection, scale bar is 1μm. **B**. The crystal structure reveals tightly mated pairs of anti-parallel β-sheets with opposing sheets in grey and cyan. The side-chains interdigitate to form a dry interface. Two neighboring sheets are viewed perpendicular to the β-sheets. **C**. View of 6 layers perpendicular to the fibril axis (black line). The β-sheets stack out of register along the fibril axis.

Table 1. Statistics of MicroED data collection and atomic refinement.

	KLVFFAENVGS
Excitation Voltage (kV)	200
Electron Source	field emission gun
Wavelength (Å)	0.0251
Total dose per crystal (e^-/ Å^2)	2.7
Frame rate (frame/s)	0.3-0.5
Rotation rate (°/s)	0.3
#crystals used	13
Total angular rotation collected (°)	941
Merging Statistics	
Space group	$P2_1$
Cell dimensions	
a, *b*, *c* (Å)	11.67, 51.91, 12.76
α, β, γ (°)	90, 114.18, 90
Resolution (Å)	11.64-1.4 (1.44-1.40)*
R_{merge}	24.0% (65.2%)
No. Reflections	47,598 (1966)
Unique Reflections	2355 (163)
Completeness (%)	86.2% (78.0%)
Multiplicity	21 (12)
I/σ	9.06 (2.88)
$CC_{1/2}$	99.5% (69.7%)
Refinement Statistics	
No. reflections	2354
Reflections in test set	236
R_{work}	23.7%
R_{free}	28.3%
R.m.s. deviations	
Bond lengths (Å)	0.014
Bond angles (°)	1.5
Avg. B factor (Å^2)	9.46
Wilson B factor (Å^2)	7.2
Ramachandran (%)	
Favored	100%
Allowed	0%
Outliers	0

*Highest resolution shell shown in parenthesis.

As the zipper motif observed in the atomic structure of $A\beta_{16-26}$ D23N may be relevant to a variety of amyloid beta assemblies, we sought to use it to develop structure-based peptide inhibitors of $A\beta_{1-42}$. Our laboratory has developed a Rosetta based design strategy using steric zipper structures to design capping peptide inhibitors for a number of amyloid proteins implicated in disease (43–47). We chose to truncate our structure to residues 16-22 for the search model, omitting the residues not in the β strand. We threaded amino acids onto a capping β strand and minimized energies of sidechains. From our first round of design we chose 6 distinct inhibitor candidates; those that were identified as good candidates but containing strong amino acid similarities to other top inhibitors were discarded. Our initial pool of inhibitors contained four L-form peptides, 2 each of 6 and 8 amino acids length, termed L1-L4, and two D-peptides 6 amino acids long, termed D1 and D2.

We assessed the efficacy of the inhibitors at a 10 molar excess by testing if they prevented $A\beta_{1-42}$ toxicity on Neuro-2a (N2a) cells, a mouse neuroblastoma cell line, (48). We measured cytotoxicity using 3-(4,5-dimethylthiazol-2-yl)-2,5-diphenyltetrazolium bromide (MTT) dye reduction (49, 50). Our toxicity assay revealed one inhibitor, D1 with the sequence (D)-LYIWVQ, that was able to eliminate the toxic effect of $A\beta_{1-42}$ (Figure 2A, Table 2); none of the inhibitors were toxic to N2a cells alone (Figure 9A—Supplement). In our molecular model of the inhibitor, smaller hydrophobic residues of D1 mimic interactions with the fibril interface on one side of the peptide, which promotes recognition, (Figure 2B), while the other side of the peptide positions large aromatic residues between Aβ residues, blocking possible further interactions (Figure 2C).

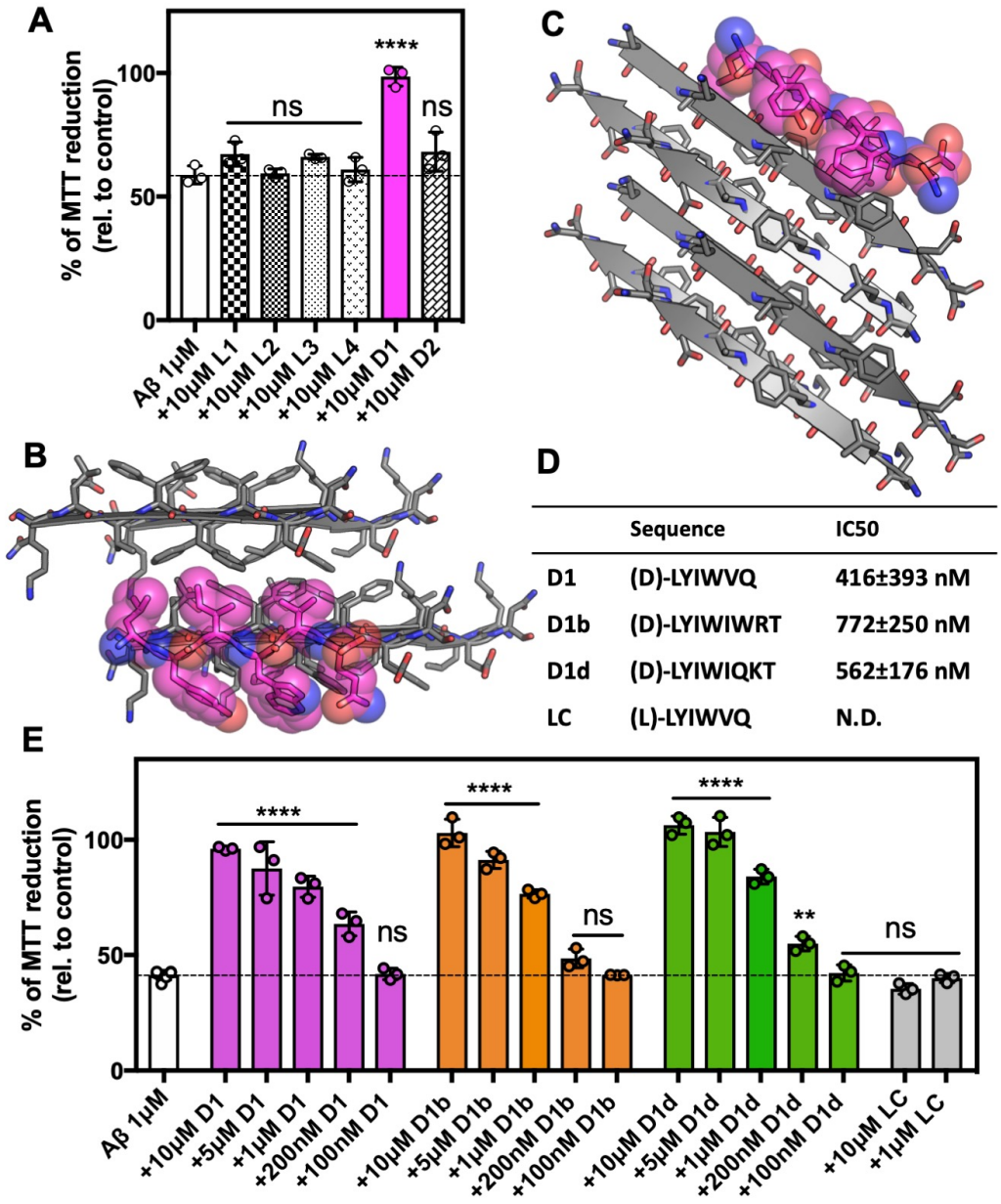


Figure 2. Development of inhibitors of Aβ fibril formation using structure-based design against Aβ 16-26 D23N **A**. Identification of Aβ1-42 inhibitor. 10 μM Aβ1-42 was incubated alone or with 100 μM of each candidate peptide inhibitor for 12 hours at 37 °C and then diluted 1:10 with pre-plated N2a cells. Cytotoxicity was quantified using MTT dye reduction Bars represent mean with individual technical replicates (n = 3; ns = not significant; ****, $p < 0.0001$ using an ordinary one-way ANOVA relative to leftmost column) **B, C.** Segment KLVFFAEN, derived from the Aβ 16-26 D23N crystal structure, was used as the design target. Model of peptide inhibitor D1(magenta) bound to the design target, KLVFFAEN (gray). Smaller hydrophobic residues of D1 mimic interactions with the fibril interface on one side of the peptide (**B)**, whereas the other side of the peptide positions

large aromatic residues between Aβ residues, breaking possible further interactions (**C**). **D.** Overview of peptide inhibitors in D and L amino acid conformations, as indicated, used in this study and their sequences. Peptide LC is the L-form cognate peptide of D-form peptide D1 and is the negative control for peptide inhibitor D1 and its derivatives D1b and D1d. IC_{50} values were determined using 4 parameter nonlinear fit. N.D., not determined. **E.** Peptide inhibitors D1, D1b, and D1d reduce the cytotoxicity of Aβ1-42 in a dose dependent manner, whereas control peptide LC does not. 10 μM Aβ1-42 was incubated alone or with various concentrations of each peptide inhibitor for 12 hours at 37 °C and then diluted 1:10 with pre-plated N2a cells. Cytotoxicity was quantified using MTT dye reduction. Bars represent mean with individual technical replicates (n = 3-6; ns = not significant; **, p < 0.002; ****, p < 0.0001 using an ordinary one-way ANOVA relative to leftmost column)

We focused on these key features of the inhibitor sequence for our second round of design and aimed to improve efficacy. We lengthened our peptides to extend over more of our available structure towards the carboxy-terminus and made conservative residue changes to the face containing smaller hydrophobic residues. We selected and tested 6 new designs. Of the six,

four were eight amino acids long such that the inhibitor would extend over more of our crystal structure, which we called D1a-D1d. The additional two, termed D1e and D1f, were six amino acids long featuring slight sequence perturbations from D1 (Table S1). We identified 2 of the 8 amino acid long inhibitors, D1b and D1d, that were also effective at reducing AB_{1-42} toxicity at both a tenfold excess and at an equimolar ratio (Figure 9B,C—Supplement). We then tested these two inhibitors, as well as D1, across a range of concentrations with final concentrations ranging from 100 nM to 10 μM (Figure 2D, E). We found that all inhibitors elicited a dose dependent response, with all having an IC_{50} of less than 1uM. The 6 residue long inhibitors, D1e and D1g, also had a similar effect on toxicity reduction as D1, however they did not perform as well as D1 in additional characterization

and were not explored further (Figure 10A—Supplement). The cognate negative peptide control, LC, the L-form peptide of inhibitor D1, did not reduce toxicity (Figure 2E).

Reduction of toxicity by designed inhibitors is explained by a reduction of $A\beta_{1-42}$ aggregation

We next sought to understand the mechanism by which our peptide inhibitors reduce the toxic effect of $A\beta_{1-42}$. We therefore assayed fibril formation to discern if this reduction of toxicity could be explained by reduced aggregation. We incubated $A\beta_{1-42}$ with our inhibitors at 10:1, 1:1, and 1:10 molar ratios and monitored fibril formation by thioflavin-T (ThT) fluorescence at 37 °C under quiescent conditions. We observe that all of our inhibitors reduce fibril formation in a dose dependent manner, while the negative control peptide, LC, does not (Figure 3A). The longer inhibitors, D1b and D1d, appear effective at an equimolar ratio. However, when assayed at higher concentrations, the inhibitors appear to self-assemble, but remain effective at reducing $A\beta_{1-42}$ toxicity (Figure 10B—Supplement, Figure 2E). After 72 hours, samples were taken for negative-stain TEM analysis, which confirmed the reduced abundance of Aβ1-42 fibrils. D1b and D1d were more effective at reducing fibril formation than D1, although all three inhibitors showed near equal efficiency in reducing toxicity. Fibrils were observed in the equimolar ratio sample of $A\beta_{1-42}$ with D1, whereas the comparable samples with D1b and D1d did not contain fibrils. Inhibitors that were not efficient at preventing toxicity, such as D1a and D1c, were also less effective at blocking fiber formation (Figure 9C ,Figure 10A—Supplement).

Since oligomers, and not fibrils, are considered to be the more toxic species of Aβ (18–21), we then investigated if our inhibitors affect the formation of oligomers or other

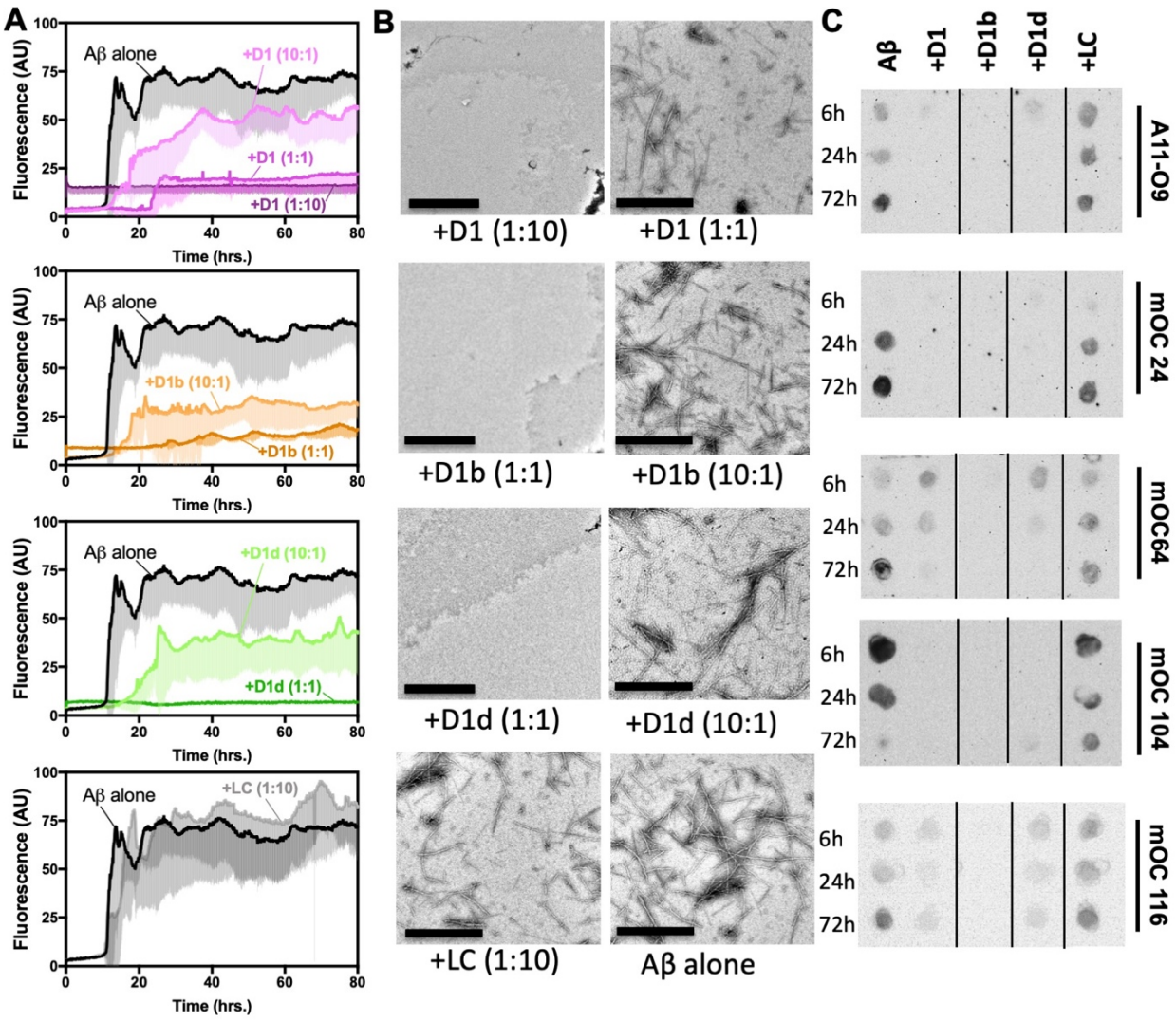


Figure 3. Designed inhibitors reduce aggregation of Aβ1-42 A. Peptide inhibitors D1, D1b, and D1d reduce fibril formation of Aβ1-42, while negative control peptide LC does not. 10 μM of Aβ1-42 was incubated alone or at a 1:10, 1:1, or 10:1 molar ratio to each inhibitor under quiescent conditions at 37 °C. Fibril formation was monitored using ThT fluorescence. Curves show the average of three technical replicates with one standard deviation below. **B.** Negative-stain TEM analysis confirms the results of the ThT assays in Figure 3A. Samples were prepared as above and incubated for 72 hours before TEM analysis. Images of Aβ1-42 to D1 (1:10), D1b (1:1) and D1d (1:1) were captured at 3,200x; scale bars are 2μm. All other images were captured at 24,000x; scale bars are 500 nm. **C.** Peptide inhibitors reduce the formation of Aβ1-42 assemblies recognized by conformational monoclonal antibodies, while negative control peptides do not. 10 μM Aβ1-42 was incubated alone (left-most column) or with 10-fold molar excess of each peptide-based inhibitor. Aliquots of the reaction were tested for antibody-binding at 6 h, 24 h, and 72 h. Membranes were spliced as indicated for clarity.

cytotoxic $A\beta_{1-42}$ species. We used conformational antibodies to probe samples of $A\beta_{1-42}$ incubated with a 10-molar excess of inhibitor overnight at 37°C. Binding by oligomer specific conformational antibody A11-O9, a monoclonal variant of A11, was reduced by all of our inhibitors (Figure 3C, Figure 10C—Supplement). Additionally, the inhibitors reduced the abundance of Aβ conformations recognized by antibodies mOC24, mOC64, mOC104, and mOC116. These antibodies bind fibrillar plaques from patient derived AD tissue and/or 3xTg-AD mouse tissue (51). Overall, these results indicate that our inhibitors may reduce disease relevant, and oligomeric conformations.

Inhibitors bind and reduce toxicity of Aβ aggregates

As AD is only diagnosable long after Aβ aggregation has initiated, we wondered if these inhibitors would not only prevent amyloid aggregates from forming, but also if they can reduce the toxic effect of already formed aggregates. First, we incubated 10 μM Aβ at 37°C for 12hours to form oligomers, and then added inhibitors at various concentrations just prior to addition to N2a cells and assayed toxicity by MTT dye reduction. We found that adding the inhibitor to monomeric $A\beta_{1-42}$ prior to incubation had a marked difference from adding inhibitor to pre-formed $A\beta_{1-42}$ oligomers. When co-incubated with monomeric Aβ, the shorter D1 inhibitor was as effective as D1b and D1d at reducing toxicity; however, when added to pre-formed Aβ assemblies, only the longer inhibitors D1b and D1d were effective at reducing toxicity. (Figure 4A). Both of the longer inhibitors could fully ameliorate toxicity of aggregates at 10 μM, but D1d is more potent, with effective reduction of toxicity to 1 μM. D1b differs from D1d only at amino acid positions 6 and 7. We suspect the difference in efficacy is conferred from residue 6, because both inhibitors contain positively charged residues at position 7, but at position 6 D1b contains a Gln while D1d

has a much bulkier Trp. Our results indicate that while peptide inhibitors can both prevent aggregation initiation and block toxicity of aggregated assemblies, the latter appears to be more sensitive to slight perturbations in inhibitor composition.

We next performed TEM to determine if our inhibitors could disaggregate fibers, or if the fibers are being capped, as our inhibitor design would predict. We aggregated 10 μM $A\beta_{1\text{-}42}$ for 72 hours at 37°C under shaking conditions, then added inhibitors at 100 μM and incubated overnight. As the fibers are still present, we presume that our inhibitors are indeed capping or coating the fibers at toxicity inducing interfaces, thus preventing further seeding or toxic effects (Figure 4B). We performed SPR to verify that our inhibitors bind to fibers We find that the most potent inhibitor of aggregated assemblies, D1d, binds to $A\beta_{1\text{-}42}$ fibrils with an apparent K_d of 46 μM (Figure 4C, Figure 11—Supplement). We used a one-inhibitor-to-one-protein substrate model to fit the data; however the true K_d may be lower due to the complication of D1d self-interaction and polymorphic Aβ fibrils. Thus, we have shown that inhibitors D1b and D1d not only prevent aggregation of monomeric Aβ, but also bind aggregated states.

Inhibitors reduce seeding of tau by aggregated $A\beta_{1\text{-}42}$

Having demonstrated that our inhibitors block a toxic interface on Aβ, we next questioned if this interface could also be involved in cross seeding tau. First, we sought to validate the direct seeding mechanism that has been reported by others (22, 24, 52). We tested seeding of full length tau (tau40) in a ThT assay at 37 °C under shaking conditions and found that fibrils of $A\beta_{1\text{-}42}$ seeded aggregation as efficiently as fibrils of the microtubule binding domain of tau (K18) (Figure 5A, Figure 12A—Supplement). Conversely, K18 was unable to seed Aβ (Figure 12B—Supplement).

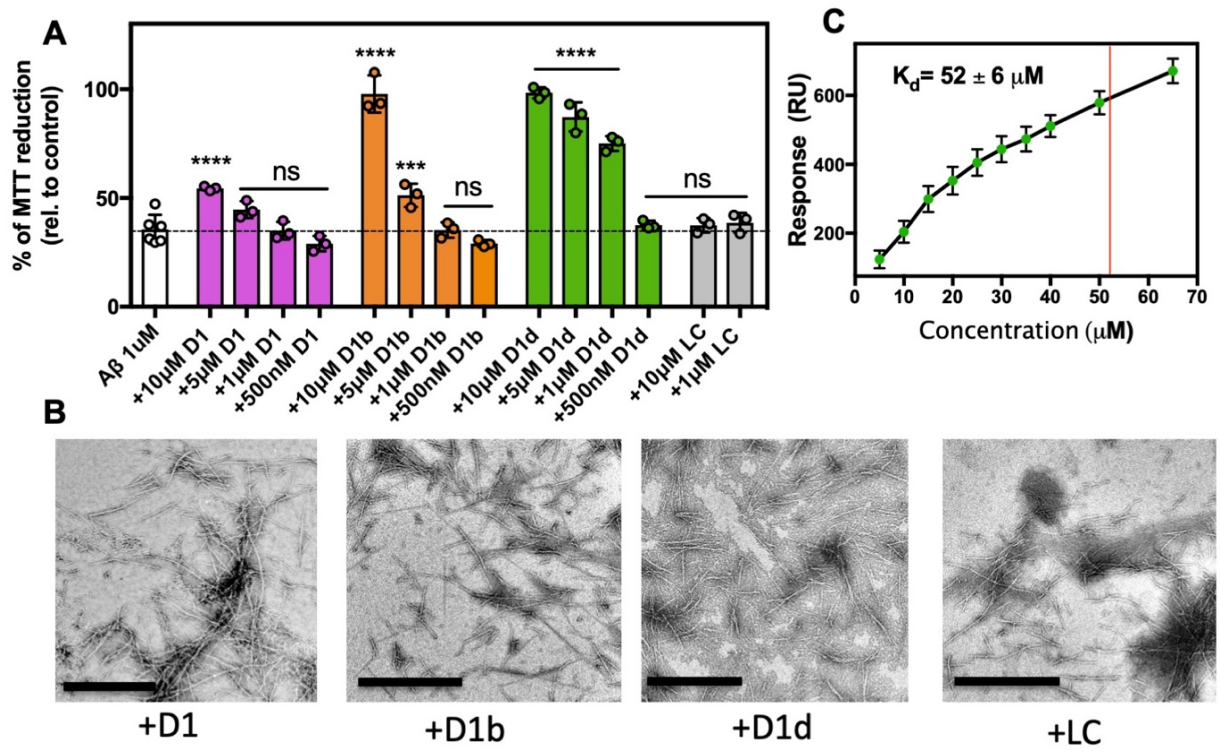


Figure 4. Inhibitors bind and block toxicity of aggregated Aβ1-42. **A.** The toxicity of already formed Aβ1-42 aggregates is lessened by peptide inhibitors. 10 μM Aβ1-42 was incubated alone for 12 hours at 37 °C. Indicated molar ratio of inhibitor was added to the incubated Aβ1-42 and then diluted 1:10 with pre-plated N2a cells. Cytotoxicity was quantified using MTT dye reduction. Bars represent mean with individual technical replicates (n = 3-6; ns = not significant; ***, $p < 0.0005$; ****, $p < 0.0001$ using an ordinary one-way ANOVA relative to leftmost column). **B, C.** Inhibitors bind to Aβ1-42 fibrils. **B.** Peptide inhibitors do not disaggregate Aβ. 10 μM Aβ1-42 was incubated alone for 72 hours at 37 °. Peptide inhibitors were added at 10-fold molar excess and incubated at RT for 24 hours before TEM analysis. Images were captured at 24,000; scale bars are 500 nm. **C.** Binding isotherm of inhibitor D1d to fibrillar Aβ1-42. The maximal response (RU_{max}) was derived by fitting sensorgrams obtained over a range of D1d concentrations to the binding model with a K_d of 52 ± 6 μM. . These RU_{max} values are plotted (mean ± SD, n = 3) as a function of concentration and fitted to a one to one binding model.

Next, we tested seeding in a well-established HEK293 biosensor cell line, tau-K18 (P301S) EYFP, which stably expresses the microtubule binding domain of tau P301S mutant. This cell line, referred to hereafter as tau-K18 biosensor cells, has been used to demonstrate prion like seeding from transfected tau fibrils to cells and has been used as a

model system to test tau inhibitors (44, 53). We transfected biosensor cells with tau40 or Aβ fibrils to a final concentration of 250 nM. We found that Aβ was able to produce intracellular aggregates significantly greater than the vehicle alone, but only at around 2.5% efficiency of tau40. It is not altogether surprising that Aβ has such a low efficiency of cross-seeding; this mirrors a previous result in a similar system (23). It is possible that tau fibrils contain multiple polymorphs and interfaces capable of homotypic seeding, whereas Aβ may have a more limited number of tau seeding-competent conformations. Additionally, in vitro Aβ aggregation may create disproportionate ratios of assemblies compared to those present in AD. Regardless, it remains that some Aβ species is tau-seeding competent.

The finding that Aβ is indeed able to seed aggregation in tau-K18 expressing cell lines suggests that the cross-interacting region of tau is located on this microtubule binding domain. (Figure 12C—Supplement), indicating the biosensor cell assay can faithfully differentiate between amyloid proteins that form morphologically similar fibers, but that differ in their underlying structures and sequences.

If our inhibitors block the interface responsible for seeding, we would expect Aβ treated with inhibitors to no longer to be seeds for tau. To test this hypothesis, we treated 250 nM Aβ fibers with indicated concentrations of inhibitor for 1 hour and transfected these into the biosensor cell line. All of our inhibitors were able to reduce seeding at 20 μM final concentration, while D1b showed a reduction in seeding at a concentration as low as 1 μM (Figure 5DE, Figure 12D—Supplement). While both D1b and D1d reduced Aβ aggregate toxicity on N2a cells, D1d was the more effective inhibitor of Aβ toxicity, whereas D1b is the more effective inhibitor at reducing tau seeding.

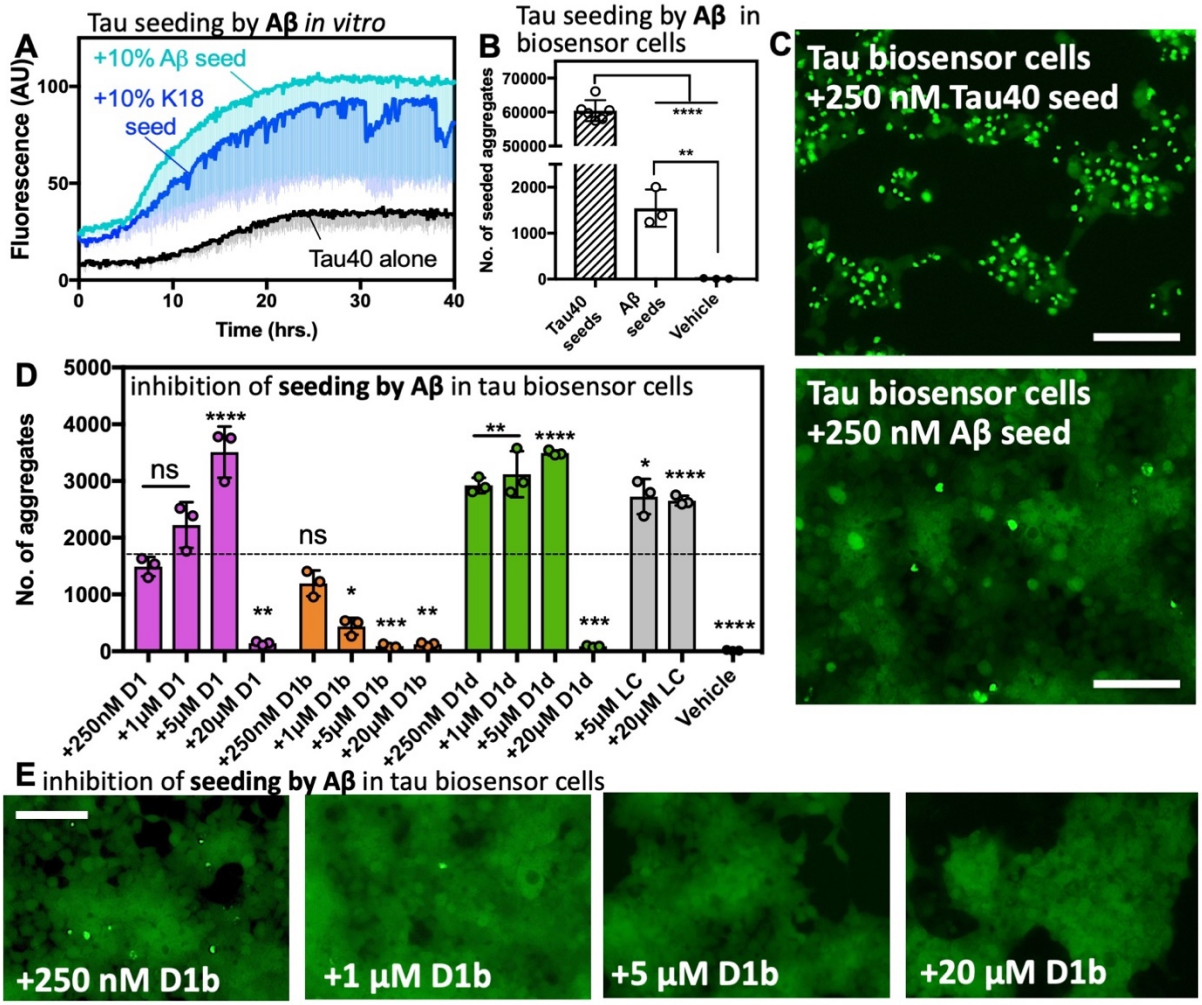


Figure 5. Tau aggregation is seeded by Aβ and reduced by structure-based inhibitors. **A.** 20 μM tau40 was seeded with 10% monomer equivalent of pre-formed fibrils of Aβ1-42 or tau-K18m under shaking conditions at 700 RPM at 37 °C in buffer containing 0.5mg/ml heparin. Fibril formation was monitored using ThT fluorescence. Error bars show the standard deviation of the average of three technical replicates. **B.** The number of intracellular aggregates present in tau-K18CY biosensor cells normalized to cell confluence seeded by the addition of 250 nM tau40 or 250 nM Aβ1-42 fibrils. Error bars show the standard deviation of the mean of technical replicates (n = 3; ****, $p < 0.0001$ using an ordinary one-way ANOVA relative to leftmost column, and **, $p < 0.005$ in unpaired t test of Aβ vs. vehicle) **C.** Representative images of seeded cells from B at 10x magnification, scale bar 100 μm. **D and E.** Concentration dependent inhibition of Aβ1-42 induced seeding of tau aggregation in tau-K18CY biosensor cells. **D.** Average by Aβ as a function of indicated inhibitor concentration. Error bars show the standard deviation of the mean of technical replicates (n = 3; ns = not significant; *, $p < 0.02$; **, $p < 0.005$; ***, $p < 0.001$; ****, $p < 0.0001$ using an ordinary one-way ANOVA relative to leftmost column), and the dotted line shows the mean number of aggregates from untreated Aβ1-42 fibrils. **E.** Representative images of tau-K18CY biosensor cells showing the concentration dependent effect of D1b on seeding. Cells are shown at 10X magnification, scale bar 100 μm.

Inhibitors reduce tau aggregation and seeding

Our data support previous studies that suggest the tau binding surface on Aβ is localized to the segment whose structure we determined and targeted for design of inhibitors against Aβ aggregation and Aβ-mediated seeding of tau (22, 24). We hypothesized that the tau fibril could contain a similar self-complementary surface and would also be susceptible to treatment with our inhibitors. We first asked if the Aβ inhibitors, D1, D1b, and D1d could prevent monomeric tau from aggregating. We performed a ThT assay on 10 μM tau40, at 37 °C with shaking and 0.5 mg/mL heparin and found that all inhibitors function in a dose dependent manner similar to our results with Aβ monomer, while the control inhibitor LC does not reduce tau aggregation (Figure 6A, Figure 13A—Supplement). The peptide inhibitors are not able to block aggregation of the amyloid forming proteins hIAPP or alpha synuclein, indicating that these inhibitors are specific for Abeta and tau, and are not general amyloid inhibitors (Figure 13B—Supplement).

Because we had observed differences in inhibitor efficacy on monomer versus aggregated species of Aβ, we next tested if the inhibitor was effective against the seeding ability of tau40 fibrils. We formed tau40 fibrils, treated them with indicated inhibitor concentration and transfected into tau-K18 biosensor cells to measure seeding inhibition. We found that similar to our Aβ-mediated tau biosensor seeding experiment, D1b was the best inhibitor, with an IC50 of 4.5 μM. D1 was slightly effective, while D1d showed seeding reduction only when increased to 75 μM (Figure 6B, C). It could be that D1b plays a dual role to inhibit both Aβ and tau, and this combined effect could explain the drastically reduced seeding from Aβ fibrils in our prior experiment (Figure 5D).

Next, we sought to determine potential binding sites on tau for D1b. We postulated that regions know to be drivers of tau aggregation could share structural features with the Aβ core, and thus be inhibited by D1b. We designed mutants of tau40 that disrupt key interactions in steric zipper interfaces determined from crystal structures of VQIINK(44) and VQIVYK (54), and cryoEM models of AD tau fibrils (55). In total we tested 6 different constructs, each designed to block all but one aggregation interface of tau. The first 3 mutants were engineered to block the VQIVYK aggregation interfaces in addition to all but 1 of the 3 different known VQIINK interfaces. Mutant 1 (Q276W, L282R, I308P) leaves only interface A of VQIINK available for aggregation, mutant 2 (Q276W, I277M, I308P) leaves only interface B for aggregation, and mutant 3 (I277M, L282R, I308P) leaves only interface C accessible for aggregation. Constructs 4 and 5 were designed to test the effect of blocking VQIINK and all but 1 of the VQIVYK surfaces. Mutant 4 (Q276W, I277M, L282R, Q307W, V309W) leaves only the dry interface of VQIVYK available for aggregation and mutant 5 (Q276W, I277M, L282R, I308W) leaves only the solvent accessible surface for aggregation. In addition, we tested the effect of D1b on blocking seeding by 3R tau, which lacks the VQIINK aggregation segment and leaves the VQIVYK interface intact (Figure 6D, Figure 13D-F—Supplement).

To test if specific interfaces are inhibited by D1b, fibrils were formed from all of the different mutants, and then each was incubated with the indicated concentration of D1b and used to seed wild type tau-K18 biosensor cells, as described previously with wild type tau fibrils. We found that D1b was most effective at inhibiting seeding by fibrils of mutants that left intact: interface A of VQIINK which is thought to involve aggregation at site I277 of tau, the solvent accessible interface of VQIVYK as well as 3R (Figure 6D). D1b also showed

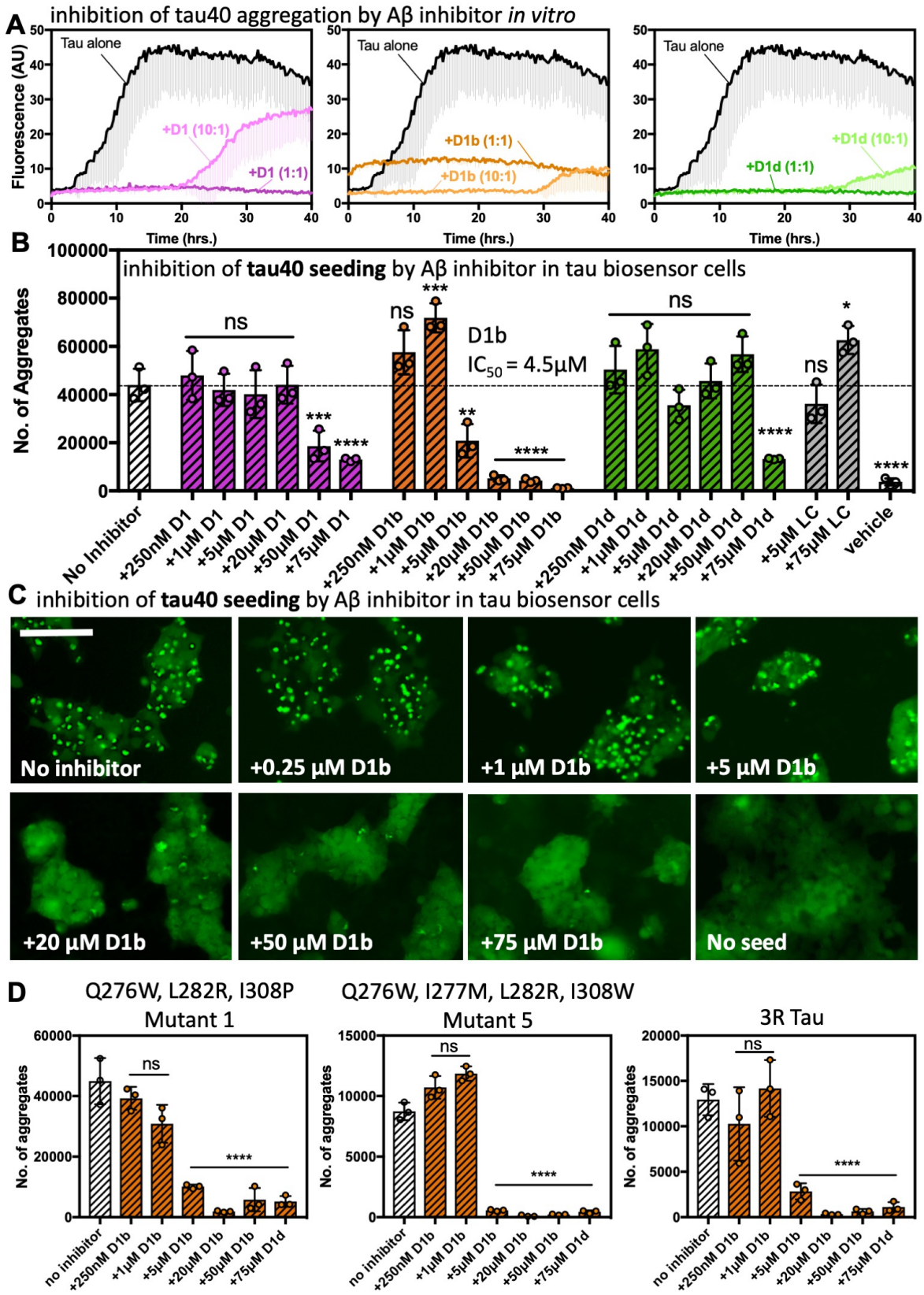

A
inhibition of tau40 aggregation by Aβ inhibitor *in vitro*
Fluorescence (AU)
Tau alone
+D1 (10:1)
+D1 (1:1)
+D1b (1:1)
+D1b (10:1)
+D1d (10:1)
+D1d (1:1)
Time (hrs.)
B
inhibition of **tau40 seeding** by Aβ inhibitor in tau biosensor cells
No. of Aggregates
D1b
IC50 = 4.5µM
ns
No Inhibitor
+250nM D1
+1µM D1
+5µM D1
+20µM D1
+50µM D1
+75µM D1
+250nM D1b
+1µM D1b
+5µM D1b
+20µM D1b
+50µM D1b
+75µM D1b
+250nM D1d
+1µM D1d
+5µM D1d
+20µM D1d
+50µM D1d
+75µM D1d
+5µM LC
+75µM LC
vehicle
C
inhibition of **tau40 seeding** by Aβ inhibitor in tau biosensor cells
No inhibitor
+0.25 µM D1b
+1 µM D1b
+5 µM D1b
+20 µM D1b
+50 µM D1b
+75 µM D1b
No seed
D
Q276W, L282R, I308P
Mutant 1
Q276W, I277M, L282R, I308W
Mutant 5
3R Tau
No. of aggregates
no inhibitor
+250nM D1b
+1µM D1b
+5µM D1b
+20µM D1b
+50µM D1b
+75µM D1d

Figure 6. Aβ inhibitors also reduce fibril formation and seeding by tau40. A. Peptide inhibitors D1, D1b, and D1d reduce fibril formation of tau40. 10 μM tau40 monomer was incubated at a 1:10, 1:1, or 10:1 molar ratio to each inhibitor with 0.5mg/ml heparin under shaking conditions at 700 RPM at 37 °C. Fibril formation was monitored using ThT fluorescence. Plots show the average of three technical replicates with one standard deviation below. **B**, **C**. The effects of the inhibitors on seeding by tau40 fibrils in tau-K18CY biosensor cells. The cells were seeded with 250 nM tau40 fiber (final concentration); in samples with inhibitor, tau40 fibers were incubated with indicated final concentrations of peptide inhibitor for one hour prior to addition to cells. **B.** Average number of aggregates at the indicated inhibitor concentrations, Bars represent mean with individual technical replicates (n = 3; ns = not significant; *, p < 0.02; ***, p < 0.0005; ****, p < 0.0001 using an ordinary one-way ANOVA relative to leftmost column). dotted line represents number of aggregates from untreated tau40 fibrils. IC_{50} value was calculated from the dose–response plot of inhibitor D1b. **C**. Representative images of effect of D1b on seeding. Cells are shown at 10X magnification, scale bar 100 μm. **D.** Seeding from tau interface mutation fibrils in tau-K18CY biosensor cells is reduced by D1b. Experiment was performed as above. Average number of normalized aggregates at the indicated inhibitor concentrations, Bars represent mean with individual technical replicates (n = 3; ns = not significant; ****, p < 0.0001 using an ordinary one-way ANOVA relative to leftmost column).

moderate inhibition of several other tau mutants, but required high concentrations to inhibit seeding (Figure 13D—Supplement). As a control, we tested seeding by a mutant of tau40 that combined all of the different mutations, and found this mutant did not induce any seeding in tau-K18 biosensor cells (Figure 13E—Supplement), indicating that at least one of the known interfaces is needed for seeding. Control inhibitor LC has little to no effect on seeding from any construct (Figure 13F—Supplement). Taken together, these data show that both the VQIINK and VQIVYK aggregation segments of tau are inhibited by D1b, and suggest that each may share common structural features with the Aβ core that could allow for cross-seeding of tau by Aβ.

Designed inhibitor D1b targets disease relevant conformations

Amyloid polymorphs may differ depending on whether they were aggregated *in vitro* or extracted from human brain tissue (56). We sought to determine if our inhibitors are capable of blocking pathological forms of either tau, or Aβ. As suggested previously in our conformational antibody assay and structural alignment (Figure 3C), we hypothesized that our inhibitors would block disease-relevant amyloid polymorphs. Since we also found that our inhibitors blocked both homotypic and heterotypic tau seeding by aggregated tau and Aβ, we tested our inhibitor series on crude lysate from AD donor patient brain tissue.

We homogenized tissue from three different brain regions of a single AD patient brain, corresponding to early (hippocampal), middle (frontal cortex), and late (occipital lobe) stage affected areas. We also prepared samples from patient tissue with progressive supranuclear palsy (PSP), which is a tau aggregation disease that displayed no Aβ aggregation by immunostaining. We transfected brain lysates into the biosensor cells; samples with inhibitor were treated with 10 μM D1, D1b, or D1d.

We found that treating the brain-derived lysates with D1b significantly reduced seeding by all tested brain tissue samples (Fig. 7). D1b treatment reduced seeding in all stages of AD brain, with more pronounced effects in areas affected later in the disease. Although our inhibitor D1b showed reduction of seeding in the hippocampal sample, the fibril load of this region due to the late stage of the patient may have been too great to have been efficiently halted by the dose used. Interestingly, the PSP tauopathy tissue was also responsive to treatment with each of the inhibitors, with D1b displaying the most pronounced inhibition. We surmise that D1b recognizes a common toxic epitope found in both Aβ, and in a variety of tau polymorphs.

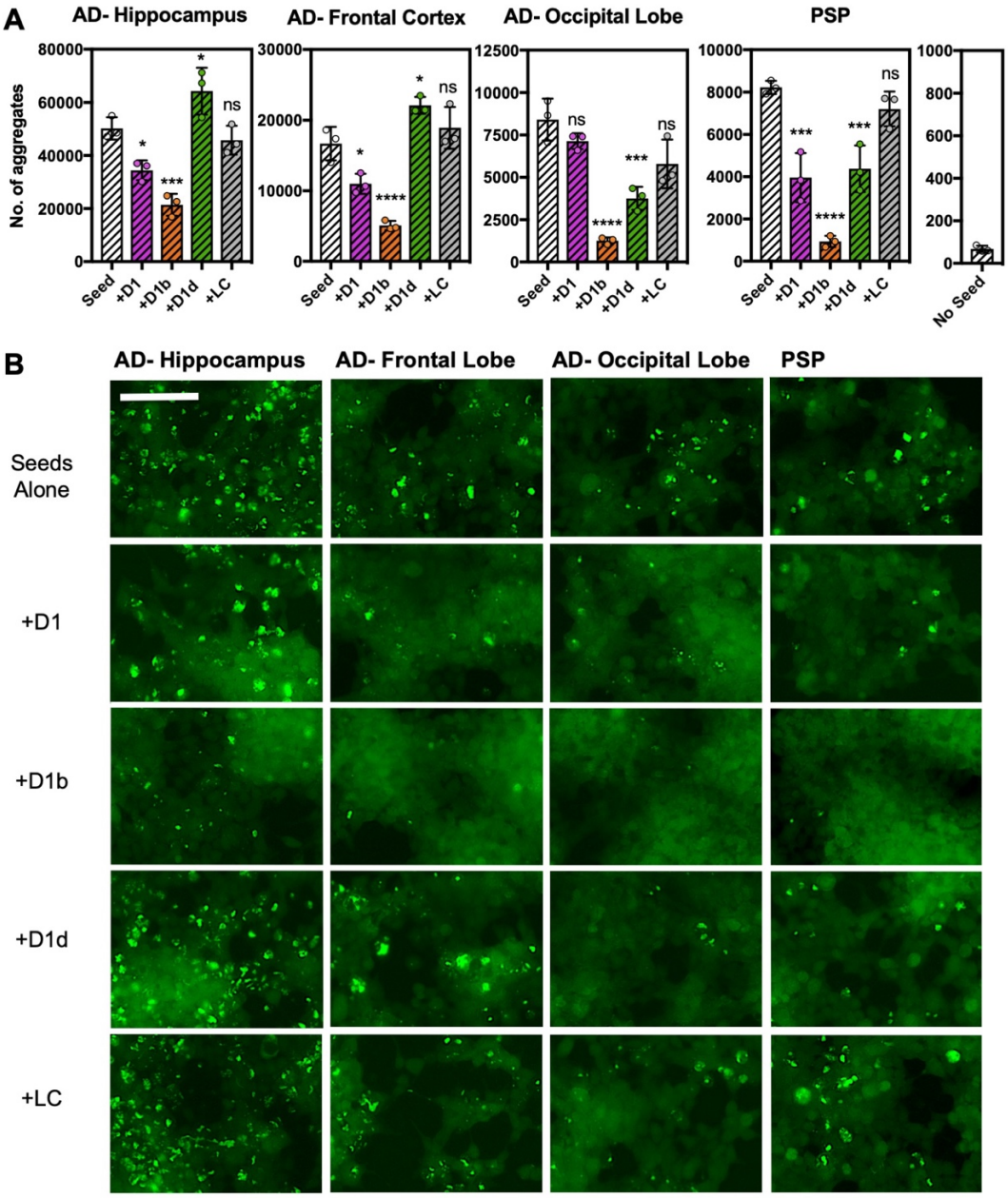


Figure 7. Peptide inhibitors reduce seeding by crude brain-extract from tauopathy donor tissue. Brain lysate was prepared in TBS buffer from 3 brain regions of one AD patient, and from a one sample of a PSP patient lacking Aβ plaques. Cells were seeded with a 1/400 dilution of brain tissue lysate; for samples with inhibitor, lysates were incubated with inhibitor overnight prior to addition to cells. A concentration of 10 μM peptide was used for all of the experiments shown. **A.** The average number of aggregates seeded by lysate from each respective brain region, with or without addition of inhibitors. Bars represent mean with individual technical replicates (n = 3; ns = not significant; *, $p < 0.05$; ***, $p < 0.0005$; ****, $p < 0.0001$ using an ordinary one-way ANOVA relative to leftmost column). **B**. Representative images of seeded biosensor cells from A shown at 10X magnification, scale bar 100 μm.

Discussion

The search for druggable targets in AD is muddied by the numerous proteins involved and incomplete understanding of whether or not the two histological protein hallmarks, Aβ and tau, interact directly with each other. On top of this, Aβ, the apparent initiator of the disease, aggregates into a wide variety of species, from soluble oligomers ranging from dimers to those that contain dozens of copies, to polymorphic fibril deposits. While there may be numerous toxic assemblies, targeting a specific sequence or structure of a toxic motif that is present in a variety of these assemblies could be an effective strategy for designing pharmaceuticals.

We targeted the amyloid core segment of Aβ due to its defined amyloidogenicity, and putative interaction with the late-stage aggregating protein, tau. We focused our efforts on the $A\beta_{16\text{-}26}$ segment with a hereditary mutation D23N, whose structure we determined by MicroED. Although the structure of this segment is fibrillar, and resembles a previously observed zipper interface, the out-of-register interface of the β-strands suggests that portions of this conformation may be present in a number of toxic oligomeric intermediates as well as in fibrils. We successfully used this structure to design a series of related inhibitors that reduce toxicity of Aβ in model N2a cells.

Our biochemical and toxicity studies indicate that these inhibitors function in two ways. The first is by preventing monomeric Aβ from aggregating. The second is by reducing toxicity of pre-formed oligomeric Aβ, possibly by binding to and blocking a surface that is responsible for conferring toxicity or seeding. While all of our designed inhibitors prevent monomeric Aβ from aggregating, only the longer D1b and D1d versions are effective at reducing toxicity of preformed assemblies. These two peptides were designed by

extending the C-terminus. D1b and D1d could conceivably act by obscuring resides important for conferring toxicity, as supported by early onset hereditary mutations clustering at residues 21-23 (57–59).

Our data implicate an extended Aβ core in the spread of the disease, because targeting inhibitors to this region appears to block the templating interface needed to cross-seed tau. Aβ fibers treated with D1b showed a dramatic reduction of cross seeding in tau-K18 biosensor cells. Tau fibers treated with D1b showed similarly inhibited seeding in biosensor cells. The dual efficacy of the inhibitor D1b designed against the 16-23 region of Aβ suggests that these two pathological aggregates, Aβ and tau, share a common structural motif and aggregation pathway in AD. By using mutant constructs of tau with only one available amyloid interface, we were able to determine two interfaces on tau where seeding was highly reduced by D1b. Both the R2 and R3 amyloid-prone regions of tau contain a D1b sensitive interface. Of note, the surface of R2 blocked by D1b contains residue I277, which previously has been shown to be critical for tau aggregation (60). We find that overlaying our Aβ segment crystal structure with structures of tau R2 and R3 reveals a high degree of structural similarity both in the backbone, and also apparently in the complementarity of sidechains from each to intrinsically interdigitate (Figure 14—Supplement, supplementary methods). These models support the hypothesis that Aβ and tau may interact with favorable energy to form a stable heterozipper. Interestingly, Aβ overlays well with these regions of tau in both parallel and anti-parallel orientations, suggesting that either fiber or smaller oligomers could be capable of cross seeding. On this basis, we suggest that the amyloid core of Aβ and the regions VQIINK and VQIVYK form similar structures in AD that are biochemically capable of cross-seeding.

Consistent with our finding that Aβ and tau share structural similarities, we found that the Aβ inhibitor D1b is able to reduce seeding from brain homogenates, indicating that the inhibitor is recognizing a disease-related structural motif, while D1 and D1d are much less effective. It is curious that seeding by both AD and PSP is greatly reduced by the inhibitor D1b, as PSP pathology does not include Aβ aggregates. It is thought that different disease phenotypes, which display distinct fiber morphologies commonly referred to as strains, are determined by the formation of different steric zipper cores (61). Thus, PSP fibers may contain a different core than our in vitro aggregated tau or AD derived tau. However, our tau mutagenesis results suggest that inhibitor D1b can recognize at least 2 unique core interfaces, and thus could be able to act on multiple strains of tau fibers.

Similar to other peptide-based amyloid inhibitors, the effective dose to reduce toxicity of aggregated species is higher than to delay aggregation of monomeric species. This is emphasized by the differing efficacies of our related inhibitor series, where some inhibitors were able to prevent initial aggregation, but not toxicity or seeding from various assemblies. It appears that inhibitors to prevent an aggregation nucleus are much more promiscuous than those that ameliorate toxicity by binding to a distinct structure. This trend was observed in both Aβ and tau, suggesting a common inhibitory mechanism for both proteins, and highlights the need for multiple experimental measures to validate inhibitor efficacy.

In summary, our results suggest that a direct interaction between the Aβ core and the amyloid-prone regions of tau facilitates cross seeding. Our inhibitors designed for the Aβ core segment prevent cross seeding of tau, as well as tau homotypic seeding. The entwined nature of these two proteins in AD suggests it is necessary to control aggregation of both in

order to treat the disease. Early detection is still crucial, but these data provide a platform on which further inhibitors can be designed for optimized inhibition of amyloid seeding in Alzheimer's disease.

Experimental Procedures

Recombinant Amyloid Beta Peptide purification- Aβ was purified as described in Krotee et. Al (47) After purification, the protein was lyophilized. Dried peptide powders were stored in desiccant jars at -20˚C.

Peptide Preparation- Candidate inhibitors were custom made and purchased from Genscript (Piscataway, NJ). Lyophilized candidate inhibitors were dissolved at 10mM in 100% DMSO. 10mM stocks were diluted as necessary. All stocks were stored frozen at -20°C.

Amyloid Beta was prepared by dissolving lyophilized peptide in 100% DMSO or 100mM NaOH. Next, the sample was spin-filtered and the concentration was assessed by BCA assay (Thermo Scientific, Grand Island, NY). The DMSO or NaOH peptide stocks were diluted 100-fold in filter-sterilized Dulbecco's PBS (Cat. # 14200-075, Life Technologies, Carlsbad, CA).

Crystallization- 16-Ac-KLVFFAENVGS-NH_3-26 (Aβ 16-26 D23N) was dissolved at 4.5 mg/ml in 20% DMSO. Micro crystals were grown in batch in 0.2M magnesium formate, 0.1M Tris base pH 8.0, and 15% isopropanol at room temperature under quiescent conditions. Crystals grew within 4 days to a maximum of 2 weeks.

MicroED data collection- The procedures for MicroED data collection and processing largely follow published procedures (62, 63). Briefly, a 2-3 μl drop of crystals in suspension

was deposited onto a Quantifoil holey-carbon EM grid then blotted and vitrified by plunging into liquid ethane using a Vitrobot Mark IV (FEI, Hillsboro, OR). Blotting times and forces were optimized to keep a desired concentration of crystals on the grid and to avoid damaging the crystals. Frozen grids were then either immediately transferred to liquid nitrogen for storage or placed into a Gatan 626 cryo-holder for imaging. Images and diffraction patterns were collected from crystals using FEI Tecnai 20 TEM with field emission gun (FEG) operating at 200 kV and fitted with a bottom mount TVIPS TemCam-F416 CMOS-based camera. Diffraction patterns were recorded by operating the detector in a video mode using electronic rolling shutter with 2 x 2 pixel binning (64). Exposure times for these images were either 2 or 3 seconds per frame. During each exposure, crystals were continuously unidirectionally rotated within the electron beam at a fixed rate of 0.3 degrees per second, corresponding to a fixed angular wedge of 0.6 or 0.9 degrees per frame.

Crystals that appeared visually undistorted produced the best diffraction. Datasets from individual crystals were merged to improve completeness and redundancy. Each crystal dataset spanned a wedge of reciprocal space ranging from 40-80°. We used a selected area aperture with an illuminating spot size of approximately 1 μm. The geometry detailed above equates to an electron dose rate of less than 0.01 $e^{-}/Å^{2}$ per second being deposited onto our crystals.

Measured diffraction images were converted from TIFF format into SMV crystallographic format, using publicly available software (available for download at http://cryoem.janelia.org/downloads).

We used XDS to index the diffraction images and XSCALE (65) for merging and scaling together datasets originating from thirteen different crystals.

Structure determination- We determined the structure of Aβ 16-26 D23N using molecular replacement. KLVFFA (pdb 2Y2A) led us to our atomic model. The solution was identified using Phaser (66). Subsequent rounds of model building and refinement were carried out using COOT and Phenix, respectively (67, 68). Electron scattering factors were used for refinement. Some reflections extended to 1.40 Å resolution. Calculations of the area buried and Sc were performed with AREAIMOL (69, 70)) and Sc (71–73), respectively.

Computational structure-based design- Computational designs were carried out using the RosettaDesign software as described previously (74). The atomic structure of the 16-KLVFFAENVGS-26 Aβ segment was used as a starting template for computational design. An extended L-peptide (or D-peptide, six to eight residues) was first placed at the end of the starting template of atomic structure. The design procedure then built side-chain rotamers of all residues onto the nine-residue peptide backbone placed at growing end of fibril. The optimal set of rotamers was identified as those that minimize an energy function containing a Lennard-Jones potential, an orientation-dependent hydrogen bond potential, a solvation term, amino acid-dependent reference energies, and a statistical torsional potential that depends on the backbone and side-chain dihedral angles. Area buried and shape complementarity calculations were performed with areaimol and Sc, respectively, from the CCP4 suite of crystallographic programs (69). The solubility of each peptide was evaluated by hydropathy index (75). The designed peptides were selected based on calculated binding energy of top or bottom binding mode, shape complementarity and peptide solubility. Each structural model of selected peptides went through human

inspection using Pymol, where those peptides with sequence redundancy and less binding interactions were omitted. Finally, select peptides were synthesized and tested experimentally.

Sample preparation for electron microscopy- Aβ1-42 was dissolved and diluted as previously described. Inhibitor stocks were prepared in 100% DMSO and were added such that the sample contained 10 μM monomeric Aβ1-42 the indicated ratio of inhibitor with final concentration of 1% DMSO. Samples were incubated for 72 hours at 37°C under quiescent conditions. Aβ1-42 fibrils were formed as described, and then treated with indicated ration of inhibitor for 24 hours at 37°C under quiescent conditions. Fibril abundance was checked using electron microscopy.

Transmission electron microscopy-Samples were spotted onto non-holey grids and left for 160 to 180 seconds. Remaining liquid was wicked off and then left to dry before analyzing. Samples for negative-stain TEM were treated with 2% uranyl acetate after sample was wicked off the grid. After 1 minute, the uranyl acetate was wicked off. The grids were analyzed using a T12 Electron Microscope (FEI, Hillsboro, OR). Images were collected at 3,200 or 24,000x magnification and recorded using a Gatan 2kX2k CCD camera.

Thioflavin-T (ThT) kinetic assays- Thioflavin-T (ThT) assays were performed in black 96-well plates (Nunc, Rochester, NY) sealed with UV optical tape. The total reaction volume was 150 μL per well. Aβ1-42 was prepared as described. Inhibitors were added at indicted concentrations, with a final concentration of 1%DMSO. ThT fluorescence was recorded with excitation and emission of 444 nm and 482 nm, respectively, using a Varioskan Flash (Thermo Fisher Scientific, Grand Island, NY). Experiments were performed at 37°C without shaking in triplicate and readings were recorded every 5 minutes. ThT assays with tau40

were prepared as above with the following exceptions. 0.5mg/mL heparin (Sigma cat. no. H3393) was added to the reaction mixture and experiments were performed at 37°C with double orbital shaking at 700 rpm. Seeding assay included 10% monomer equivalent of preformed fibrils, sonicated for 10 minutes prior to addition.

Cell culture- Neuro2a (N2a) cells were a gift from the Pop Wongpalee in the laboratory of Douglas Black at UCLA. Cells were cultured in MEM media (Cat. # 11095-080, Life Technologies) plus 10% fetal bovine serum and 1% pen-strep (Life Technologies). Cells were cultured at 37°C in 5% CO2 incubator.

3-(4,5-dimethylthiazol-2-yl)-2,5-diphenyltetrazolium bromide (MTT) dye reduction assay for cell viability- N2a cells were plated at 5,000 cells per well in 90 µL of culture media, in clear 96-well plates (Cat. # 3596, Costar, Tewksbury, MA). Cells were allowed to adhere to the plate for 20-24 hours. Aβ1-42 samples were incubated at 10µM with or without inhibitors at varying ratios for 12 hours at 37°C and then applied to N2a cells. 10 µL of sample was added to cells. By doing this, samples were diluted 1/10 from in vitro stocks. Experiments were done in triplicate.

After a 24-hour incubation, 20 µL of Thiazolyl Blue Tetrazolium Bromide MTT dye (Sigma, St. Louis, MO) was added to each well and incubated for 3.5 hours at 37°C under sterile conditions. The MTT dye stock is 5 mg/mL in Dulbecco's PBS. Next, the plate was removed from the incubator and the MTT assay was stopped by carefully aspirating off the culture media and adding 100 µL of 100% DMSO to each well. Absorbance was measured at 570 nm using a SpectraMax M5. A background reading was recorded at 700 nm and subsequently subtracted from the 570 nm value. Cells treated with vehicle alone (PBS+0.1%DMSO) were designated at 100% viable and cells treated with 100% DMSO designated as 0% viable, and cell viability of all

other treatments was calculated accordingly. We employed one-way ANOVA as our statistical test for significance.

Dot Blot Assay- Aβ1-42 samples were incubated at 10 μM with or without inhibitors for 6, 24, and 72 hours at 37°C, and spotted onto a nitrocellulose membrane (Cat. # 162–0146, BioRad, Hercules, CA). 20μL was loaded for each condition; 2μL was spotted at a time and allowed to dry between application. The membranes were blotted as previously described (76), with the exception of the primary antibodies used. The antibodies used in the assay were previously generated and characterized (51).

Surface Plasmon Resonance (SPR)- SPR experiments were performed using BiacoreT200 instrument (GE Healthcare). Aβ42 fibrils/tau K18 fibrils were immobilized on a CM5 sensor chip. The fibrils of Aβ42 were prepared by placing a sample of 50 μM Aβ42 in PBS pH 7.4 in two wells of a Nunc 96-well optical bottom plate (Thermo Scientific), 150 μl/well and incubating the plate in a microplate reader (FLUOstar Omega, BMG Labtech) at 37 °C with double orbital shaking at 600 rpm overnight. Sample from the two wells were pooled together and Aβ42 fibrils were isolated from the incubation mixture by centrifuging it at 13,000 xg, 4°C for 45 minutes. The supernatant was removed and the pellet was re-dissolved in an equal volume of PBS as that of supernatant. The isolated fibrils were sonicated using a probe sonicator for 1-2 minutes at 18% amplitude with 2 sec on, 5 sec off pulses. The sonicated fibrils were filtered through a 0.22 μ filter to remove large aggregates. The sonicated and filtered fibrils were diluted to 60 μg/ml in 10 mM NaAc, pH 3 and then, immobilized immediately on a CM5 sensor chip using standard amine coupling chemistry. Briefly, the carboxyl groups on the sensor surface were activated by injecting 100 ul of 0.2 M EDC and 0.05 M NHS mixture over flow cells 1–2. The fibrils were then

injected at a flow rate of 5 µl/min over flow cell 2 of the activated sensor surface for 900 seconds. The remaining activated groups in both the flow cells were blocked by injecting 120 µl of 1 M ethanolamine-HCl pH 8. 5.. For the binding assay each peptide inhibitor was dissolved in 100 % DMSO at a concentration of 1 mM and diluted in PBS pH 7.4+1.2% DMSO to concentrations ranging from 5 µM to 260 µM. Each peptide was injected at a flow rate of 30 µl/min over both flow cells (1 and 2) at increasing concentrations (in running buffer, PBS, pH 7.4+1.2% DMSO) at 25°C. For each sample the contact time and dissociation time were 120 seconds and 160 seconds, respectively. 3 M NaCl was used as regeneration buffer. The data were processed and analyzed using Biacore T200 evaluation software 3.1. The data of flow cell 1 (blank control) was subtracted from the data of flow cell 2 (with immobilized fibrils/monomers). The equilibrium dissociation constant (Kd) was calculated by fitting the plot of steady-state peptide binding levels (Req) against peptide concentration (C) with 1:1 binding model (Eq 1).

Eq 1. $$Req = \frac{CR_{max}}{Kd + C} + RI$$

R_{max} = Analyte binding capacity of the surface
RI = Bulk refractive index contribution in the sample

Recombinant Tau purification-Human Tau40 (residues 1-441) WT, 3R and mutants: : interface A (Q276W, L282R, I308P), interface B (Q276W, I277M, I308P), interface C (I277M, L282R, I308P)interface 1 (Q276W, I277M, L282R, Q307W, V309W), interface 2 (Q276W, I277M, L282R, I308W), were expressed in pET28b with a C-terminal His-tag in BL21-Gold E. coli cells grown in TB to an OD600 = 0.8. Cells were induced with 0.5 mM IPTG for 3 hours at 37°C and lysed by sonication in 50 mM Tris (pH 8.0) with 500 mM NaCl, 20 mM imidazole, 1 mM beta-mercaptoethanol, and HALT protease inhibitor. Cells were lysed by sonication,

clarified by centrifugation at 15,000 rpm for 15 minutes, and passed over a 5 ml HisTrap affinity column. The column was washed with lysis buffer and eluted over a gradient of imidazole from 20 to 300 mM. Fractions containing purified Tau40 were dialyzed into 50 mM MES buffer (pH 6.0) with 50 mM NaCl and 1 mM beta-mercaptoethanol and purified by cation exchange as described for K18. Peak fractions were polished on a HiLoad 16/600 Superdex 200 pg in 1X PBS (pH 7.4), and concentrated to ~20-60 mg/ml by ultrafiltration using a 10 kDa cutoff.

Fibril incubation with inhibitors for tau biosensor cell-seeding assays. Aβ fibrils were prepared at 200 μM at 37°C for 72 hours before diluting to 50 μM in PBS buffer (pH 7.4) for seeding experiments. Tau40 WT and interface mutation fibrils were prepared by shaking 50 μM tau40 in PBS buffer (pH 7.4) with 0.5 mg/ml heparin (Sigma cat. no. H3393) and 1 mM dithiothreitol (DTT) for 3–6 days. Fibrillization was confirmed with an endpoint ThT reading, and fibrils were then diluted 20-fold to 1.25 μM in OptiMEM (Life Technologies, cat. no. 31985070). Inhibitors dissolved in DMSO were added to 20 μl of diluted fibrils at a concentration 20-fold greater than the final desired concentration. Fibrils were incubated for ~16 h with the inhibitor, and subsequently were sonicated in a Cup Horn water bath for 3 min before seeding the cells. The resulting 'pre-capped fibrils' were mixed with one volume of Lipofectamine 2000 (Life Technologies, cat. no. 11668027) prepared by diluting 1 μl of Lipofectamine in 19 μl of OptiMEM. After 20 min, 10 μl of fibrils were added to 90 μl of the tau-K18CY biosensor cells to achieve the final indicated ligand concentration. Quantification of seeding was determined by imaging the entire well of a 96-well plate seeded in triplicate and imaged using a Celigo Image Cytometer (Nexcelom) in the YFP channel. Aggregates were counted using ImageJ (77) by subtracting the background fluorescence from unseeded cells and then counting the number of peaks with fluorescence above background using the built-in

Particle Analyzer. Dose-response curves were constructed for inhibitor peptides exhibiting concentration dependence by fitting to a nonlinear regression model in Graphpad Prism. High resolution images were acquired using a ZEISS Axio Observer D1 fluorescence microscope.

Preparation of Brain lysate. Human brain tissue was obtained from the Neuropathology Laboratory at UCLA Medical Center. AD and PSP cases were confirmed by the Neuropathology Laboratory by immunostaining autopsied brain tissue sections, and the PSP donor was confirmed to be free of amyloid immunoreactivity. Tissue sections from the indicated brain regions were manually homogenized using a disposable ultra-tissue grinder (Thermo Fisher) in TBS (pH 7.4) supplemented with 1X HALT protease inhibitor. Homoginzed tissue was aliquoted to several PCR tubes and prepared for seeding in biosensor cells by sonication as described by Kaufman et al. (78), except tissue sections were sonicated twice as long, for a total of 2 h, in an ice cooled circulating water bath with individual sample tubes stirring to ensure each tube received the same sonication energy. Subsequently, seeding was measured by transfection into biosensor cells and quantified as described above.

ACKNOWLEDGEMENTS

We thank M. Diamond for gifting the monoclonal biosensor HEK293 cell-line that expressed tau-K18 (P301S) EYFP for our inhibitor assay. We thank Dr. Vinters and Christopher K. Williams for supplying patient tissue and immunohistological summaries of tissues. We thank Dan Anderson for general support in the laboratory. We thank Lorena Saelices for providing TTR fibers and Qin Cao for providing TDP-43 fibers. We thank Lin

Jiang for helpful conversation regarding Aβ toxicity. We thank the UCLA-DOE X-ray Crystallography Core Technology Center; the Janelia Research Campus visitor program and Ivo Atanasov and the Electron Imaging Center for NanoMachines (EICN) of California NanoSystems Institute (CNSI) at UCLA for the use of their electron microscopes. The UCLA-DOE X-ray Crystallization Core Technology Center is supported in part by the Department of Energy grant DE-FC0302ER63421. The Gonen laboratory is funded by the Howard Hughes Medical Institute.

COMPETING INTERESTS

DSE is a SAB member and equity holder in ADRx, Inc.

AUTHOR CONTRIBUTIONS

SLG conceived and designed this study, interpreted results and wrote the manuscript. SLG crystallized, solved and analyzed Aβ 16-26 D23N, purified Aβ1-42, performed the ThT aggregation assays, prepared Aβ samples for toxicity, biosensor cell, and dot blot assays, and performed TEM experiments and structural overlays. PS performed and interpreted tau biosensor cell experiments, prepared brain extracts, and purified all tau constructs. JB cultured cells, executed and analyzed toxicity experiments, and purified alpha synuclein. KM designed inhibitors for Aβ 16-26 D23N and performed biosensor seeding controls. SS preformed and analyzed the SPR experiment. TPY performed tau interface mutant biosensor experiments. JAR screened crystals and collected MicroED data of Aβ16-26 D23N. MRS helped solve and analyze the Aβ 16-26 D23N structure, and calculate structural overlays. DC helped solve and analyze the Aβ 16-26 D23N structure. TG and DS acquired

and analyzed MicroED diffraction data. JS and CGG generated essential material for experiments and performed and analyzed the dot blot assay. DSE conceived the idea for the project, secured funding, interpreted results and revised the manuscript. All authors reviewed the results and approved the final version of the manuscript.

FOOTNOTES

This project was supported by the National Institutes of Health (NIH) (R01 AG029430).

The abbreviations used are: AD, Alzheimer's disease; Aβ, amyloid-β; MicroED, Microcrystal Electron Diffraction; N2a, Neuro-2a; ThT, thioflavin- T; MTT, 3-(4,5-dimethylthiazol-2- yl)-2,5-diphenyltetrazolium bromide; R2, repeat 2; R3, repeat 3.

The atomic coordinates and associated structure factors have been deposited in the Protein Data Bank 6O4J.

SUPPLEMENTARY MATERIALS

EXPERIMANTAL PROCEDURES

Aggregation Inhibition Assay with α-synuclein- α-synuclein was expressed and purified as described previously in Rodriguez, *et al.* with the following exceptions to the expression protocol. An overnight starter culture was grown in 15 mL instead of 100 mL, 7 mL of which was used to inoculate 1 L. After induction, cells were allowed to grown for 3-4 hours at 34 °C (instead of 4-6 hours at 30 °C). Cells were then harvested by centrifuging at 5,000 x g.

ThT assays with α-synuclein were performed in black 96-well plates (Nunc, Rochester, NY) sealed with UV optical tape. The total reaction volume was 180 μL per well. ThT fluorescence was recorded with excitation and emission of 444 nm and 482 nm, respectively, using a Varioskan Flash (Thermo Fisher Scientific, Grand Island, NY). Experiments were performed at 37°C, shaking at 600 rpm with a teflon bead, in triplicate and readings were recorded every 15 minutes. Alpha synuclein at 105 μM in PBS was diluted to a final concentration of 50 μM in 25 μM Thioflavin-T and PBS. Inhibitors were added at the specified concentration by diluting 10 mM stocks in 100% DMSO 1 to 40 in the same manner. Thus, inhibitors were tested at 5:1 molar excess of α-synuclein.

Aggregation Inhibition Assay with IAPP- Human IAPP1-37NH_2 (hIAPP) was purchased for Innopep (San Diego, CA). Peptides were prepared by dissolving lyophilized peptide in 100% 1,1,1,3,3,3-Hexafluoro-2-propanol (HFIP) at 250μM for 2 hours. Next, the sample was spin-filtered and then HFIP was removed with a CentriVap Concentrator (Labconco, Kansas City, MO). After removal of the HFIP, the peptide was dissolved at 1mM

or 10mM in 100% DMSO (IAPP alone) or 100% DMSO solutions containing 1mM or 10mM inhibitor. The DMSO peptide stocks were diluted 100-fold in filter-sterilized Dulbecco's PBS (Cat. # 14200-075, Life Technologies, Carlsbad, CA). Thioflavin-T (ThT) assays with hIAPP were performed in black 384-well plates (Nunc, Rochester, NY) sealed with UV optical tape. hIAPP1-37NH_2 and mIAPP1-37NH_2 were prepared as described. The total reaction volume was 150 µL per well. ThT fluorescence was recorded with excitation and emission of 444 nm and 482 nm, respectively, using a Varioskan Flash (Thermo Fisher Scientific, Grand Island, NY). Experiments were performed at 25°C without shaking in triplicate and readings were recorded every 5 minutes.

Atomic structure overlay- A structural superposition of Aβ 16-26 and tau (5V5B, 6HRE) was performed using LSQ from coot (78). We calculated root mean square deviation (RMSD) of main chains for parallel orientations fitting 6-8 resisdues. Anti-paprallel LSQ computation of Aβ 16-22 and tau 275-281 (5V5B) of C_α atoms was calculated, and side chain rotomers optimized with foldit (79) over 2000 iterations to minimize energy to -603 REU.

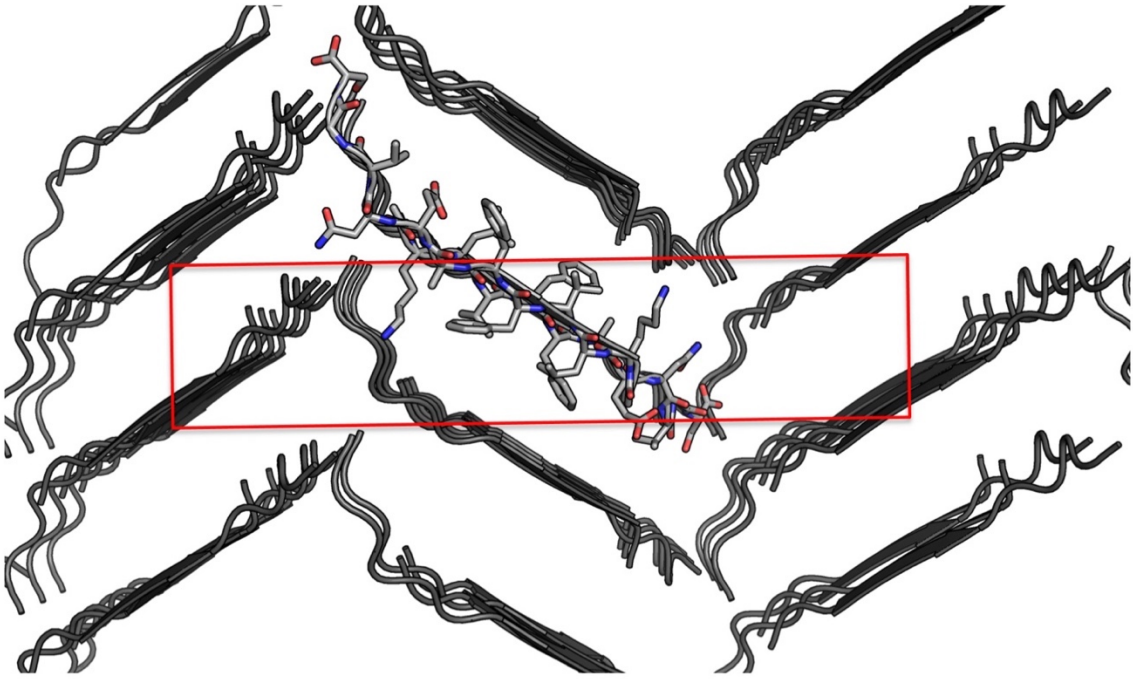


Figure 8. Crystal packing of the Aβ 16-26 D23N atomic structure. View down the ‘a’ axis of the unit cell, outlined in red.

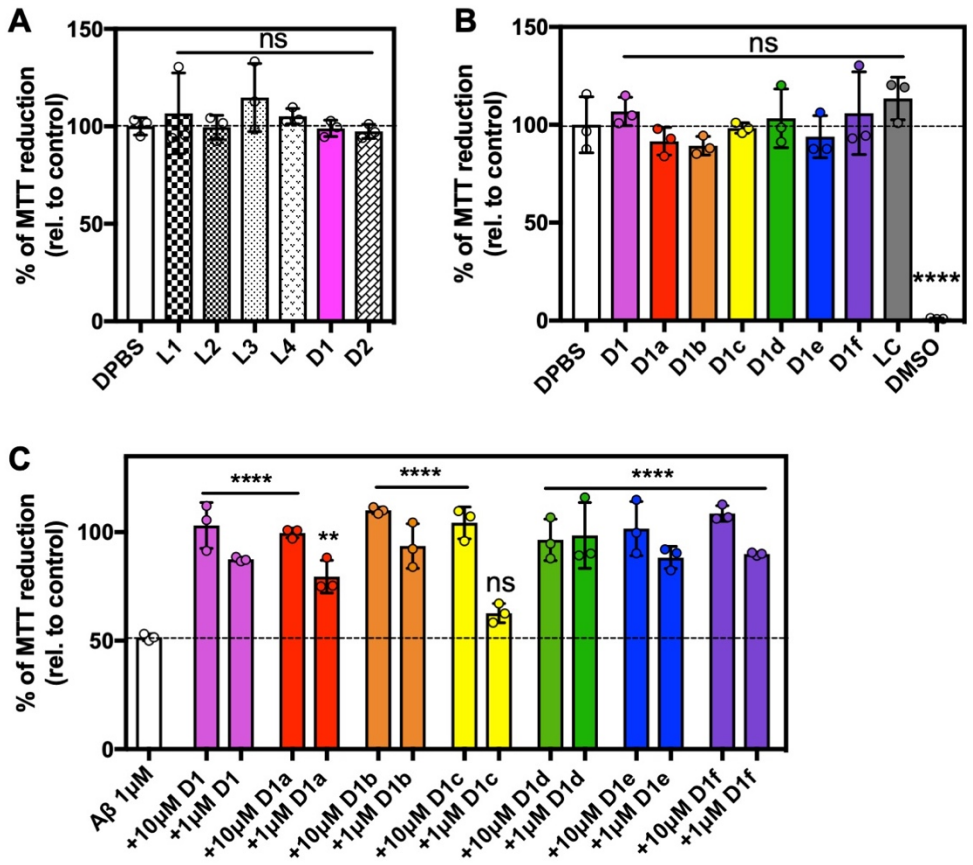


Figure 9. Extended Toxicity data **A, B.** Peptide inhibitors are not toxic. 100 μM of each peptide inhibitor was incubated for 12 hours at 37 °C and then diluted 1:10 with pre-plated N2a cells. Cytotoxicity was quantified using MTT dye reduction. Bars represent mean with individual technical replicates. **C.** Second generation peptide inhibitors reduce the cytotoxicity of Aβ1-42. 10 μM Aβ1-42 was incubated alone or with 10 μM and 100 μM of each peptide inhibitor for 12 hours at 37 °C and then diluted 1:10 with pre-plated N2a cells. Cytotoxicity was quantified using MTT dye reduction. (n = 3; ns = not significant; ****, $p < 0.0001$ using an ordinary one-way ANOVA relative to leftmost column).

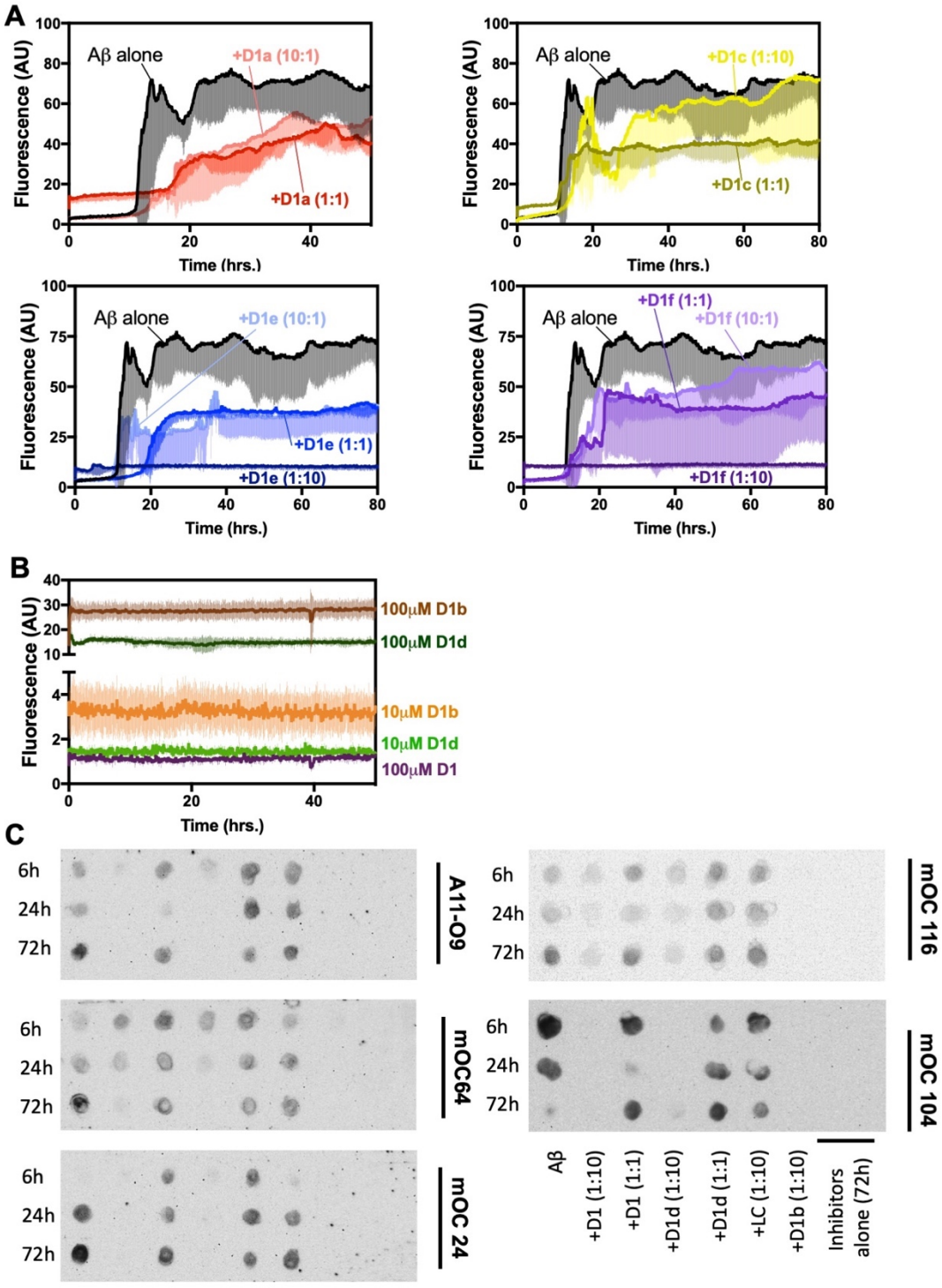


Figure 10. Peptide inhibitors D1a, D1c, D1e, and D1f are less effective ate reducing fibril formation of Aβ1-42, 10 μM of Aβ1-42 was incubated alone or at a 1:10, 1:1, or 10:1 molar ratio to each inhibitor under quiescent conditions at 37 °C. Fibril formation was monitored using ThT fluorescence. Lines show the average of three technical replicates with one standard deviation below. Inhibitors D1a and D1c are not shown at (1:10) ratio due to high

ThT signal from peptide self-association. **B.** Peptide inhibitors D1b and D1d self-associate at high concentrations. Peptide inhibitors were incubated at 10 μM and 100 μM under quiescent conditions at 37 °C. Fibril formation was monitored using ThT fluorescence. Lines show the average of three technical replicates with one standard deviation. **C.** Unspliced dot blots from figure 4C. Column key displayed at lower right is representative of all displayed blots.

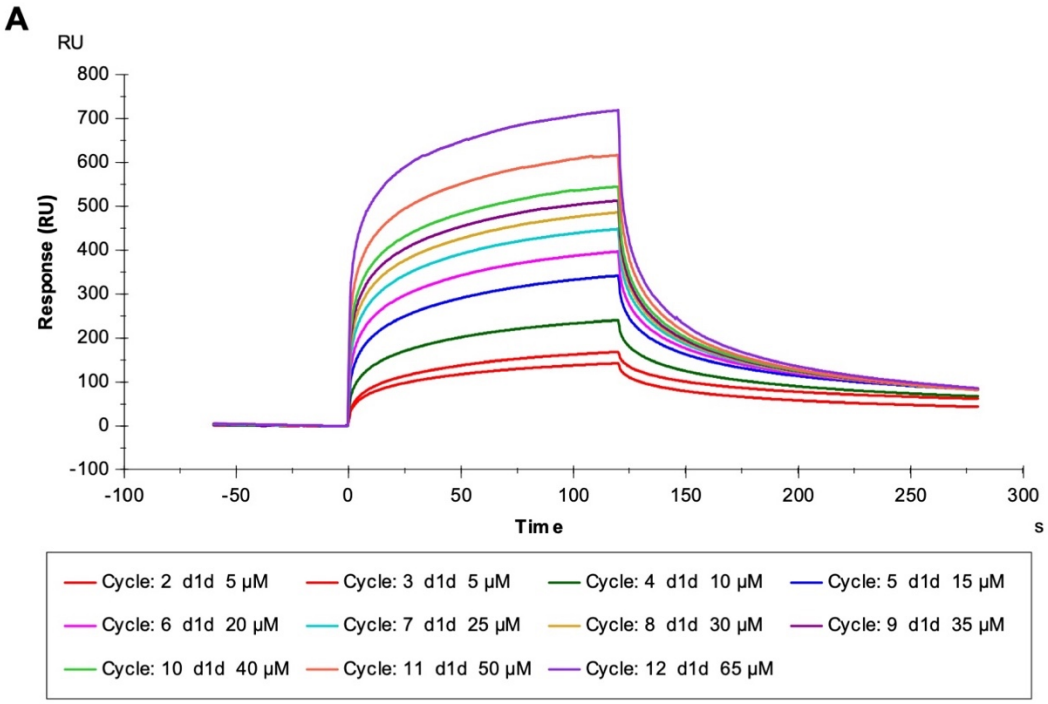


Figure 11. Representative Sensorgram obtained when D1d solutions at the indicated concentrations were flowed across the Aβ1-42 sensor chip.

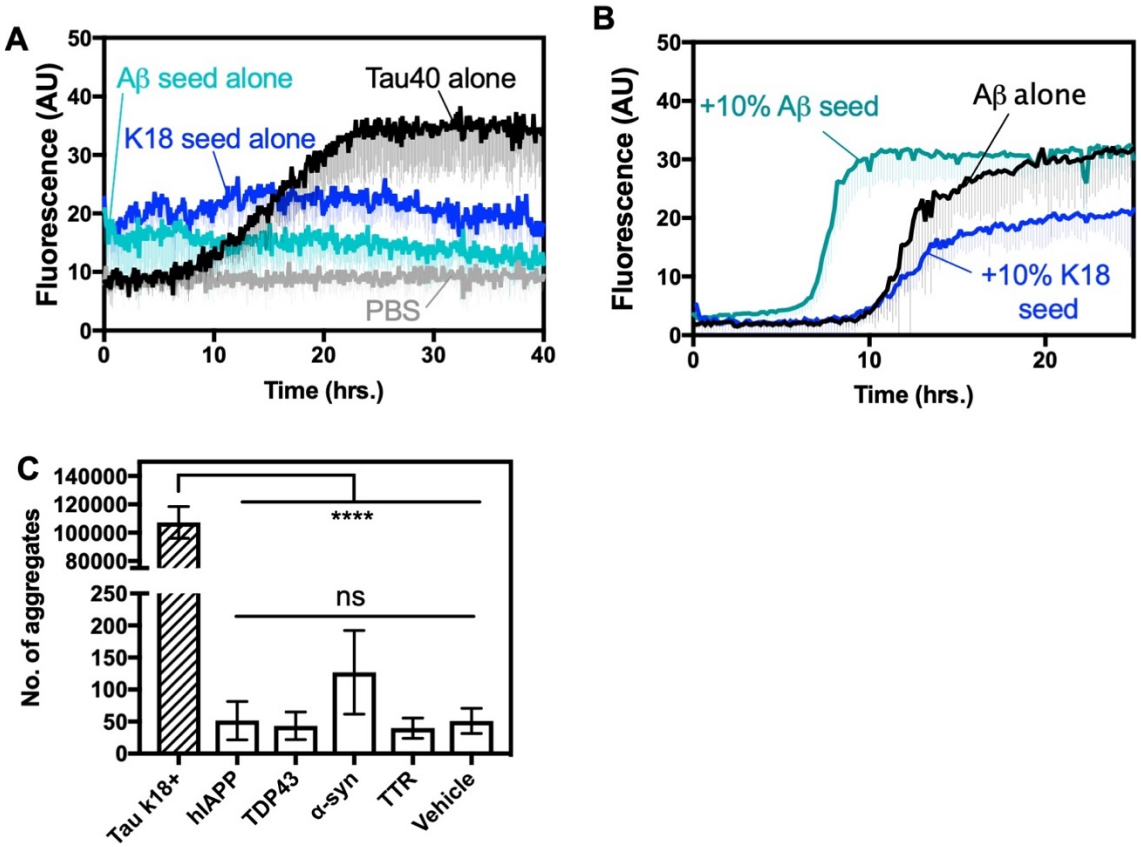


Figure 12. Extended ThT data of Tau seeding experiment. **A.** K18 and Aβ1-42 seeds have some baseline ThT signal. **B.** 10 μM Aβ1-42 was seeded with 10% monomer equivalent of pre-formed seed of Aβ1-42 or K18, under quiescent conditions at 37 °C. Fibril formation was monitored using ThT fluorescence. Lines show average of three technical replicates. **C.** The relative seeding efficiency of tau40 and other amyloid fibrils into the HEK293 biosensor that stably expresses K18 yellow fluorescent protein (YFP) fusion. The cells were seeded with 250 nM final concentration of amyloid fibril. (n = 3; ns = not significant; ****, p < 0.0001 using an ordinary one-way ANOVA relative to leftmost column or against all columns excluding leftmost, as indicated). Amyloid fibrils were confirmed by endpoint ThT or Electron Microscopy.

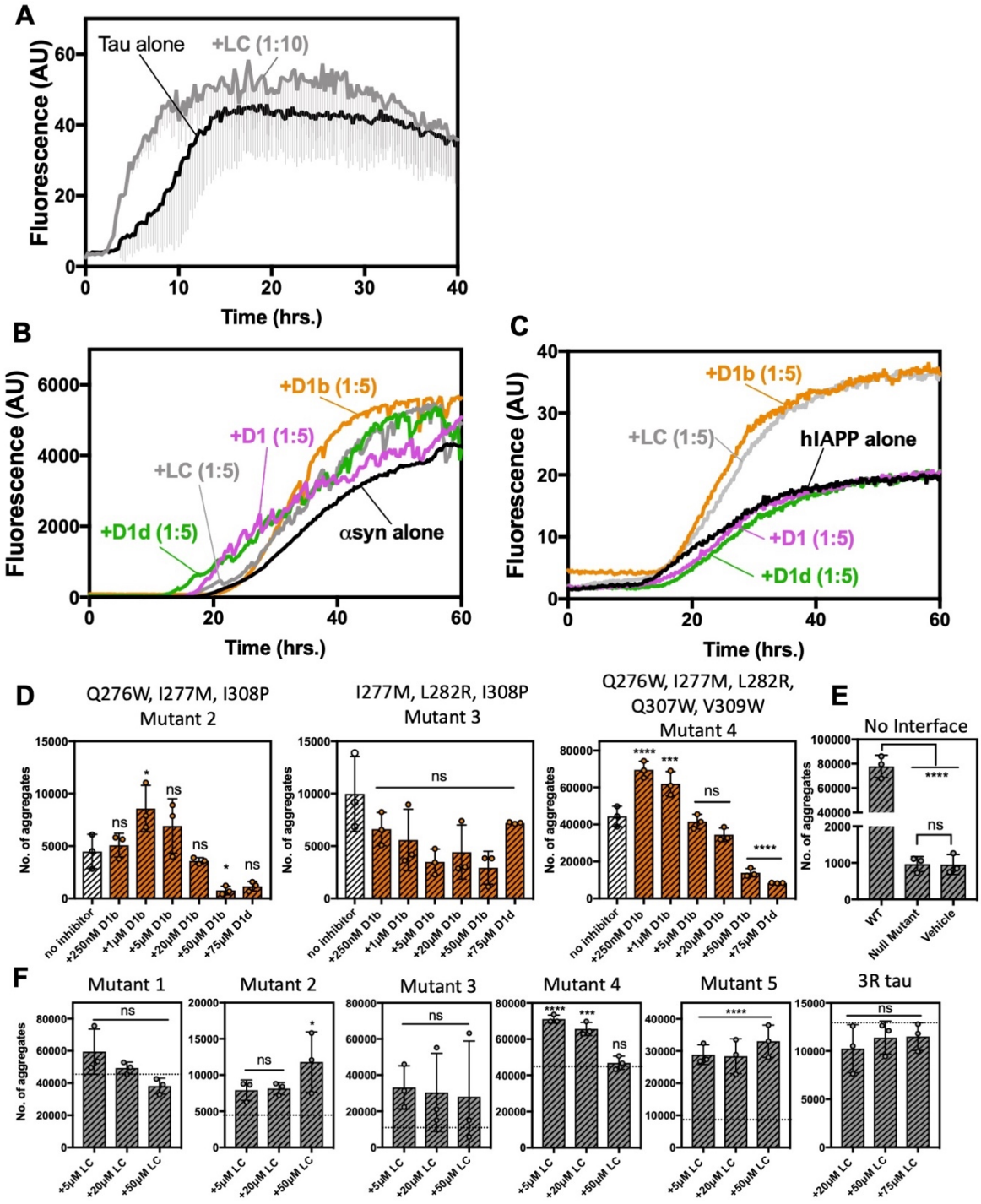


Figure 13. A. Control peptide inhibitor LC does not reduce fibril formation of tau40. 10 μM of tau40 was incubated at a 1:10 molar ratio to LC with 0.5mg/ml heparin under shaking conditions at 700 RPM at 37 °C. Fibril formation was monitored using ThT fluorescence. Lines show the average of three technical replicates with one standard deviation below. **B, C.** Designed inhibitors are not general amyloid inhibitors. **B**. 50 μM of α-synuclein was incubated at a 1:5 molar ratio to peptide inhibitors under shaking conditions at 700 RPM at

37 °C. Lines show the average of three technical replicates. **C.** 10 μM hIAPP was incubated at a 1:5 molar ratio to peptide inhibitors under quiescent conditions at 37 °C. Lines show the average of three technical replicates. **D, E, F.** Extended data of seeding by tau interface mutation fibrils in tau-K18CY biosensor cells. The cells were seeded with 250 nM tau40 fiber (final concentration); in samples with inhibitor, tau40 fibers were incubated with indicated final concentrations of peptide inhibitor for one hour prior to addition to cells. Average number of aggregates at the indicated inhibitor concentrations, Bars represent mean with individual technical replicates ($n = 3$; ns = not significant; *, $p < 0.05$; ***, $p < 0.0005$; ****, $p < 0.0001$ 0001 using an ordinary one-way ANOVA relative to leftmost column in D, relative as indicated in E, and relative to dotted line representing untreated fibrils in E).. **D**. Interface mutations less affected by D1b. **E.** Construct containing all interface mutations is seeding incompetent. **F.** Seeding interface mutants are not reduced by control inhibitor LC.

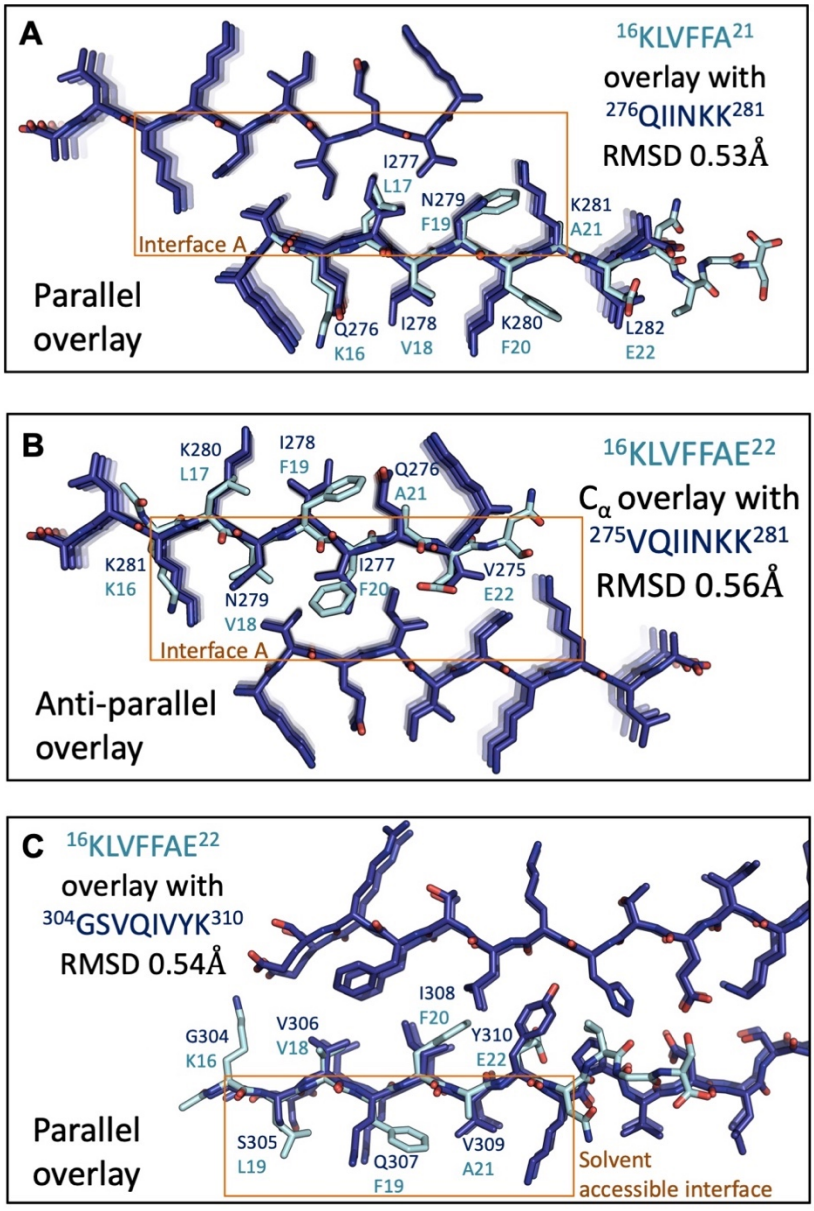


Figure 14. The spines of Aβ 16-26 D23N and tau are structurally similar. **A, B.** Aβ 16-26 D23N overlay with tau 274-283 in parallel and antiparallel orientations. **A.** 32 backbone atoms differ from each other by 0.53 Å RMSD. RMSD values were calculated using LSQ in Coot. **B.** The C_α atoms differ from each other by 0.56 Å RMSD. Backbone and side chain rotomers were optimized with Foldit over 2000 iterations to minimize energy to -603 REU. **C.** Aβ 16-22 overlay with tau 304-310 in parallel, backbone atoms differ from each other by 0.54 Å RMSD. RMSD values were calculated using LSQ in Coot.

Table 2. Computed binding properties of designed inhibitors to amyloid-beta $_{16}$KLVFFAEN$_{23}$

Peptide Name	Sequence	MW (g/mol)	Hydropathicity (GRAVY)	Binding Energy (R.E.U.)	SA Buried (Å^2)	Shape Complementarity
L1	KWYFIE	885	-0.38	-4.41	760	0.76
L2	NLYVRE	793	-0.80	-5.02	761	0.73
L3	ERLYHFME	1124	-0.94	-4.69	1016	0.79
L4	QRVYRTWQ	1136	-1.84	-4.75	1026	0.75
LC	LYIWVQ	821	1.13	-4.25	719	0.75
D1	D-LYIWVQ	821	1.13	-4.92	771	0.70
D1a	D-LYIWIQMQ	1094	0.69	-5.33	1149	0.71
D1b	D-LYIWIWRT	1150	0.56	-6.11	1235	0.72
D1c	D-LYIWIWFS	1127	1.46	-5.95	1215	0.71
D1d	D-LYIWIQKT	1064	0.31	-5.25	1140	0.70
D1e	D-MYIWVQ	839	0.82	-4.94	776	0.70
D1f	D-MYIWRQ	896	-0.63	-4.40	802	0.70
D2	D-MLIVRN	745	1.07	-4.17	760	0.70

REFERRENCES

1. Glenner, G. G., Wong, C. W., Quaranta, V., and Eanes, E. D. (1984) The amyloid deposits in Alzheimer's disease: their nature and pathogenesis. *Appl. Pathol.* **2**, 357–369
2. Goedert, M., Eisenberg, D. S., and Crowther, R. A. (2017) Propagation of Tau Aggregates and Neurodegeneration. *Annu. Rev. Neurosci.* **40**, 189–210
3. Tanzi, R. E. (2012) The genetics of Alzheimer disease (7). *Cold Spring Harb. Perspect. Med.* **2**, a006296
4. Hardy, J., and Selkoe, D. J. (2002) The amyloid hypothesis of Alzheimer's disease: progress and problems on the road to therapeutics. *Science*. **297**, 353–356
5. Manczak, M., and Reddy, P. H. (2014) Abnormal interaction of oligomeric amyloid-β with phosphorylated tau: implications to synaptic dysfunction and neuronal damage. *J Alzheimers Dis.* **36**, 285–295
6. Seward, M. E., Swanson, E., Norambuena, A., Reimann, A., Cochran, J. N., Li, R., Roberson, E. D., and Bloom, G. S. (2013) Amyloid- signals through tau to drive ectopic neuronal cell cycle re-entry in Alzheimer's disease. *J. Cell Sci.* **126**, 1278–1286
7. Brier, M. R., Gordon, B., Morris, J. H., Benzinger, T. L. S., and Ances, B. M. (2016) Tau and Aß imaging, CSF measures, and cognition in Alzheimer' s disease. *Sci. Transl. Med.* **8**, 1–10
8. Schwarz, A. J., Yu, P., Miller, B. B., Shcherbinin, S., Dickson, J., Navitsky, M., Joshi, A. D., Devous, M. D., and Mintun, M. S. (2016) Regional profiles of the candidate tau PET ligand18F-AV-1451 recapitulate key features of Braak histopathological stages. *Brain*. **139**, 1539–1550

9. Chen, G., Xu, T., Yan, Y., Zhou, Y., Jiang, Y., Melcher, K., and Xu, H. E. (2017) Amyloid beta : structure , biology and structure-based therapeutic development. *Nat. Publ. Gr.* **38**, 1205–1235

10. Oddo, S., Caccamo, A., Shepherd, J. D., Murphy, M. P., Golde, T. E., Kayed, R., Metherate, R., Mattson, M. P., Akbari, Y., and LaFerla, F. M. (2003) Triple-transgenic model of Alzheimer's Disease with plaques and tangles: Intracellular Aβ and synaptic dysfunction. *Neuron*. **39**, 409–421

11. Bolmont, T., Clavaguera, F., Meyer-Luehmann, M., Herzig, M. C., Radde, R., Staufenbiel, M., Lewis, J., Hutton, M., Tolnay, M., and Jucker, M. (2007) Induction of tau pathology by intracerebral infusion of amyloid-β-containing brain extract and by amyloid-β deposition in APP x tau transgenic mice. *Am. J. Pathol.* **171**, 2012–2020

12. Gotz, J. (2001) Formation of Neurofibrillary Tangles in P301L Tau Transgenic Mice Induced by Abeta 42 Fibrils. *Science (80-.).* **293**, 1491–1495

13. Morales, R., Bravo-Alegria, J., Duran-Aniotz, C., and Soto, C. (2015) Titration of biologically active amyloid-β seeds in a transgenic mouse model of Alzheimer's disease. *Sci. Rep.* **5**, 9349

14. Choi, S. H., Kim, Y. H., Hebisch, M., Sliwinski, C., Lee, S., D'Avanzo, C., Chen, H., Hooli, B., Asselin, C., Muffat, J., Klee, J. B., Zhang, C., Wainger, B. J., Peitz, M., Kovacs, D. M., Woolf, C. J., Wagner, S. L., Tanzi, R. E., and Kim, D. Y. (2014) A three-dimensional human neural cell culture model of Alzheimer's disease. *Nature*. **515**, 274–278

15. Ittner, L. M., and Götz, J. (2011) Amyloid-β and tau - A toxic pas de deux in Alzheimer's disease. *Nat. Rev. Neurosci.* **12**, 67–72

16. Stancu, I. C., Vasconcelos, B., Terwel, D., and Dewachter, I. (2014) Models of β-amyloid induced Tau-pathology: the long and "folded" road to understand the mechanism. *Mol. Neurodegener.* **9**, 51

17. Rajendran, L., Honsho, M., Zahn, T. R., Keller, P., Geiger, K. D., Verkade, P., and Simons, K. (2006) Alzheimer's disease beta-amyloid peptides are released in association with exosomes. *Proc. Natl. Acad. Sci.* **103**, 11172–11177

18. Lesné, S., Ming, T. K., Kotilinek, L., Kayed, R., Glabe, C. G., Yang, A., Gallagher, M., and Ashe, K. H. (2006) A specific amyloid-β protein assembly in the brain impairs memory. *Nature*. **440**, 352–357

19. Lambert, M. P., Barlow, A. K., Chromy, B. A., Edwards, C., Freed, R., Liosatos, M., Morgan, T. E., Rozovsky, I., Trommer, B., Viola, K. L., Wals, P., Zhang, C., Finch, C. E., Krafft, G. A., and Klein, W. L. (1998) Diffusible, nonfibrillar ligands derived from Aβ 1-42 are potent central nervous system neurotoxins. *Proc. Natl. Acad. Sci.* **95**, 6448–6453

20. Benilova, I., Karran, E., and De Strooper, B. (2012) The toxic Aβ oligomer and Alzheimer's disease: an emperor in need of clothes. *Nat. Neurosci.* 10.1038/nn.3028

21. Jin, M., Shepardson, N., Yang, T., Chen, G., Walsh, D., and Selkoe, D. J. (2011) Soluble amyloid -protein dimers isolated from Alzheimer cortex directly induce Tau hyperphosphorylation and neuritic degeneration. *Proc. Natl. Acad. Sci.* **108**, 5819–5824

22. Guo, J.-P., Arai, T., Miklossy, J., and McGeer, P. L. (2006) Abeta and tau form soluble complexes that may promote self aggregation of both into the insoluble forms observed in Alzheimer's disease. *Proc. Natl. Acad. Sci. U. S. A.* **103**, 1953–8

23. Vasconcelos, B., Cosmin, I., Arjan, S., Matthew, B., Wang, P., Vanoosthuyse, A., Kolen, K. Van, Verheyen, A., Kienlen, P., Jean, C., Octave, N., Baatsen, P., and Moechars, D. (2016) Heterotypic seeding of Tau fibrillization by pre - aggregated Abeta provides potent seeds for prion - like seeding and propagation of Tau - pathology in vivo. *Acta Neuropathol.* **131**, 549–569

24. Miller, Y., Ma, B., and Nussinov, R. (2011) Synergistic interactions between repeats in tau protein and Aβ amyloids may be responsible for accelerated aggregation via polymorphic States. *Biochemistry*. **50**, 5172–5181

25. Tjernberg, L. O., Callaway, D. J., Tjernberg, a, Hahne, S., Lilliehöök, C., Terenius, L., Thyberg, J., and Nordstedt, C. (1999) A molecular model of Alzheimer amyloid beta-peptide fibril formation. *J. Biol. Chem.* **274**, 12619–12625

26. Bernstein, S. L., Wyttenbach, T., Baumketner, A., Shea, J. E., Bitan, G., Teplow, D. B., and Bowers, M. T. (2005) Amyloid β-protein: Monomer structure and early aggregation states of Aβ42 and its Pro19alloform. *J. Am. Chem. Soc.* **127**, 2075–2084

27. Marshall, K. E., Vadukul, D. M., Dahal, L., Theisen, A., Fowler, M. W., Al-Hilaly, Y., Ford, L., Kemenes, G., Day, I. J., Staras, K., and Serpell, L. C. (2016) A critical role for the self-assembly of Amyloid-β1-42 in neurodegeneration. *Sci. Rep.* **6**, 1–13

28. Colletier, J.-P., Laganowsky, A., Landau, M., Zhao, M., Soriaga, A. B., Goldschmidt, L., Flot, D., Cascio, D., Sawaya, M. R., and Eisenberg, D. (2011) Molecular basis for amyloid- polymorphism. *Proc. Natl. Acad. Sci.* **108**, 16938–16943

29. Lührs, T., Ritter, C., Adrian, M., Riek-Loher, D., Bohrmann, B., Döbeli, H., Schubert, D., and Riek, R. (2005) 3D structure of Alzheimer's amyloid-beta(1-42) fibrils. *Proc. Natl. Acad. Sci. U. S. A.* **102**, 17342–17347

30. Colvin, M. T., Silvers, R., Ni, Q. Z., Can, T. V., Sergeyev, I., Rosay, M., Donovan, K. J., Michael, B., Wall, J., Linse, S., and Griffin, R. G. (2016) Atomic Resolution Structure of Monomorphic Aβ 42 Amyloid Fibrils. *J. Am. Chem. Soc.* **138**, 9663–9674

31. Qiang, W., Yau, W.-M., Luo, Y., Mattson, M. P., and Tycko, R. (2012) Antiparallel -sheet architecture in Iowa-mutant -amyloid fibrils. *Proc. Natl. Acad. Sci.* **109**, 4443–4448

32. Huber, M., Ovchinnikova, O. Y. u, Schütz, A. K., Glockshuber, R., Meier, B. H., and Böckmann, A. (2015) Solid-state NMR sequential assignment of Osaka-mutant amyloid-beta (Aβ1-40 E22Δ) fibrils. *Biomol. NMR Assign.* **9**, 7–14

33. Wälti, M. A., Ravotti, F., Arai, H., Glabe, C. G., Wall, J. S., Böckmann, A., Güntert, P., Meier, B. H., and Riek, R. (2016) Atomic-resolution structure of a disease-relevant Aβ(1-42) amyloid fibril. *Proc. Natl. Acad. Sci. U. S. A.* **113**, E4976-84

34. Van Nostrand, W. E., Melchor, J. P., Cho, H. S., Greenberg, S. M., and Rebeck, G. W. (2001) Pathogenic Effects of D23N Iowa Mutant Amyloid β-Protein. *J. Biol. Chem.* **276**, 32860–32866

35. Tay, W. M., Huang, D., Rosenberry, T. L., and Paravastu, A. K. (2013) The Alzheimer's amyloid-β(1-42) peptide forms off-pathway oligomers and fibrils that are distinguished structurally by intermolecular organization. *J. Mol. Biol.* **425**, 2494–2508

36. Laganowsky, A., Liu, C., Sawaya, M. R., Whitelegge, J. P., Park, J., Zhao, M., Pensalfini, A., Soriaga, A. B., Landau, M., Teng, P. K., Cascio, D., Glabe, C., and Eisenberg, D. (2012) Atomic view of a toxic amyloid small oligomer. *Science*. **335**, 1228–31

37. Sarkar, B., Mithu, V. S., Chandra, B., Mandal, A., Chandrakesan, M., Bhowmik, D., Madhu, P. K., and Maiti, S. (2014) Significant Structural Differences between

Transient Amyloid-β Oligomers and Less-Toxic Fibrils in Regions Known To Harbor Familial Alzheimer's Mutations. *Angew. Chem. Int. Ed*. 10.1002/anie.201402636

38. Krotee, P., Griner, S. L., Sawaya, M. R., Cascio, D., Rodriguez, J. A., Shi, D., Philipp, S., Murray, K., Saelices, L., Lee, J., Seidler, P., Glabe, C. G., Jiang, L., Gonen, T., and Eisenberg, D. S. (2018) Common fibrillar spines of amyloid-β and human islet amyloid polypeptide revealed by microelectron diffraction and structure-based inhibitors. *J. Biol. Chem.* 10.1074/jbc.M117.806109

39. Colletier, J.-P., Laganowsky, A., Landau, M., Zhao, M., Soriaga, A. B., Goldschmidt, L., Flot, D., Cascio, D., Sawaya, M. R., and Eisenberg, D. (2011) Molecular basis for amyloid-beta polymorphism. *Proc. Natl. Acad. Sci. U. S. A.* **108**, 16938–43

40. Tycko, R., Sciarretta, K. L., Orgel, J. P. R. O., and Meredith, S. C. (2009) Evidence for novel β-sheet structures in Iowa mutant β-amyloid fibrils. *Biochemistry*. **48**, 6072–6084

41. Liu, C., Zhao, M., Jiang, L., Cheng, P.-N., Park, J., Sawaya, M. R., Pensalfini, A., Gou, D., Berk, A. J., Glabe, C. G., Nowick, J., and Eisenberg, D. (2012) Out-of-register β-sheets suggest a pathway to toxic amyloid aggregates. *Proc. Natl. Acad. Sci. U. S. A.* **109**, 20913–8

42. Sun, Y., Ge, X., Xing, Y., Wang, B., and Ding, F. (2018) β-barrel Oligomers as Common Intermediates of Peptides Self-Assembling into Cross-β Aggregates. *Sci. Rep.* **8**, 10353

43. Sievers, S. A., Karanicolas, J., Chang, H. W., Zhao, A., Jiang, L., Zirafi, O., Stevens, J. T., Münch, J., Baker, D., and Eisenberg, D. (2011) Structure-based design of non-natural amino-acid inhibitors of amyloid fibril formation. *Nature*. **475**, 96–100

44. Seidler, P. M., Boyer, D. R., Rodriguez, J. A., Sawaya, M. R., Cascio, D., Murray, K.,

Gonen, T., and Eisenberg, D. S. (2018) Structure-based inhibitors of tau aggregation. *Nat. Chem.* **10**, 170–176

45. Saelices, L., Johnson, L. M., Liang, W. Y., Sawaya, M. R., Cascio, D., Ruchala, P., Whitelegge, J., Jiang, L., Riek, R., and Eisenberg, D. S. (2015) Uncovering the mechanism of aggregation of human transthyretin. *J. Biol. Chem.* **290**, 28932–28943

46. Soragni, A., Janzen, D. M., Johnson, L. M., Lindgren, A. G., Thai-Quynh Nguyen, A., Tiourin, E., Soriaga, A. B., Lu, J., Jiang, L., Faull, K. F., Pellegrini, M., Memarzadeh, S., and Eisenberg, D. S. (2016) A Designed Inhibitor of p53 Aggregation Rescues p53 Tumor Suppression in Ovarian Carcinomas. *Cancer Cell*. **29**, 90–103

47. Krotee, P., Griner, S. L., Sawaya, M. R., Cascio, D., Rodriguez, J. A., Shi, D., Philipp, S., Murray, K., Saelices, L., Lee, J., Seidler, P., Glabe, C. G., Jiang, L., Gonen, T., and Eisenberg, D. S. (2018) Common fibrillar spines of amyloid-β and human islet amyloid polypeptide revealed by microelectron diffraction and structure-based inhibitors. *J. Biol. Chem.* **293**, 2888–2902

48. Olmsted, J. B., Carlson, K., Klebe, R., Ruddle, F., and Rosenbaum, J. (1970) Isolation of microtubule protein from cultured mouse neuroblastoma cells. *Proc. Natl. Acad. Sci. U. S. A.* **65**, 129–136

49. Mosmann, T. (1983) Rapid colorimetric assay for cellular growth and survival: application to proliferation and cytotoxicity assays. *J. Immunol. Methods*. **65**, 55–63

50. Liu, Y., Peterson, D. A., Kimura, H., and Schubert, D. (1997) Mechanism of cellular 3-(4,5-dimethylthiazol-2-yl)-2,5- diphenyltetrazolium bromide (MTT) reduction. *J. Neurochem.* **6**, 581–593

51. Hatami, A., Albay, R., Monjazeb, S., Milton, S., and Glabe, C. (2014) Monoclonal

antibodies against A??42 fibrils distinguish multiple aggregation state polymorphisms in vitro and in Alzheimer disease brain. *J. Biol. Chem.* **289**, 32131–32143

52. Manuscript, A., Iii, G. E., Salvadores, N., Shahnawaz, M., Soto, C., May, A., Responsible, B., Tatarnikova, O. G., Orlov, M. A., Bobkova, N. V, Chen, G., Xu, T., Yan, Y., Zhou, Y., Jiang, Y., Melcher, K., Xu, H. E., Baughman, H. E. R., Clouser, A. F., Klevit, R. E., Nath, A., Vasconcelos, B., Cosmin, I., Arjan, S., Matthew, B., Wang, P., Vanoosthuyse, A., Kolen, K. Van, Verheyen, A., Kienlen, P., Jean, C., Octave, N., Baatsen, P., and Moechars, D. (2017) Heterotypic seeding of Tau fibrillization by pre - aggregated Abeta provides potent seeds for prion - like seeding and propagation of Tau - pathology in vivo. *Acta Neuropathol.* **131**, 1327–1334

53. Kfoury, N., Holmes, B. B., Jiang, H., Holtzman, D. M., and Diamond, M. I. (2012) Trans-cellular propagation of Tau aggregation by fibrillar species. *J. Biol. Chem.* **287**, 19440–19451

54. Sawaya, M. R., Sambashivan, S., Nelson, R., Ivanova, M. I., Sievers, S. A., Apostol, M. I., Thompson, M. J., Balbirnie, M., Wiltzius, J. J. W., McFarlane, H. T., Madsen, A. Ø., Riekel, C., and Eisenberg, D. (2007) Atomic structures of amyloid cross-β spines reveal varied steric zippers. *Nature*. **447**, 453

55. Fitzpatrick, A. W. P., Falcon, B., He, S., Murzin, A. G., Murshudov, G., Garringer, H. J., Crowther, R. A., Ghetti, B., Goedert, M., and Scheres, S. H. W. (2017) Cryo-EM structures of tau filaments from Alzheimer's disease. *Nature*. **547**, 185

56. Falcon, B., Zhang, W., Schweighauser, M., Murzin, A. G., Vidal, R., Garringer, H. J., Ghetti, B., Scheres, S. H. W., and Goedert, M. (2018) Tau filaments from multiple cases

of sporadic and inherited Alzheimer ' s disease adopt a common fold. *Acta Neuropathol.* **136**, 699–708

57. Lazo, N. D., Grant, M. A., Condron, M. C., Rigby, A. C., and Teplow, D. B. (2009) On the nucleation of amyloid β-protein monomer folding. *Protein Sci.* **14**, 1581–1596

58. Krone, M. G., Baumketner, A., Bernstein, S. L., Wyttenbach, T., Lazo, N. D., Teplow, D. B., Bowers, M. T., and Shea, J. (2008) Effects of Familial Alzheimer's Disease Mutations on the Folding Nucleation of the Amyloid β-Protein. *J. Mol. Biol.* **381**, 221–228

59. Chong, S.-H., Yim, J., and Ham, S. (2013) Structural heterogeneity in familial Alzheimer's disease mutants of amyloid-beta peptides. *Mol. BioSyst. Mol. BioSyst*. **9**, 997–1003

60. Kirschner, D. A., Abraham, C., and Selkoe, D. J. (1986) X-ray diffraction from intraneuronal paired helical filaments and extraneuronal amyloid fibers in Alzheimer disease indicates cross-beta conformation. *Proc. Natl. Acad. Sci.* **83**, 503–507

61. Sanders, D. W., Kaufman, S. K., DeVos, S. L., Sharma, A. M., Mirbaha, H., Li, A., Barker, S. J., Foley, A. C., Thorpe, J. R., Serpell, L. C., Miller, T. M., Grinberg, L. T., Seeley, W. W., and Diamond, M. I. (2014) Distinct tau prion strains propagate in cells and mice and define different tauopathies. *Neuron*. **82**, 1271–1288

62. Shi, D., Nannenga, B. L., de la Cruz, M. J., Liu, J., Sawtelle, S., Calero, G., Reyes, F. E., Hattne, J., and Gonen, T. (2016) The collection of MicroED data for macromolecular crystallography. *Nat. Protoc.* **11**, 895–904

63. Hattne, J., Reyes, F. E., Nannenga, B. L., Shi, D., de la Cruz, M. J., Leslie, A. G. W., and Gonen, T. (2015) MicroED data collection and processing. *Acta Crystallogr. Sect. A*

Found. Adv. **71**, 353–360

64. Nannenga, B. L., Shi, D., Leslie, A. G. W., and Gonen, T. (2014) High-resolution structure determination by continuous-rotation data collection in MicroED. *Nat. Methods*. **11**, 1–5

65. Kabsch, W. (2010) XDS. *Acta Crystallogr. D. Biol. Crystallogr.* **66**, 125–32

66. McCoy, A. J. (2007) Solving structures of protein complexes by molecular replacement with Phaser. *Acta Crystallogr. D. Biol. Crystallogr.* **63**, 32–41

67. Emsley, P., and Cowtan, K. (2004) Coot: model-building tools for molecular graphics. *Acta Crystallogr. D. Biol. Crystallogr.* **60**, 2126–32

68. McCoy, A. J., Grosse-Kunstleve, R. W., Storoni, L. C., and Read, R. J. (2005) Likelihood-enhanced fast translation functions. *Acta Crystallogr. D. Biol. Crystallogr.* **61**, 458–64

69. Collaborative Computational Project Number 4 (1994) The CCP4 suite: programs for protein crystallography. *Acta Crystallogr. D. Biol. Crystallogr.* **50**, 760–763

70. Lee, B., and Richards, F. M. (1971) The interpretation of protein structures: Estimation of static accessibility. *J. Mol. Biol.* 10.1016/0022-2836(71)90324-X

71. Connolly, M. L. (1983) Solvent-accessible surfaces of proteins and nucleic acids. *Science*. **221**, 709–13

72. Lawrence, M. C., and Colman, P. M. (1993) Shape complementarity at protein-protein interfaces. *J. Mol. Biol.* **93**, 946–950

73. Richards, F. M. (1977) Areas, volumes, packing, and protein structure. *Annu. Rev. Biophys. Bioeng.* **5**, 151–176

74. Sievers, S. A., Karanicolas, J., Chang, H. W., Zhao, A., Jiang, L., Zirafi, O., Stevens, J. T., Münch, J., Baker, D., and Eisenberg, D. (2011) Structure-based design of non-natural

amino-acid inhibitors of amyloid fibril formation. *Nature*. **475**, 96–100

75. Kyte, J., and Doolittle, R. F. (1982) A simple method for displaying the hydropathic character of a protein. *J. Mol. Biol.* **157**, 105–132

76. Krotee, P., Rodriguez, J. A., Sawaya, M. R., Cascio, D., Reyes, F. E., Shi, D., Hattne, J., Nannenga, B. L., Oskarsson, M. E., Philipp, S., Griner, S., Jiang, L., Glabe, C. G., Westermark, G. T., Gonen, T., and Eisenberg, D. S. (2017) Atomic structures of fibrillar segments of hIAPP suggest tightly mated β-sheets are important for cytotoxicity. *Elife*. 10.7554/eLife.19273

77. Eliceiri, K., Schneider, C. A., Rasband, W. S., and Eliceiri, K. W. (2012) NIH Image to ImageJ : 25 years of image analysis HISTORICAL commentary NIH Image to ImageJ : 25 years of image analysis. *Nat. Methods*. **9**, 671–675

78. Emsley, P., and Cowtan, K. (2004) Coot: model-building tools for molecular graphics. *Acta Crystallogr. D. Biol. Crystallogr.* **60**, 2126–32

79. Kleffner, R., Cooper, S., Khatib, F., Flatten, J., Leaver-Fay, A., Baker, D., and Siegel, J. B. (2017) Foldit Standalone: a video game-derived protein structure manipulation interface using Rosetta. *Bioinformatics*. **33**, 2765–2767

Chapter Two

Common Fibrillar Spines of Amyloid-β and human Islet Amyloid Polypeptide Revealed by Micro Electron Diffraction and Inhibitors Developed Using Structure-Based Design

ABSTRACT

Amyloid-β (Aβ) and human islet amyloid polypeptide (hIAPP) aggregate to form amyloid fibrils that deposit in tissues, and are associated with Alzheimer's disease (AD) and Type-II Diabetes (T2D), respectively. Individuals with T2D have an increased risk of developing AD, and conversely, AD patients have an increased risk of developing T2D. Evidence suggests that this link between AD and T2D might originate from a structural similarity between aggregates of Aβ and hIAPP. Using the cryoEM method Micro-Electron Diffraction (MicroED) we determined the atomic structures of 11-residue segments from both Aβ and hIAPP, termed Aβ 24-34 WT and hIAPP 19–29 S20G, with 64% sequence similarity. We observe a high degree of structural similarity between their backbone atoms (0.96 Å RMSD). Moreover, fibrils of these segments induce amyloid formation through self- and cross-seeding. Furthermore, inhibitors designed for one segment show cross-efficacy for full-length Aβ and hIAPP and reduce cytotoxicity of both proteins, though by apparently blocking different cytotoxic mechanisms. The similarity of the atomic structures of Aβ 24-34 WT and hIAPP 19–29 S20G offers a molecular model for cross-seeding between Aβ and hIAPP.

INTRODUCTION

Amyloid fibrils are protein aggregates associated with pathogenesis in a variety of incurable, and largely untreatable, diseases. These fibrils all appear morphologically similar and share β-sheet rich structures, which stack along the fibril axis. Such fibrils give a cross-β diffraction pattern when they are aligned and analyzed in a X-ray or electron beam (1–3). Two of the most prevalent of these amyloid diseases are Alzheimer's disease

(AD) and Type-II diabetes (T2D). In AD, extracellular amyloid fibrils that form senile plaques are composed of amyloid-β (Aβ), a peptide of 39-42 amino acids. In T2D, amyloid fibrils are composed of human islet amyloid polypeptide (hIAPP), a 37 amino acid peptide hormone (4, 5).

Although as far as is known, each fibril is composed of a single protein, the deposits can contain fibrils of more than one protein, which has led to the hypothesis that amyloid proteins may make cross-sequence interactions as well as self-assemble (6). For example, in AD, Aβ has been reported to form soluble complexes with tau (7), as well as co-deposit with alpha-synuclein (8) and transthyretin (9), whereas hIAPP aggregation is inhibited by binding to insulin (10, 11). Recently, hIAPP has been found to co-deposit with Aβ in senile plaques in AD patient-derived samples (12).

The co-deposition of Aβ and hIAPP might arise from cross-seeding events, where fibrils of one sequence lower the energy barrier to fibrilization of the other sequence. The molecular mechanism of cross-seeding is unknown, but likely depends on structural similarity between aggregates of the two proteins. In the native state, both proteins are unfolded, but contain hydrophobic regions which are highly aggregation prone. Their sequences are 50% similar and 25% identical (Figure 1A), with sequence segments important for self-aggregation displaying the greatest similarity (13). Protein segments of hIAPP and Aβ with the highest similarity bind to one another with high affinity (14, 15) and appear to catalyze hetero-assembly. Aβ and hIAPP appear to interact not only in their native unfolded states, but also can interact once aggregated. Aβ fibrils cross-seed hIAPP fibril formation, suggesting the 3D fibril structure of Aβ is able to template hIAPP aggregation, possibly by conferring a similar structural motif (16). Supporting the idea that

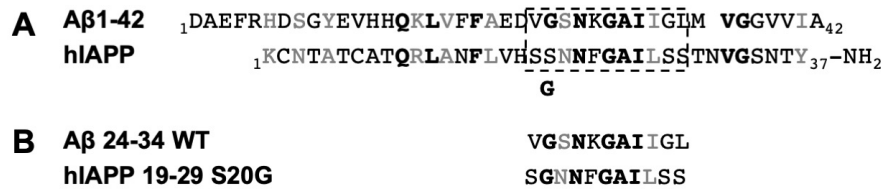


Figure 1. Sequence alignment of amyloid-β1-42 (Aβ1-42) and hIAPP. Identical residues are highlighted in bold font and similar residues are highlighted in gray. **A.** Alignment of Aβ1-42 and hIAPP sequences reveals that hIAPP is 51% similar and 27% identical to Aβ1-42. The early onset Type-II Diabetes mutation in hIAPP, S20G, is shown below the hIAPP sequence. The amyloid spines of Aβ1-42 and hIAPP are boxed with dotted lines. hIAPP-S20G was used to calculate sequence similarity to Aβ1-42. **B.** Alignment of the spine segments Aβ 24-34 WT and hIAPP 19-29 S20G reveals that they are 64% similar are 45% identical.

the underlying structures of the fibrils are similar, a recent study describes a peptide-based fibril blocker that mitigates fibril formation and cytotoxicity of both Aβ and hIAPP (17).

Cross-seeding is further evident in *in vivo* studies. One study showed that islet amyloid formed in hIAPP transgenic mice upon injection with fibril seeds of either Aβ or hIAPP (12). Moreover, a recent study observed a similar cross-seeding effect when Aβ transgenic mice were injected with hIAPP seeds (18). Beyond model systems, clinical studies have reported increased risk for AD in T2D patients and vice versa (19–21). Some studies suggest AD and T2D are connected by heightened stress and cholesterol levels, while others propose that cross-amyloid interactions, or cross-seeding, connect the diseases (22). This has led some to hypothesize that drugs used to treat T2D may be effective treatments for AD (23).

In an effort to uncover a molecular basis for interaction of Aβ with hIAPP, we focus on two 11-residue, fibril-forming protein segments with 64% sequence identity; we call these segments Aβ 24-34 WT and hIAPP 19-29 S20G, which harbors a familial mutation implicated in early onset T2D (Figure 1B) (24–26). In addition to high identity, these

sequences appear to be important for aggregation and accompanying toxicity of their respective full-length proteins. The Aβ 24-34 WT segment is integral to the core in structures of full length Aβ fibrils as determined from solid state NMR (27–30). Additionally, short peptides spanning from residues 27-32 and 29-34 of Aβ crystallize in steric zipper arrangements (31). Aβ 24-34 WT contains residues necessary for oligomerization and formation of toxic species (32–34). Previously, we demonstrated that fibrils formed from the hIAPP 19-29 S20G segment are structurally related to that of full-length hIAPP and comprise the spine of the mature fibrils (35). Thus Aβ 24-34 WT and hIAPP 19-29 S20G are candidates for self and cross-interacting segments of their two parent proteins.

RESULTS

Atomic structure of Aβ 24-34 WT determined using MicroED- Aβ 24-34 WT crystallized as nanocrystals only a few hundred nanometers thick (Figure 2A), similar to the 11-residue segments of previously determined amyloid structures (3, 35). This crystal size is ideal for Micro-Electron Diffraction (MicroED), a diffraction mode of cryoEM (36–39).

The structure of Aβ 24-34 WT reveals a class I steric-zipper, with pairs of parallel in-register β-sheets anti-parallel to each other (Figure 2B, Table 1). The side-chains interdigitate to form two dry interfaces (Figure 9). Interface A buries 210 $Å^2$ of solvent-accessible surface area (SASA) per strand with a shape complementarity (Sc) of 0.62, with Ala30, Ile32 and Leu34 lining the zipper interface. Additionally, this interface is capped by hydrogen bonding of Lys28 to the carboxy-terminus of the opposing sheet. Interface B is

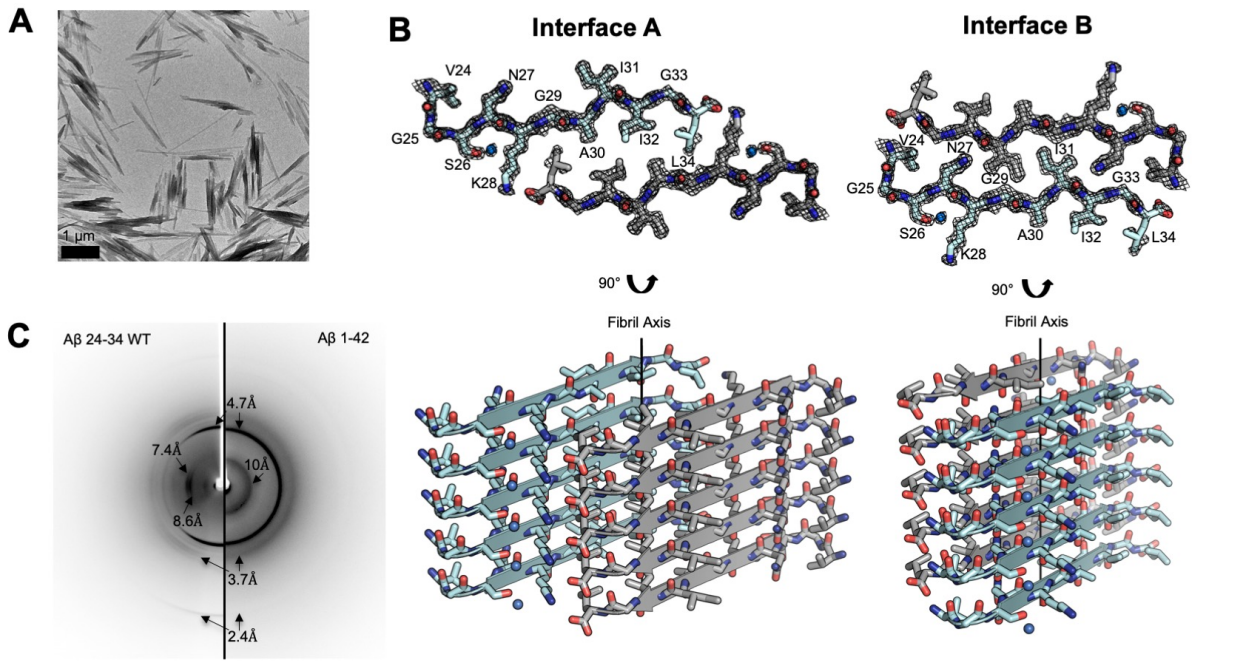


Figure 2. MicroED structure of segment Aβ 24–34 WT from microcrystals. **A**. Electron micrograph of 3D crystals used for data collection. **B**. The crystal structure reveals tightly mated pairs of β-sheets. The side-chains interdigitate to form two extensive dry interfaces, termed Interface A and Interface B. Above: 1 layer viewed down the fibril axes with the $2F_0$-F_c electron density at 1σ displayed as black mesh. Below: 6 layers viewed nearly perpendicular to the fibril axis. The β-sheets are related by a 2_1 axis parallel to the fibril axis**. C**. Comparison of the fibril diffraction of aligned Aβ 24-34 WT microcrystals and Aβ 1-42. Both display a strong reflection at a spacing of 4.7 Å and a weaker reflection at 2.4 Å. Additionally, the two have a broad reflection around 3.7 Å. Aβ 24-34 WT has two distinct reflections at 8.6 Å and 7.4 Å, reflecting the separation of β-sheets in each interface, while Aβ1-42 has a broad reflection around 10 Å.

somewhat larger; it buries 256 $Å^2$ of SASA and has a Sc of 0.85, with Asn27, Gly29 and Ile31 lining the center of the interface. Flanking this interface, Val24 packs into the space provided by the lack of side-chain at Gly33, and salt bridges form between terminal amine and carboxylates from opposing sheets as previously seen in the NACore of alpha-synuclein (3). These later two interactions are introduced by a kink at Gly25.

We see similarities in the fibril diffraction patterns of Aβ1-42 and our crystallized segment. Both display meridional reflections at spacings of 4.7 Å and 2.4 Å, indicative of the

Table 1. Statistics of MicroED data collection and atomic refinement.

	VGSNKGAIIGL
Excitation Voltage (kV)	200
Electron Source	field emission gun
Wavelength (Å)	0.0251
Total dose per crystal (e^-/ Å^2)	2.7
Frame rate (frame/s)	0.3-0.5
Rotation rate (°/s)	0.3
#crystals used	5
Total angular rotation collected (°)	383
Merging Statistics	
Space group	$P2_1$
Cell dimensions	
a, *b*, *c* (Å)	18.78, 4.73, 33.47
α, β, γ (°)	90, 100.02, 90
Resolution (Å)	20-1.5 (1.58-1.50)*
R_{merge}	22.0% (30.6%)
No. Reflections	5586 (555)
Unique Reflections	1032 (133)
Completeness (%)	91.8%(76.4%)
Multiplicity	5.4 (4.2)
I/σ	5.19 (3.11)
$CC_{1/2}$	98.7% (90.8%)
Refinement Statistics	
No. reflections	1031
Reflections in test set	103
R_{work}	22.7%
R_{free}	29.5%
R.m.s. deviations	
Bond lengths (Å)	0.015
Bond angles (°)	1.879
Avg. B factor (Å^2)	
Protein	11.56
Water	14.60
Wilson B factor (Å^2)	7.24
Ramachandran (%)	
Favored	88.9
Allowed	11.1
Outliers	0

*Highest resolution shell shown in parenthesis.

strand-strand spacing within β-sheets, and a set of reflections around 3.7 Å (Figure 2C). The diffraction pattern of Aβ 24-34 WT has two strong equatorial reflections at 8.6 Å and 7.4 Å, which match the average separations of the β-sheets in Interfaces A and B, respectively. The closest corresponding reflections in the Aβ1-42 diffraction pattern are centered around 10 Å, which matches more closely with Interface A rather than B. We hypothesize that Interface A contributes to the strength and spacing of this reflection and therefore is part of the spine of Aβ1-42 fibrils.

Segment Aβ 24-34 WT is cytotoxic- Full-length Aβ is known to be cytotoxic (40), and we wondered whether the segment Aβ 24-34 WT could be the source of this cytotoxicity. To investigate the cytotoxicity of Aβ 24-34 WT, we assessed the effects of the soluble and fibrillar forms of the protein segment on Neuro-2a (N2a) cells, a mouse neuroblastoma cell line (41). We measured cytotoxicity using 3-(4,5-dimethylthiazol-2-yl)-2,5-diphenyltetrazolium bromide (MTT) dye reduction (42, 43) and we measured pro-apoptotic caspase activation using a fluorescent marker for caspase activity.

MTT dye reduction assays revealed that soluble Aβ 24-34 WT is mildly cytotoxic at high concentrations, but its fibrillar form is significantly more cytotoxic (Figure 3A). Aβ 24-34 WT is not as cytotoxic as full-length Aβ 1-42, possibly because Aβ 24-34 WT lacks other residues that are important for cytotoxicity, particularly Met35, which is an important contributor to the potent cytotoxicity of Aβ 25-35 (44, 45). Additionally, we observe that fibrillar Aβ 24-34 WT activates pro-apoptotic caspases, but to a lesser degree than full-length Aβ 1-42 at similar concentrations (Figure 3B, Figure 10). Fibrils of the toxic spine

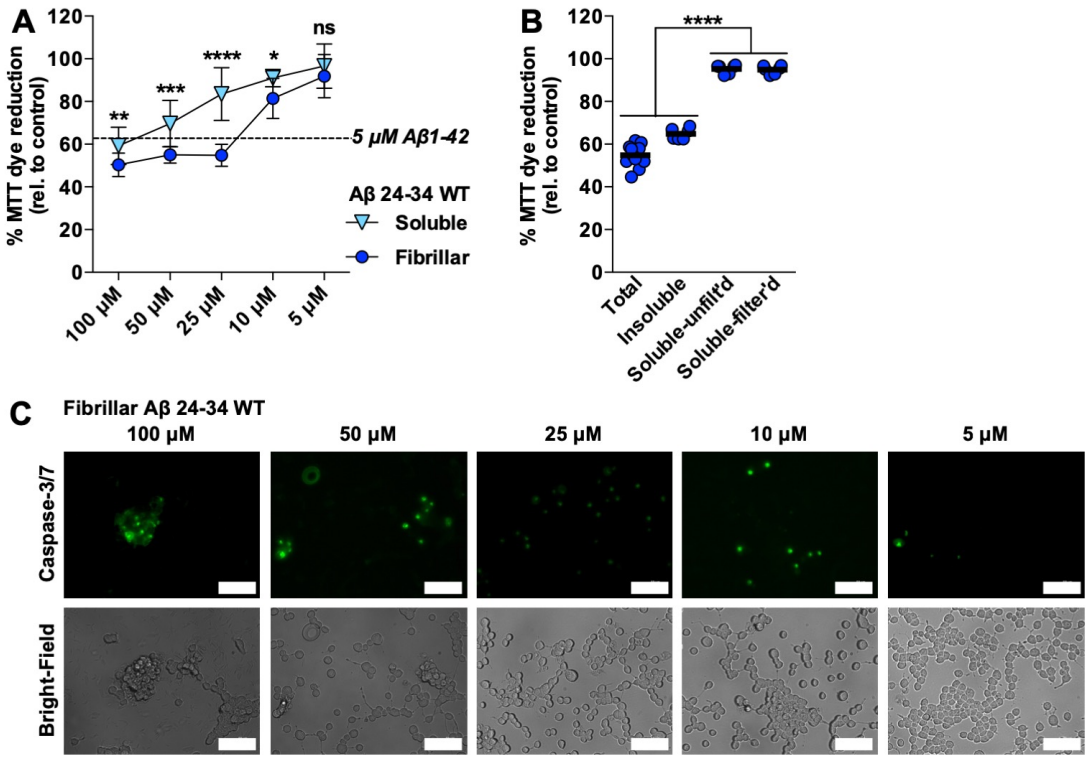


Figure 3. Aβ 24-34 WT is cytotoxic to N2a cells, a mouse neuroblastoma cell line. **A.** The cytotoxicity of Aβ 24-34 WT mainly resides in its fibrillar form, but its soluble form is also mildly cytotoxic. Samples were diluted to 10x from 1 mM stocks and then further diluted 1:10 in media containing pre-plated cells to the concentration specified. Concentrations represent monomer equivalents for both preparations. **B.** The insoluble fraction of the 25 μM fibrillar sample, which contains fibrils, is cytotoxic, further confirming that fibrils or some type of oligomer that tightly associates with fibrils is the cytotoxic species. The insoluble fraction was isolated by centrifuging the fibrillar sample for 1 h using a tabletop centrifuge, and then aspirating off the soluble fraction. Then, the insoluble fraction was resuspended in fresh buffer at its original volume. The 'soluble-filtered' fraction was filtered with a 0.1 μm spin filter while the 'soluble-unfiltered' fraction was not. For **A** and **B**, cytotoxicity was quantified using MTT dye reduction. Points and bars show mean with individual technical replicates (n = 6-12; ns = not significant; *, $p < 0.05$; **, $p < 0.01$; ***, $p < 0.001$; ****, $p < 0.0001$ using a unpaired t-test with equal standard deviations. A is relative to vehicle, in B relative as indicated). **C.** The fibrillar form of Aβ 24-34 WT is associated with increased pro-apoptotic caspase-3/7 activation. Cells were treated as described in section A, and then caspase-3/7 activity was visualized using a fluorescence-based probe for caspase activity. Cells were imaged using a Zeiss fluorescent microscope. Scale bars are 50 microns.

from hIAPP, hIAPP 19-29 S20G, are slightly more cytotoxic than Aβ 24-34 WT to the same cell line (Figure 10).

The insoluble fraction of the Aβ 24-34 WT fibrillar sample is cytotoxic, while the soluble fractions are not, thus suggesting that fibrils are the cytotoxic species (Figure 3B). However, it is plausible that some undetectable population of highly toxic oligomers that associate with fibrils causes the cytotoxicity of the fibrillar sample.

The spines of Aβ and hIAPP are structurally similar- The similarity in sequence between segments Aβ 24-34 WT and hIAPP 19-29 S20G motivated us to compare their atomic structures. We had previously applied MicroED to determine the atomic structure of hIAPP 19-29 S20G (35), a spine segment of hIAPP 64% similar in sequence with Aβ 24-34 WT (Figure 1B).

For both segments, the crystal reveals two sheet-to-sheet interfaces termed Interface A and Interface B, described previously for the structure of Aβ 24-34 WT (Figure 4A). In the crystal structure of hIAPP 19-29 S20G, interface A is lined by Asn21, Phe23, Ala25 and Leu27, while residues Asn22, Gly24, Ile26, and Ser28 line interface B. Interface A of hIAPP 19-29 S20G is likely the primary interface because it excludes waters and fibril diffraction calculated from this interface best matches diffraction collected from full-length hIAPP fibrils. Its Interface B contains waters and has lower shape complementarity. The primary interface of Aβ 24-34 WT is less clear; both its A and B interfaces are dry and large. Either could exist in Aβ 1-42; while interface B appears somewhat stronger, interface A is closer to observed diffraction of the full-length fibers.

Our structures reveal a similarity that is not accurately reflected by their sequence similarity. We observe that the two interface As are more structurally similar to each other than the two interface Bs. Superimposing Aβ 24-34 WT onto hIAPP 19-29 S20G using LSQKAB, we find that backbone atoms of the A interfaces superimpose with 0.96 Å RMSD (Figure 4A), and the backbones of the B interfaces superimpose with a higher RMSD of 2.11 Å. Surprisingly, the structural alignment with lower RMSD (interfaces A) has fewer sequence equivalences than structural alignment with higher RMSD (interfaces B). That is, residues expected to align by sequence identity are shifted by two residues in the structural alignment of interfaces A (Figure 4B). Whereas Ala30 in Aβ 24-34 WT would be expected to align with Ala25 in hIAPP 19-29 S20G, the structural alignment instead superimposes these alanines with Phe23 in hIAPP and Ile32 in Aβ, respectively. Moreover, the leucines in the cores of each of the two interfaces, which are not paired in the sequence alignment, almost perfectly superimpose. This startling result makes one wonder how often sequence alignments do not accurately reflect structural alignments.

Additionally, the mated sheets in each of the two atomic structures differ in the number of residues that stabilize Interface A. Ten of the 11 residues of hIAPP 19-29 S20G form interface A, while the same interface of the Aβ 24-34 WT structure is composed of only 6 of the 11 residues (Figure 4B). The main reason for the reduced overlap between sheets in the Aβ 24-34 WT atomic structure is that the symmetry axes between sheets lies further from the center of the peptide than in the hIAPP segment structure. The length of this offset is supported by Lys28, which hydrogen bonds to the carboxy terminus of its adjacent strand in the mated sheet.

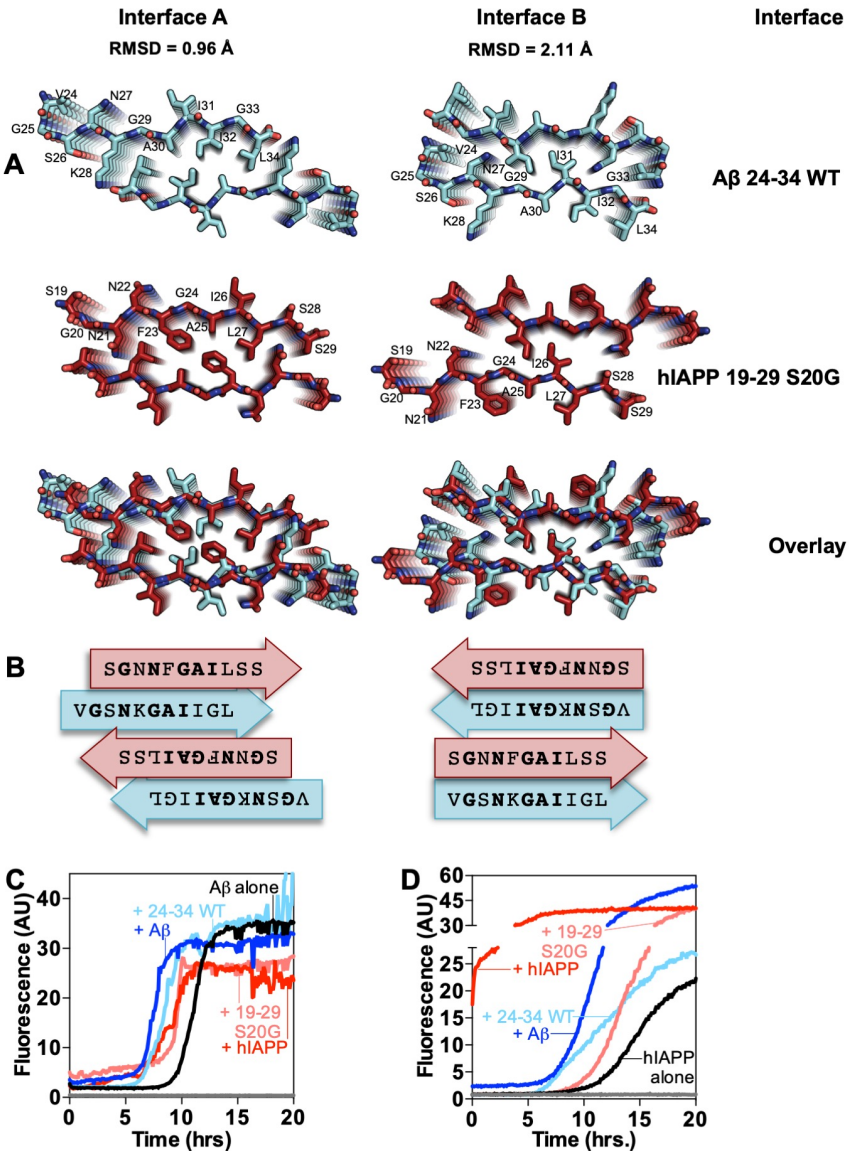
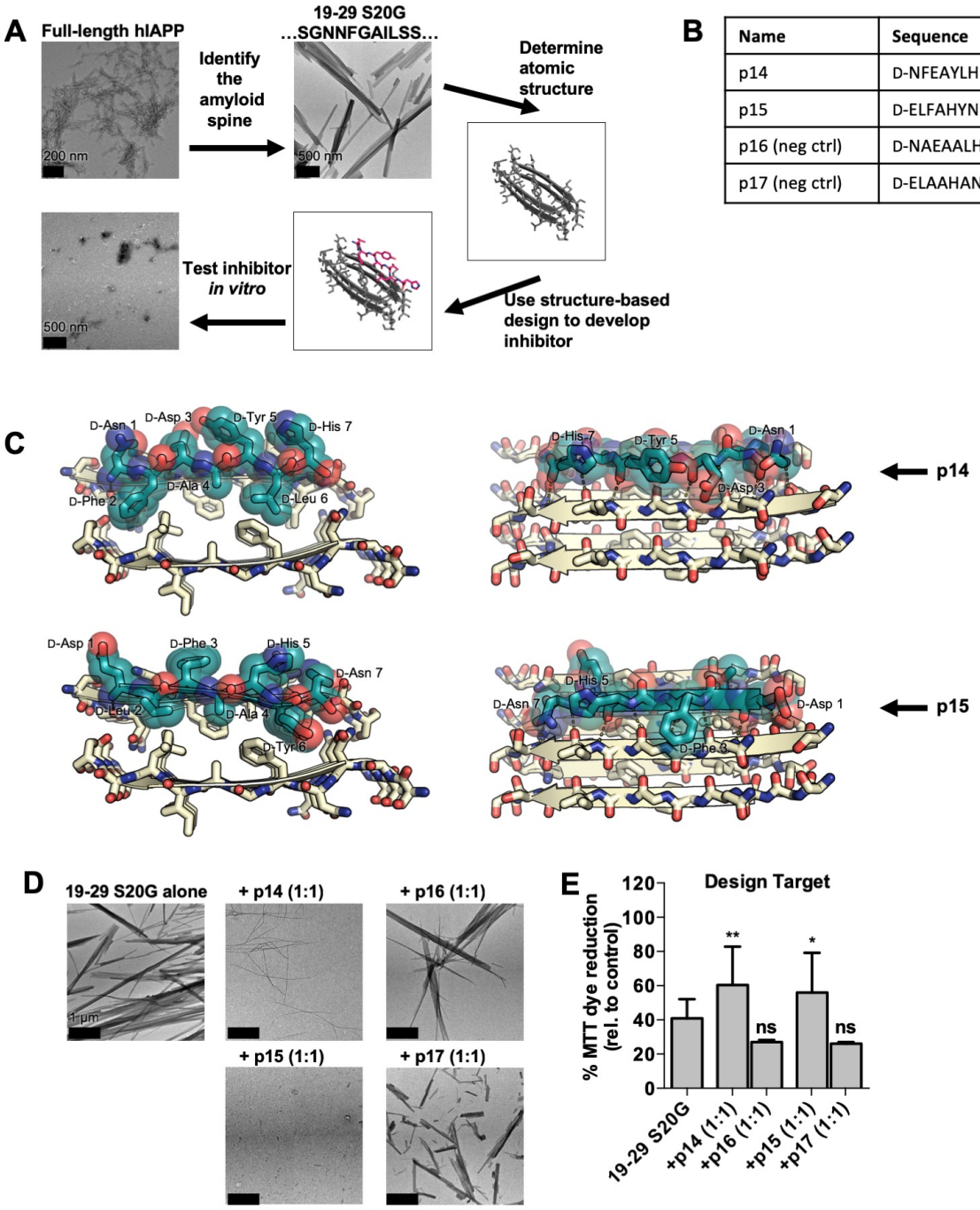


Figure 4. The spines of Aβ 24-34 WT and hIAPP 19-29 S20G are structurally similar. **A.** The crystal packing reveals two interfaces: Interface A and Interface B. The backbone atoms of Interface A (left) differ from each other by 0.96 Å RMSD, whereas the backbones of Interface B (right) differ from each other by 2.11 Å. RMSD values were calculated using LSQKAB. **B.** Schematic of how superpositions of atomic structures reveal that mated sheets composing Interface A are shifted by two residues and display different degrees of overlap. **C.** Seeds of Aβ 24-34 WT and hIAPP 19-29 S20G seed full-length Aβ 1-42 fibril formation near to the efficiency of their parent full-length proteins, suggesting the segments have similar structures to full-length Aβ 1-42 fibrils. **D.** Seeds of Aβ 1-42, Aβ 24-34 WT and hIAPP 19-29 S20G seed full-length hIAPP fibril formation at similar efficacies, while hIAPP 1-37 seeds initiate fibrillization immediately. For **C** and **D**, 10 μM Aβ 1-42 or hIAPP was seeded with 10% (v/v) monomer equivalent of pre-formed seed of each protein or protein segment. Fluorescence of buffer alone is show in gray. Lines show average of three technical replicates with one standard deviation.

As these atomic structures form the spines of their parent full-length proteins and are so similar, we hypothesized that they could facilitate cross-seeding of amyloid fibril formation. In fact, both Aβ 24-34 WT and hIAPP 19-29 S20G fibrils seed full-length Aβ 1-42 fibril formation near to the efficiency of their cognate full-length protein, as seen by thioflavin-T (ThT) fluorescence (Figure 4C, Figure 11A,C). Likewise, both Aβ 24-34 WT and hIAPP 19-29 S20G fibrils seed full-length hIAPP at similar efficiencies as fibrillar Aβ1-42, while addition full-length hIAPP seeds is so efficient that initiation of fibrillization occurs immediately (Figure 4D, Figure 11B,D). These results suggest that perhaps peptide-based inhibitors of fibril formation, developed for hIAPP using the 19-29 S0G atomic structure, may likewise target Aβ.

Development of inhibitors using structure-based design against hIAPP 19-29 S20G- We sought to develop structure-based peptide inhibitors of hIAPP fibril formation using the Interface A of hIAPP 19-29 S20G atomic structure as a scaffold. We used a Rosetta-based design strategy and workflow similar to Sievers, et al. (Figure 5A). Our laboratory has used similar strategies to develop peptide-based inhibitors that reduce fibril formation of amyloid proteins tau, p53, and transthyretin, which are implicated in tauopathies, various cancers, and familial amyloid polyneuropathy, respectively (46–48). We performed multiple rounds of design that produced approximately 50 peptide sequences, about a dozen of which were effective at reducing hIAPP 19-29 S20G fibril formation and cytotoxicity (Table 2; Figures 12 and 13).



Name	Sequence
p14	D-NFEAYLH
p15	D-ELFAHYN
p16 (neg ctrl)	D-NAEAALH
p17 (neg ctrl)	D-ELAAHAN

Figure 5. Development of inhibitors using structure-based design against hIAPP 19-29 S20G. **A.** Schematic of structure-based design process using RosettaDesign (47). Segment hIAPP 19-29 S20G, which forms the toxic spine of hIAPP, was used as the design target. **B.** Overview of peptide inhibitors used in this study and their sequences. Peptides p16 and p17 are the negative controls for peptide inhibitors p14 and p15, respectively. **C.** Models of peptide inhibitors p14 and p15 (dark teal) bound to the design target, hIAPP 19-29 S20G (ivory). The side-chains of the peptide inhibitors form hydrophobic interactions with the

core of hIAPP 19-29 S20G. Additionally, the peptide inhibitors form hydrogen bonds along the peptide backbone (left panel). **D.** Designed peptide inhibitors, p14 and p15, reduce fibril formation of the design target, hIAPP 19-29 S20G, but negative control peptides do not. 1 mM hIAPP 19-29 S20G was incubated with equimolar concentrations of each inhibitor overnight under quiescent conditions. Fibril abundance was evaluated using TEM. Images were captured at 3,200x. Scale bars are 1μm. **E.** Peptide inhibitors reduce cytotoxicity of the design target, hIAPP 19-29 S20G, but negative control peptides do not. Samples were prepared as described in panel **D** and then applied to HEK293 cells at 10 μM final concentration for 24 hours. Cytotoxicity was quantified using MTT dye reduction. Columns show mean with individual technical replicates (n = 3-6; ns = not significant; **, p = 0.0014; *, p = 0.0118 using an ordinary one-way ANOVA relative to leftmost cloumn).

We chose to focus on two all D-conformation peptide sequences because of their potential for longer *in vivo* stability (49), which may be important during downstream clinical testing (Figure 5B, 5C). These designs, abbreviated p14 and p15, reduce fibril formation of the design target, hIAPP 19-29 S20G (Figure 5D) at equimolar concentrations, while their cognate negative control sequences do not. Consistent with previous findings, reducing fibril formation likewise reduces the cytotoxicity of hIAPP 19-29 S20G to HEK293 cells (Figure 5E).

The peptide-based fibril blockers are specific for the design target; they do not reduce aggregation of three other amyloid proteins, transthyretin, tau, and α-synuclein (Figure 14).

Cross-amyloid efficiency of inhibitors- Given the structural and sequence similarity between the two atomic structures and their ability to cross-seed, we aimed to determine whether the inhibitors, developed using the hIAPP 19-29 S20G atomic structure, are effective against both full-length hIAPP and full-length Aβ.

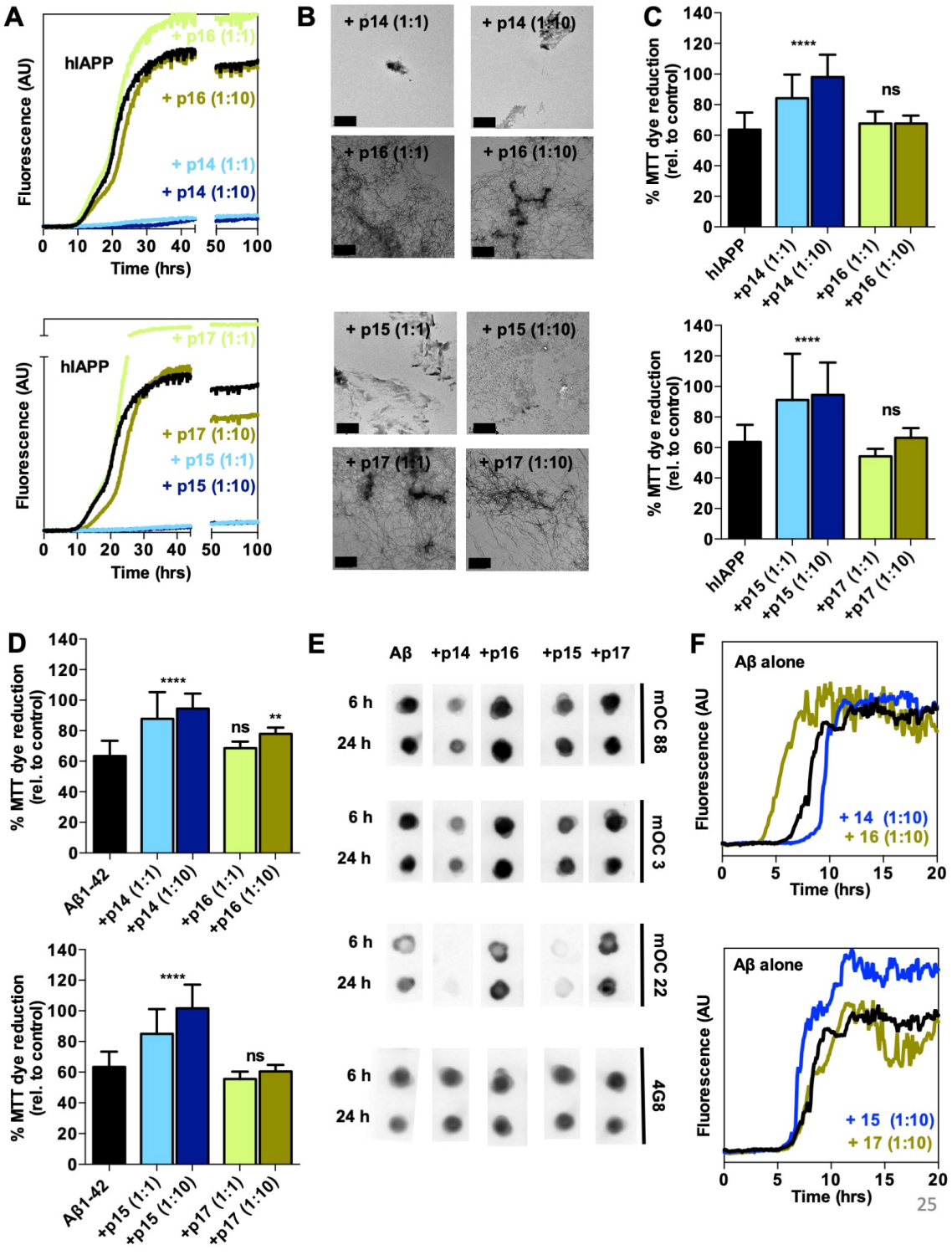


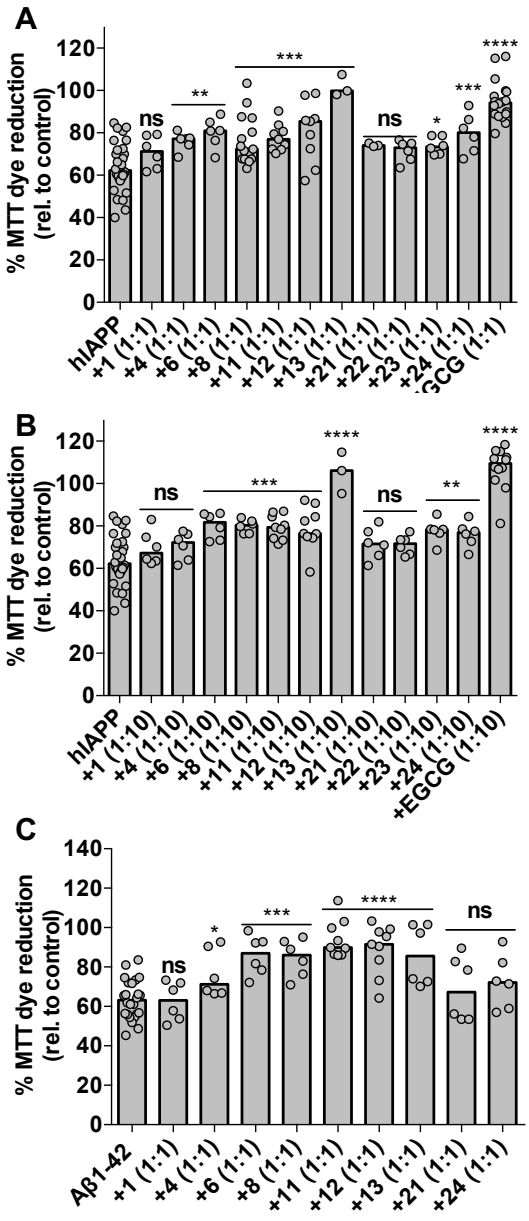
Figure 6. Cross-amyloid efficacy of inhibitors developed with structure-based design against hIAPP 19-29 S20G. **A.** Peptide inhibitors p14 and p15 reduce fibril formation of full-length hIAPP, while negative control peptides p16 and p17 do not. 10 μM hIAPP was

incubated with 1:1 or 1:10 molar ratio of each inhibitor under quiescent conditions. Fibril formation was monitored using Thioflavin-T (ThT) fluorescence. Lines show the average of three technical replicates. **B.** Negative-stain TEM analysis confirms the results of the ThT assays in Figure 6A. 45 hours into the ThT assay, the experiment was paused and samples were extracted for TEM analysis. After samples were extracted, the assay was resumed for 3 more days. **C.** Peptide inhibitors reduce cytotoxicity of full-length hIAPP. 10 μM hIAPP was incubated alone or with the designated concentration of peptide inhibitor overnight under quiescent conditions and then diluted 1:10 with pre-plated Rin5F cells, a rat pancreatic β-cell line. Cytotoxicity was quantified using MTT dye reduction. Bars show mean with individual technical replicates (n = 3-9; ns = not significant; ****, $p < 0.0001$ using an ordinary one-way ANOVA relative to leftmost column). **D.** Peptide inhibitors reduce the cytotoxicity of Aβ1-42, while negative control peptides do not. 10 μM Aβ1-42 was incubated alone or with 1:1 or 1:10 molar ratio of each peptide for 6 hours and then diluted 1:10 with pre-plated N2a cells. Cytotoxicity was quantified using MTT dye reduction. Bars represent mean with individual technical replicates (n = 3-9; ns = not significant; ****, $p < 0.0001$ using an ordinary one-way ANOVA relative to leftmost column). **E.** Peptide inhibitors reduce the formation of Aβ1-42 assemblies recognized by conformational monoclonal antibodies, while negative control peptides do not. 10 μM Aβ1-42 was incubated alone (left-most column) or with 10-fold molar excess of each peptide-based inhibitor. Aliquots of the reaction were tested for antibody-binding at 6 h and 24 h. Binding to 4G8, a monoclonal antibody specific for residues 17-24 in the linearized Aβ sequence, was used to confirm equal loading of sample onto membranes. Membranes were spliced as indicated for clarity. **F.** Peptide inhibitors do not reduce Aβ1-42 fibril formation as assessed with ThT fluorescence.

Using ThT fluorescence, we observe that p14 and p15 reduce fibril formation of full-length hIAPP, but their cognate negative control peptides (p16 and p17, respectively) do not (Figure 6A). 48 hours into the ThT fluorescence assay in Figure 6A, the experiment was paused and aliquots were taken for negative-stain TEM. Negative-stain TEM analysis confirmed the reduction of fibrils in hIAPP samples incubated with p14 and p15. Instead, these samples contained small fibrillar aggregates and amorphous aggregates (Figure 6B). As expected, hIAPP samples incubated with negative control peptides contained abundant fibrils. Consistent with our observation of reduced fibrils, we observe that p14 and p15 reduce cytotoxicity of full-length hIAPP, but their cognate negative control peptides do not (Figure 6C). We tested the cytotoxicity of the samples to Rin5F cells, a rat pancreatic β-cell

line, and we quantified cytotoxicity using MTT dye reduction. Next, we tested whether the same inhibitors, designed against hIAPP 19-29 S20G, reduce fibril formation and cytotoxicity of full-length Aβ 1-42. We observe that p14 and p15 reduce cytotoxicity of Aβ 1-42 to N2a cells (Figure 6D), but neither p14 nor p15 appear to reduce Aβ 1-42 fibril formation (Figure 6F.). To investigate whether the peptide inhibitors reduce the formation of some other cytotoxic Aβ 1-42 assemblies, we probed samples with 31 different conformational antibodies. Three monoclonal antibodies, mOC 88, mOC 3, and mOC 22 showed markedly reduced binding to Aβ 1-42 incubated with either p14 or p15 (Figure 6E, Figure 15). We observed no reduction in binding to Aβ 1-42 incubated with negative control peptides. Although not much is known about the conformations of Aβ that these antibodies recognize, one previous study showed that mOC 3 and mOC 22 bind to Aβ plaques in AD patient-derived brain tissue and also bind to hIAPP fibrils formed *in vitro* (50).

In our identification of effective inhibitors, we screened eleven other peptides to test reduction of the cytotoxicity of full-length hIAPP to Rin5F cells. (Figure 7A, B). Interestingly, all but one of the peptide inhibitors effective against hIAPP also reduced toxicity of Aβ 1-42 on N2a cells (Figure 7C,D). These seven inhibitors encompass a range of sequences and chemical properties (Figure 7C, Table 2), so we postulate that shape complementarity to the target interface is the primary factor involved in blocking hIAPP or Aβ toxic assembly.



E

Peptide Name	Sequence	hIAPP	Aβ1-42
p1	NFKmAImLH	X	X
p4	NFWAKLN	✔	✔
p6	TFYATLH	✔	✔
p8	NLGPVLP	✔	X/✔
p11	AcNFEAYLHS-NH_2	✔	✔
p12	AcTFYAELYS-NH_2	✔	✔
p13	AcHFNELYNS-NH_2	✔	✔
p14	**D-NFEAYLH**	✔	✔
p15	**D-ELFAHYN**	✔	✔
p21	NNFYAELYSS	X	X
p22	AcNNFYAELYSS-NH_2	X	-
p23	NFRmAImLHS	✔	-
p24	D-NNFKAILSS	✔	X

Figure 7. Other peptide inhibitors developed against hIAPP 19-29 S20G reduce cytotoxicity. **A, B**. 10 μM hIAPP was incubated alone or with 1:1 or 1:10 molar ratio of peptide inhibitor overnight under quiescent conditions and then diluted 1:10 with pre-plated Rin5F cells, a rat pancreatic β-cell line. Cytotoxicity was quantified using MTT dye reduction. Bars show mean with one standard deviation (n = 3-9; ns = not significant; *, $p < 0.05$; **, $p < 0.01$; ***, $p < 0.001$; ****, $p < 0.0001$ using an ordinary one-way ANOVA relative to leftmost column). **C, D**. 10 μM Aβ1-42 was incubated alone or with 1:1 or 1:10 molar ratio of each peptide for 6 hours and then diluted 1:10 with pre-plated N2a cells. Cytotoxicity was quantified using MTT dye reduction. Bars represent mean with one standard deviation (n = 3-9; ns = not significant; *, $p < 0.05$; **, $p < 0.01$; ***, $p < 0.001$; ****, $p < 0.0001$ using an ordinary one-way ANOVA relative to leftmost column). **E.** Summary of peptide inhibitors and efficacies on reduction of cytotoxicity described in this study.

DISCUSSION

As detailed in the Introduction, a variety of biochemical and animal studies have linked Aβ and hIAPP, associated with AD and T2D, respectively, but the underlying cause of the link has not been clear. Previous studies point to their similar sequences and their cross-seeding property *in vivo* and *in vitro* as the underlying cause (12, 14, 18, 51). Here, through atomic structures determined using MicroED and designed inhibitors with cross-amyloid efficacy, we provide evidence for a molecular mechanism based on fibril spines having similar structures.

Although the spines of Aβ and hIAPP are similar in sequence and structure, their structural similarity is not fully reflected by their sequence similarity. This is particularly true for the A interfaces of the two segments. This observation that sequence similarity is not a sure determinant of cross-seeding efficiency has been described previously for immunoglobulin (Ig) light chains, polyglutamine tracts, and β-2 microglobulin, all of which seed Aβ 1-40 fibril formation *in vitro* (16), and this is especially true for the amyloid-like prion proteins Sup35p, Ure2p, and Rnq1p (52). The efficiency with which Aβ 24-34 WT and hIAPP 19-29 S20G fibrils seed both Aβ 1-42 and hIAPP fibril formation suggests that their common structures are important for cross-seeding.

Our experiments further support the hypothesis that the linked effects of Aβ 1-42 and hIAPP are based on their similar fibrillar structures; the peptide inhibitors, designed against Interface A of the atomic structure of hIAPP 19-29 S20G are potent in reducing cytotoxicity of both full-length hIAPP and Aβ 1-42. The mechanism for reducing cytotoxicity of hIAPP in rat pancreatic β-cells appears to involve primarily fibril inhibition. In contrast, the mechanism for reducing Aβ 1-42 cytotoxicity to neuroblastoma cells might

involve interference with oligomerization or a relatively small population of fibril polymorphs with an interface similar to Interface A observed in the Aβ 24-34 WT structure. The persistence of Aβ fibrils in the presence of inhibitor could be explained by dominance of a less toxic, but more prevalent polymorph such as one driven by Aβ 16-KLVFFA-21, (53), which we presume would not interact with our inhibitor.

In order to determine how Aβ 24-34 WT and hIAPP 19-29 S20G may cross-seed, we generated models of all twelve possible hetero-assemblies using the structures of these two segments and an ideal β-strand as templates. Next, we applied Rosetta to assess their propensities to form. Hetero-assemblies constructed using the B interfaces provided several usable models, whereas all hetero-assemblies of interface A failed to converge due to significant steric clashes. The hetero-assembly modeled onto the backbone of Interface B of the hIAPP 19-29 S20G atomic structure possess the highest shape complementarity (Sc) of all the models at 0.66 (Figure 8). Its Sc score and Rosetta Energy score are comparable to those of the homo-assemblies containing Interface B (Table 3), suggesting that this hetero-assembly model may represent an actual interface between Aβ and hIAPP.

This hetero-assembly model, taken together with the effects of the inhibitors on hIAPP and Aβ1-42 fibril formation and cytotoxicity, lead us to suggest that different fibrillar interfaces may be important for cytotoxicity and cross-seeding. Recall that the inhibitors were designed to target Interface A of the hIAPP 19-29 S20G atomic structure. Indeed, these inhibitors reduce fibril formation and cytotoxicity of full-length hIAPP, likely by targeting a similar interface in the full-length protein and preventing it from forming. In contrast, these inhibitors do not reduce fibril formation of Aβ1-42, but they do reduce its cytotoxicity. As Aβ 24-34 WT contains a structurally similar Interface A, it seems plausible

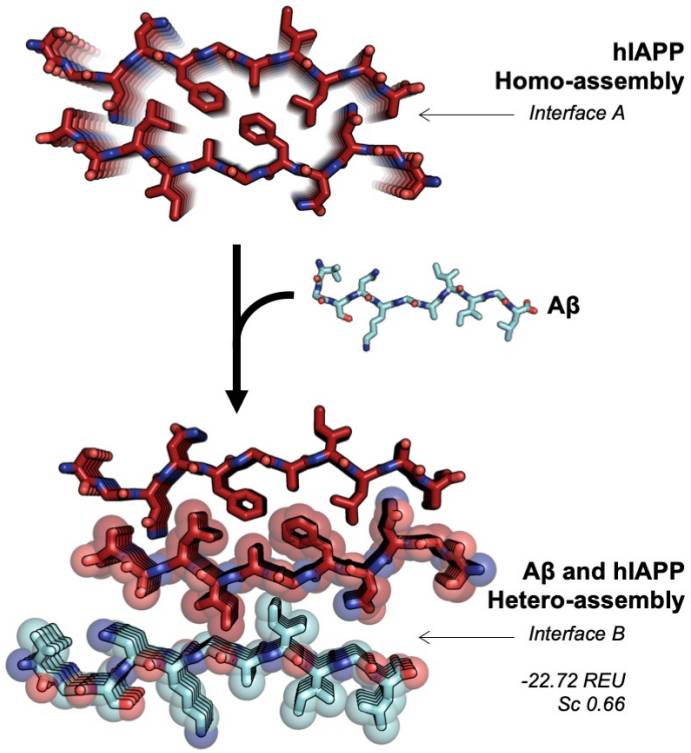


Figure 8. Model of an Aβ 24-34 WT and hIAPP 19-29 S20G hetero-assembly, which may explain how full-length Aβ and hIAPP cross-seed. The interface of the hetero-assembly model is highlighted with transparent spheres representing van der Waals radii. The model was generated from the backbone of Interface B of the hIAPP 19-29 S20G atomic structure using Rosetta. Its Rosetta Energy and shape complementarity scores are shown to its right. These scores are comparable to the Interface B homo-assemblies (Aβ 24-34 WT: -19.4 REU, Sc 0.85; hIAPP 19-29 S20G: -35.09, 0.72). Our results with the peptide inhibitors suggest that Interface A may be important for cytotoxicity.

that these inhibitors target and reduce the formation of interfaces similar to Interface A in both full-length proteins and that Interface A may be important for cytotoxicity of both proteins. Conformation-specific antibodies mOC 88, mOC 3, and mOC 22, all of which show a marked reduction in binding to Aβ1-42 incubated with inhibitors, may recognize a structural motif, or epitope, similar to Interface A. Indeed, a previous study showed that mOC 3 and mOC 22 recognize epitopes shared between Aβ and hIAPP fibrils (50). The

acceptable fit of the hetero-assembly model in Figure 7 suggests that the Interface B of both proteins is important for cross-seeding.

The fibrillar atomic structures of the segments studied here possess structural motifs important for cytotoxicity and cross-seeding, and they may also support the same properties in their parent full-length proteins. Going forward, these structures may serve as templates for the development of pharmaceutical therapeutics that may have dual efficacy.

EXPERIMENTAL PROCEDURES

Peptide Preparation- Candidate inhibitors were custom made and purchased from Innopep (San Diego, CA). For studies with the design target, 19-29 S20G, lyophilized candidate inhibitors were dissolved at 1mM in PBS and 1% DMSO. For studies with full-length hIAPP and Aβ1-42, lyophilized candidate inhibitors were dissolved at 10mM in 100% DMSO. 10mM stocks were diluted as necessary. All stocks were stored frozen at -20°C.

Human IAPP1-37NH_2 (hIAPP) was purchased for Innopep (San Diego, CA). Mouse IAPP1-37NH_2 (mIAPP) was purchased from CS Bio (Menlo Park, CA). Peptides were prepared by dissolving lyophilized peptide in 100% 1,1,1,3,3,3-Hexafluoro-2-propanol (HFIP) at 250μM for 2 hours. Next, the sample was spin-filtered and then HFIP was removed with a CentriVap Concentrator (Labconco, Kansas City, MO). After removal of the HFIP, the peptides were dissolved at 1mM or 10mM in 100% DMSO (IAPP alone) or 100% DMSO solutions containing 1mM or 10mM inhibitor. The DMSO peptide stocks were

diluted 100-fold in filter-sterilized Dulbecco's PBS (Cat. # 14200-075, Life Technologies, Carlsbad, CA).

Recombinant Amyloid Beta Peptide Cloning and Expression- Aβ was cloned and purified similar to the methods described in Laganowsky, et al (54). Aβ was cloned into p15-MBP as previously described and expressed with the following exceptions. An overnight starter culture was grown in 100 mL instead of 50 mL, 15 mL, instead of 7mL, of which was used to inoculate 1 L. After induction, cells were allowed to grown for 3-4 hours at 37 °C (instead at 34 °C). Cells were then harvested by centrifuging at 5,000 x g. The cell pellet was frozen and stored at -80˚C.

The cell pellet was thawed on ice and re-suspended in buffer A (50 mM sodium phosphate, 0.3 M sodium chloride, 20 mM imidazole, pH 8.0) at 120 mL per 3L of culture volume and lysed by sonication. Crude cell lysate was clarified by centrifugation at 15,000 x g for 30 minutes at 4˚C. The clarified cell lysate was filtered through a 0.45 μm syringe filtration device (HPF Millex-HV, Millipore, Billerica, MA) before loading onto two 5mL HisTrap-HP columns (GE Healthcare, Piscataway, NJ). The HisTrap-HP column was washed with five column volumes of buffer A and then washed in five column volumes of 10% buffer B (50 mM sodium phosphate, 0.3 M sodium chloride, 500 mM imidazole, pH 8.0). Protein eluted was eluted in 3 column volumes of 100% buffer B. The pooled sample diluted to less than 10mg/ml and was loaded into 6,000-8,000 MWCO tubing (Fisher Scientific, Pittsburgh, PA), and dialyzed against buffer C (25 mM Tris pH 8.0, 20 mM imidazole, 100 mM sodium chloride) at 4˚C for 4 hours, changing buffer after 2 hours. The dialyzed sample was pooled and 1/50 volume of TEV protease stock was added. The TEV protease reaction was incubated overnight at 4˚C before loading over a 5mL HisTrap-HP

column equilibrated in buffer A. The flow through was collected, containing the recombinant Aβ peptide. Pooled recombinant Aβ peptide was 0.22 μm filtered (Steriflip, Millipore, Billerica, MA) and further purified by reverse phase high performance liquid chromatography (RP-HPLC) on a 21.2x250mm Agilent 897250-106 Zorbax StableBond 300 C8 PrepHT cartridge, 7um beads at 80 ˚C equilibrated in buffer RA (0.1% trifluroacetic acid (TFA)/water) and eluted over a linear gradient from 15% to 50% buffer RB (Acetonitrile/0.1% TFA) in 59 minutes at a flow rate of 10 mL/min. Absorbance at 220nm and 280nm were recorded using a Waters 2487 dual ʎ absorbance detector (Waters, Milford, MA). Peak fractions containing peptide were assessed for purity by MALDI-TOF mass spectrometry (Voyager-DE-STR, Applied Biosystems, Carlsbad, CA). Pooled fractions were frozen in liquid nitrogen and lyophilized. Dried peptide powders were stored in desiccant jars at -20˚C.

Crystallization- 24-VGSNKGAIIGL-34 (Aβ 24-34 WT) was dissolved at 7.5 mg/ml in 25 mM citric acid pH 4.0 and 5% DMSO. Micro crystals were grown in batch at 37°C, shaking. Crystals grew within 2 days to a maximum of 1 week.

MicroED data collection- The procedures for MicroED data collection and processing largely follow published procedures (36, 55). Briefly, a 2-3 μl drop of crystals in suspension was deposited onto a Quantifoil holey-carbon EM grid then blotted and vitrified by plunging into liquid ethane using a Vitrobot Mark IV (FEI, Hillsboro, OR). Blotting times and forces were optimized to keep a desired concentration of crystals on the grid and to avoid damaging the crystals. Frozen grids were then either immediately transferred to liquid nitrogen for storage or placed into a Gatan 626 cryo-holder for imaging. Images and diffraction patterns were collected from crystals using FEI Tecnai 20 TEM with field

emission gun (FEG) operating at 200 kV and fitted with a bottom mount TVIPS TemCam-F416 CMOS-based camera. Diffraction patterns were recorded by operating the detector in a video mode using electronic rolling shutter with 2 x 2 pixel binning (38). Exposure times for these images were either 2 or 3 seconds per frame. During each exposure, crystals were continuously unidirectionally rotated within the electron beam at a fixed rate of 0.3 degrees per second, corresponding to a fixed angular wedge of 0.6 or 0.9 degrees per frame.

Crystals that appeared visually undistorted produced the best diffraction. Datasets from individual crystals were merged to improve completeness and redundancy. Each crystal dataset spanned a wedge of reciprocal space ranging from 40-80°. We used a selected area aperture with an illuminating spot size of approximately 1 μm. The geometry detailed above equates to an electron dose rate of less than 0.01 $e^{-}/Å^{2}$ per second being deposited onto our crystals.

Measured diffraction images were converted from TIFF format into SMV crystallographic format, using publicly available software (available for download at http://cryoem.janelia.org/downloads).

We used XDS to index the diffraction images and XSCALE (56) for merging and scaling together datasets originating from five different crystals.

Structure determination- We determined the structure of Aβ 24-34 WT using molecular replacement. An idealized 10-residue peptide strand with the sequence GAAGAIIGA led us to our atomic model. The solution was identified using Phaser (57). Subsequent rounds of model building and refinement were carried out using COOT and Phenix, respectively (58, 59).. Electron scattering factors were used for refinement. Some

reflections extended to 1.42 Å resolution. Although the outer shell was incomplete (48% complete), we retained this data as being potentially helpful in the refinement. Statistics are reported to 1.5A resolution, where completeness reaches 75% (60). Calculations of the area buried and Sc were performed with AREAIMOL (61, 62)) and Sc (63–65), respectively.

Fibril diffraction- Fibrils of Aβ 1-42 or microcrystals of Aβ 24-34 WT were spun down and washed with water three times to remove any salt using a tabletop microfuge. The samples were concentrated 20x in water and applied between two capillary ends and then the samples were left to dry overnight. Fibrils were analyzed with a RIGAKU R-AXIS HTC imaging plate detector using Cu K(alpha) radiation from a FRE+ rotating anode generator with VARIMAX HR confocal optics (Rigaku, Tokyo, Japan). Radial profiles were calculated using a program written in-house. The program calculates the average intensity as a function of distance from the beam center.

Atomic structure overlay- A structural superpostion of Aβ 24-34 WT and hIAPP 19-29 S20G was performed using LSQKAB from the CCP4 Suite (66). We calculated root mean square deviation (RMSD) of main chains.

Computational structure-based design- Computational designs were carried out using the RosettaDesign software as described previously (47). The atomic structure of the 19-SGNNFGAILSS-29 hIAPP segment was used as a starting template for computational design. An extended L-peptide (or D-peptide, seven to nine residues) was first placed at either top or bottom of the starting template of hIAPP 19-29 S20G atomic structure. The design procedure then built side-chain rotamers of all residues onto the nine-residue peptide backbone placed at growing end of fibril. The optimal set of rotamers was identified as those that minimize an energy function containing a Lennard-Jones potential,

an orientation-dependent hydrogen bond potential, a solvation term, amino acid-dependent reference energies, and a statistical torsional potential that depends on the backbone and side-chain dihedral angles. Area buried and shape complementarity calculations were performed with areaimol and Sc, respectively, from the CCP4 suite of crystallographic programs (61). The solubility of each peptide was evaluated by hydropathy index (67) and its aggregation propensity was calculated by self-stacking score (Jiang et al., unpublished data). The designed peptides were selected based on calculated binding energy of top or bottom binding mode, shape complementarity and peptide solubility. Each structural model of selected peptides went through human inspection using Pymol, where those peptides with sequence redundancy and less binding interactions were omitted. Finally, select peptides were synthesized and tested experimentally.

Testing of candidate inhibitors with design target- To test whether the candidate inhibitors prevent fibril formation of the design target, 19-29 S20G, we dissolved the lyophilized 19-29 S20G peptide at 1 mM in PBS and 1% DMSO or in an equimolar solution of candidate inhibitor in PBS and 1% DMSO. Samples were incubated for 6 hours to 15 hours at room temperature under quiescent conditions. Fibril abundance was checked using electron microscopy.

Next, the samples were applied to pre-plated HEK293 cells for 24 hours, and then cell viability was measured using MTT dye reduction.

Transmission electron microscopy-Samples were spotted onto non-holey grids and left for 160 to 180 seconds. Remaining liquid was wicked off and then left to dry before analyzing. Samples for negative-stain TEM were treated with 2% uranyl acetate after

sample was wicked off the grid. After 1 minute, the uranyl acetate was wicked off. The grids were analyzed using a T12 Electron Microscope (FEI, Hillsboro, OR). Images were collected at 3,200 or 15,000x magnification and recorded using a Gatan 2kX2k CCD camera.

Thioflavin-T (ThT) kinetic assays- Thioflavin-T (ThT) assays with hIAPP were performed in black 384-well plates (Nunc, Rochester, NY) sealed with UV optical tape. hIAPP1-37NH_2 and mIAPP1-37NH_2 were prepared as described. The total reaction volume was 50 μL per well. ThT fluorescence was recorded with excitation and emission of 444 nm and 482 nm, respectively, using a Varioskan Flash (Thermo Fisher Scientific, Grand Island, NY). Experiments were performed at 25°C without shaking in triplicate and readings were recorded every 5 minutes.

For the seeding assays in Figure 4, 1 mM of hIAPP1-37NH_2 in 100% DMSO was diluted 1 to 100 in 0.1 M NaOAc pH 6.5 containing 10% monomer-equivalent seed and 10μM ThT. Seeds of Aβ, Aβ 24-34 WT, and hIAPP 19-29 S20G were sonicated for five minutes prior to addition; seeds of hIAPP were not sonicated.

For the inhibition assays in Figure 6, 1 mM of hIAPP1-37NH_2 in 100% DMSO was diluted 1 to 100 in PBS buffer containing 10 μM ThT. Stocks of each inhibitor were diluted 1 to 100 in the same manner.

ThT assays with Aβ were performed as above with the following exceptions. Experiments were performed in black 96-well plates (Nunc, Rochester, NY) sealed with UV optical tape. The total reaction volume was 180μL per well; Experiments were performed at 37°C without shaking in triplicate and readings were recorded every 5 minutes.

For seeding experiments, 1 mM of Aβ in 100% DMSO was diluted 1 to 100 in PBS containing 10% monomer-equivalent seed and 10μM ThT. Seeds of Aβ, Aβ 24-34 WT and

hIAPP 19-29 S20G were sonicated for five minutes prior to addition; seeds of hIAPP were not sonicated.

For inhibition experiments, 1 mM of Aβ in 100% DMSO was diluted 1 to 100 in PBS containing 25μM ThT. Stocks of each inhibitor were diluted 1 to 100 in the same manner.*Cell culture*- HEK293 cells were a gift from Carol Eng in the laboratory of Arnold J. Berk at UCLA. Cells were cultured in DMEM media (Cat. # 11965-092, Life Technologies) plus 10% heat-inactivated fetal bovine serum and 1% pen-strep (Life Technologies). Cells were cultured at 37°C in 5% CO_2 incubator.

Rin5F cells were purchased from ATCC (Cat. # CRL-2058, Manassas, VA). Cells were cultured in RPMI media (ATCC, Cat. # 30-2001) plus 10% heat-inactivated fetal bovine serum. Cells were cultured at 37°C in a 5% CO_2 incubator.

Nuero2a (N2a) cells were a gift from the Pop Wongpalee in the laboratory of Douglas Black at UCLA. Cells were cultured in MEM media (Cat. # 11095-080, Life Technologies) plus 10% heat-inactivated fetal bovine serum and 1% pen-strep (Life Technologies). Cells were cultured at 37°C in 5% CO_2 incubator.

3-(4,5-dimethylthiazol-2-yl)-2,5-diphenyltetrazolium bromide (MTT) dye reduction assay for cell viability- HEK293 cells, Rin5F cells, and N2a cells were plated at 10,000, 27,000, and 15,000 cells per well in 90 μL, respectively, in clear 96-well plates (Cat. # 3596, Costar, Tewksbury, MA). Cells were allowed to adhere to the plate for 20-24 hours. For cell assays with Aβ 24-34 WT, fibrillar samples were incubated for at least 4 days and soluble samples were freshly dissolved and then applied to N2a cells. For cell assays with the design target, hIAPP 19-29 S20G, samples were incubated with or without inhibitors for 6-15 hours and then applied to HEK293 cells. For cell assays with full-length hIAPP, samples

were incubated with or without inhibitors for 15 hours to 1 week and then applied to Rin5F cells. For cell assays with Aβ1-42, samples were incubated with or without inhibitors for 6 hours at 37°C and then applied to N2a cells. 10 µL of sample was added to cells. By doing this, samples were diluted 1/10 from *in vitro* stocks. Experiments were done in triplicate.

After a 24-hour incubation, 20 µL of Thiazolyl Blue Tetrazolium Bromide MTT dye (Sigma, St. Louis, MO) was added to each well and incubated for 3.5 hours at 37°C under sterile conditions. The MTT dye stock is 5 mg/mL in Dulbecco's PBS. Next, the plate was removed from the incubator and the MTT assay was stopped by carefully aspirating off the culture media and adding 100 µL of 100% DMSO to each well. Absorbance was measured at 570 nm using a SpectraMax M5. A background reading was recorded at 700 nm and subsequently subtracted from the 570 nm value. Cells treated with vehicle alone (PBS+0.1%DMSO) were designated at 100% viable, and cell viability of all other treatments was calculated accordingly.

We determined the appropriate statistical test for significance by assessing whether 1). The sample sets had a Gaussian distribution using a D'Agostino-Pearson omnibus normality test and 2). The sample sets had equal variance using a Bartlett's test or F test. For samples with Gaussian distributions and equal variances, we employed an unpaired t-test with equal standard deviations. For samples with Gaussian distributions, but unequal variances, we employed an unpaired t-test with Welch's correction. For samples with non-Gaussian distributions and unequal variances, we employed a Mann-Whitney U-test.

Detection of Caspase-3/7- N2a cells were plated at 7,200 cells per well in black-walled 96 well plates (Cat. # 3603, Costar) and treated as described in the previous section.

After a 24 hour treatment, cell media was aspirated and then 100 µL of 2 µM Nexcelom ViaStain Live Caspase 3/7 in PBS (Cat. # CSK-V0003-1, Nexcelom Bioscience LLC, Lawrence, MA) was added to each well. The stain was incubated with cells at 37°C for 30 minutes, and then the cells were imaged using a Celigo Image Cytometer (Nexcelom Biosciences) and a Zeiss fluorescent microscope. Cells treated with 2 µM staurosporine were used as a positive control for caspase activation.

Hetero-Assembly Model- Energies and structures for the hetero-assembly models were calculated using the 3D profile method (68). Using Rosetta, the sequences of Aβ 24-34 WT and hIAPP 19-29 S20G were "threaded" onto three template backbone structures: the Aβ 24-34 WT backbone, the hIAPP 19-29 S20G fiber backbone, and an idealized beta-sheet fiber backbone. The distance between the beta-sheets of each of these threaded structures was varied by 10 Å, in increments of 0.25 Å and the shift along the stand axis was 20 Å, also by 0.25 Å increments. Each of the structures was scored by Rosetta Energy, buried surface area, and shape complementarity (69)

Dot Blot Assay- Aβ1-42 samples were incubated at 10 µM with or without inhibitors for 6 and 24 hours at 37°C, and spotted onto a nitrocellulose membrane (Cat. # 162–0146, BioRad, Hercules, CA). 20µL was loaded for each condition; 2µL was spotted at a time and allowed to dry between application. The membranes were blotted as previously described (35), with the exception of the primary antibodies used. The antibodies used in the assay were previously generated and characterized (50)

ACKNOWLEDGEMENTS

We thank Dan Anderson for general support in the laboratory and Jeannette Bowler for providing purified α-synuclein for our aggregation inhibition studies. We thank the UCLA-DOE X-ray Crystallography Core Technology Center; the Janelia Research Campus visitor program and Ivo Atanasov and the Electron Imaging Center for NanoMachines (EICN) of California NanoSystems Institute (CNSI) at UCLA for the use of their electron microscopes. The UCLA-DOE X-ray Crystallization Core Technology Center is supported in part by the Department of Energy grant DE-FC0302ER63421.

COMPETING INTERESTS

DSE is a SAB member and equity holder in ADRx, Inc.

AUTHOR CONTRIBUTIONS

PK and SLG conceived and designed this study, interpreted results and co-wrote the manuscript. SLG crystallized, solved and analyzed Aβ 24-34 WT, purified Aβ1-42, performed the Aβ and alpha synuclein aggregation assays, prepared Aβ samples for toxicity and dot blot assays. PK designed and screened inhibitors, performed structural alignments, cultured cells, executed and analyzed toxicity experiments, performed hIAPP aggregation assays. MRS performed structural alignments, helped solve and analyze the Aβ 24-34 WT structure, and revised the manuscript. DC helped solve and analyze the Aβ 24-34 WT structure. LJ designed inhibitors for hIAPP 19-29 S20G. KM provided the hetero-assembly model calculations. JAR screened crystals and collected MicroED data of Aβ 24-34 WT. TG and DS acquired and analyzed MicroED diffraction data. LS and JL performed and analyzed

the TTR aggregation assay. PS performed and analyzed the Tau aggregation assay. SP and CGG generated essential material for experiments and performed and analyzed the dot blot assay. DSE conceived the idea for the project, secured funding, interpreted results and revised the manuscript. All authors reviewed the results and approved the final version of the manuscript.

FOOTNOTES

This project was supported by the National Institutes of Health (NIH) (R01 AG029430).

The abbreviations used are: AD, Alzheimer's disease; T2D, Type-II diabetes; Aβ, amyloid-β; hIAPP, human islet amyloid polypeptide; MicroED, Micro-Electron Diffraction; N2a, Neuro-2a; ThT, thioflavin-T; SASA, solvent-accessible surface area; Sc, shape complementarity; MTT, 3-(4,5-dimethylthiazol-2-yl)-2,5-diphenyltetrazolium bromide.

The atomic coordinates and associated structure factors have been deposited in the Protein Data Bank (5VOS) and the EMDatabank (EMID-8720).

SUPPLEMENTAL INFORMATION

EXPERIMANTAL PROCEDURES

Aggregation Inhibition Assay with Transthyretin (TTR)- The TTR aggregation and immunoblot assays largely follow the protocol described in Saelices, *et al.* (70). TTR was aggregated at 1 mg/ml in 10 mM sodium acetate (pH 4.3), 100 mM KCl, 10 mM EDTA under quiescent conditions at 37 °C for a maximum of 4 days. TTR was aggregated in the presence and absence of peptide inhibitors at a ratio of 1:10 (TTR monomer:inhibitor). On each day of aggregation, absorbance at 400 nm was recorded to measure sample turbidity. On the final day of aggregation, the concentration of the insoluble fraction was measured. To do this, we first spun down 100 µL of sample at 13,000 rpm for 30 min. Next, the pellet was washed with fresh buffer and spun again and then re-spun. The pellet was dissolved in 6 M guanidine chloride, and then absorbance was measured at 295 nm. Absorbance was used to calculate the concentration of the insoluble fraction. Additionally, TTR aggregation on the final day was measured using dot blot analysis as described (71) using the SuperSignal West HisProbe™ kit following the manufacturer's instructions (Thermo Scientific). The insoluble fraction of the samples after 4 days of incubation was dotted onto nitrocellulose membranes (0.2 µm; BioRad). A dilution ratio of 1:10,000 was used for the HisProbe.

Aggregation Inhibition Assay with Tau- We used a construct of tau called K18 that contains only the 4 repeat domains of the full-length protein. Peptide inhibitors were tested by shaking 25 µM K18 in a 96-well plate at 700 rpm in PBS buffer (pH 7.4) with 40 µM ThT and 2 mM DTT. 0.5 mg/ml heparin and a two-fold molar excess of inhibitor were added. Inhibitors were diluted to the appropriate concentration from 10 mM stocks in 100% DMSO. ThT fluorescence was measured using a FLUOstar Omega plate reader with

excitation and emission wavelengths of 440 and 480 nm, respectively. Averaged curves were generated from triplicate measurements.

Aggregation Inhibition Assay with α-synuclein- α-synuclein was expressed and purified as described previously in Rodriguez, *et al.* with the following exceptions to the expression protocol. An overnight starter culture was grown in 15 mL instead of 100 mL, 7 mL of which was used to inoculate 1 L. After induction, cells were allowed to grown for 3-4 hours at 34 °C (instead of 4-6 hours at 30 °C). Cells were then harvested by centrifuging at 5,000 x g.

ThT assays with α-synuclein were performed in black 96-well plates (Nunc, Rochester, NY) sealed with UV optical tape. The total reaction volume was 180 µL per well. ThT fluorescence was recorded with excitation and emission of 444 nm and 482 nm, respectively, using a Varioskan Flash (Thermo Fisher Scientific, Grand Island, NY). Experiments were performed at 37°C, shaking at 600 rpm with a teflon bead, in triplicate and readings were recorded every 15 minutes. Alpha synuclein at 105 µM in PBS was diluted to a final concentration of 50 µM in 25 µM Thioflavin-T and PBS. Inhibitors were added at the specified concentration by diluting 10 mM stocks in 100% DMSO 1 to 40 in the same manner. Thus, inhibitors were tested at 5:1 molar excess of α-synuclein.

Thioflavin-T (ThT) kinetic assays with Aβ and hIAPP- Lag times were estimated by calculating the EC15 for each individual replicate using the four-parameter logistic equation function ECanything with F=15 in GraphPad Prism 7.0.

Table 2. Computed binding properties of designed inhibitors to hIAPP 19-29 S20G

Peptide Name	Sequence	MW (g/mol)	Hydropathy Index	Self-Stacking Propensity	Binding Energy (Top)	Binding Energy (Bottom)	SC (Top)	SC (Bottom)	SA Buried (Top)	SA Buried (Bottom)
p1	NFKmAImLH	869.6	2.3	-13.184	-31.734	-31.051	0.708	0.753	552	564
p4	NFWAKLN	891.5	-3.4	-9.3	-33.4	-32.7	0.8	0.81	614	590
p6	TFYATLH	851.4	2.5	-11.9	-30.5	-29.6	0.7	0.78	547	579
p8	NLGPVLP	707.9	4.7	-6.196	-10.536	-10.625	0.682	0.613	531	534
p11	AcNFEAYLHS-NH_2	979.1	-3.1	-11.782	-33.449	-31.004	0.837	0.759	580	565
p12	AcTFYAELYS-NH_2	992.1	1.6	-10.06	-27.862	-30.093	0.684	0.765	564	572
p13	AcHFNELYNS-NH_2	1022.1	-8.4	-12.148	-24.92	-27.122	0.703	0.73	503	515
p14	D-NFEAYLH	893.0	-3.1	-11.782	-26.444	-26.575	0.672	0.701	539	478
p15	D-ELFAHYN	893.0	-3.1	-11.404	-30.454	-18.686	0.652	0.644	586	534
p16 (-)	D-NAEAALH	724.8	4	-8.928	-22.887	-20.944	0.583	0.564	460	431
p17 (-)	D-ELAAHAN	724.8	4	-9.118	-25.142	-20.122	0.574	0.773	499	381
p21	NNFYAELYSS	1206.4	-1.2	-11.588	-29.438	-30.683	0.698	0.753	580	570
p22	AcNNFYAELYSS-NH_2	1247.5	-1.2	-11.588	-29.438	-30.745	0.697	0.765	582	564
p23	NFRmAImLHS	984.5	1.7	-9.692	-31.739	-30.996	0.696	0.761	563	563
p24	D-NNFKAILSS	992.5	5.5	-14.326	-27.803	-23.709	0.649	0.724	513	444

Table 3. Aβ 24-34 WT and IAPP 19-29 S20G heterozipper and homozipper model Rosetta interaction energies.

Threaded structure	Rosetta energy (R.E.U.)	R.E.U per residue	Shape complementarity	Area Buried (Å^2)	SASA (Å^2)
Heterozippers*					
Interface = B; backbone = IAPP threaded sequence = VGSNKGAIIGL + SGNNFGAILSS	-21.3	-1.0	0.65	132	6649
Interface = B; backbone = IAPP threaded sequence = SGNNFGAILSS + VGSNKGAIIGL	-22.7	-1.0	0.66	130	6646
Interface = B; backbone = Aβ threaded sequence = VGSNKGAIIGL + SGNNFGAILSS	-10.6	-0.5	0.60	175	6146
Interface = B; backbone = Aβ threaded sequence = SGNNFGAILSS + VGSNKGAIIGL	-6.6	-0.3	0.57	179	6206
Interface = B; backbone = ideal threaded sequence = VGSNKGAIIGL + SGNNFGAILSS	234.6	10.7	N/A	N/A	N/A
Interface = B; backbone = ideal threaded sequence = SGNNFGAILSS + VGSNKGAIIGL	234.6	10.7	N/A	N/A	N/A
Homozippers					
Interface = A; backbone = IAPP threaded sequence = SGNNFGAILSS + SGNNFGAILSS	-40.2	-1.8	0.81	395	5194
Interface = B; backbone = IAPP threaded sequence = SGNNFGAILSS + SGNNFGAILSS	-35.1	-1.6	0.90	128	6413
Interface = A; backbone = Aβ threaded sequence = VGSNKGAIIGL + VGSNKGAIIGL	-3.1	-0.1	0.74	370	5314
Interface = B; backbone = Aβ threaded sequence = VGSNKGAIIGL + VGSNKGAIIGL	-19.4	-0.9	0.59	281	5525

*Threaded structure calculations for interface A were not able to converge due to significant steric clashes

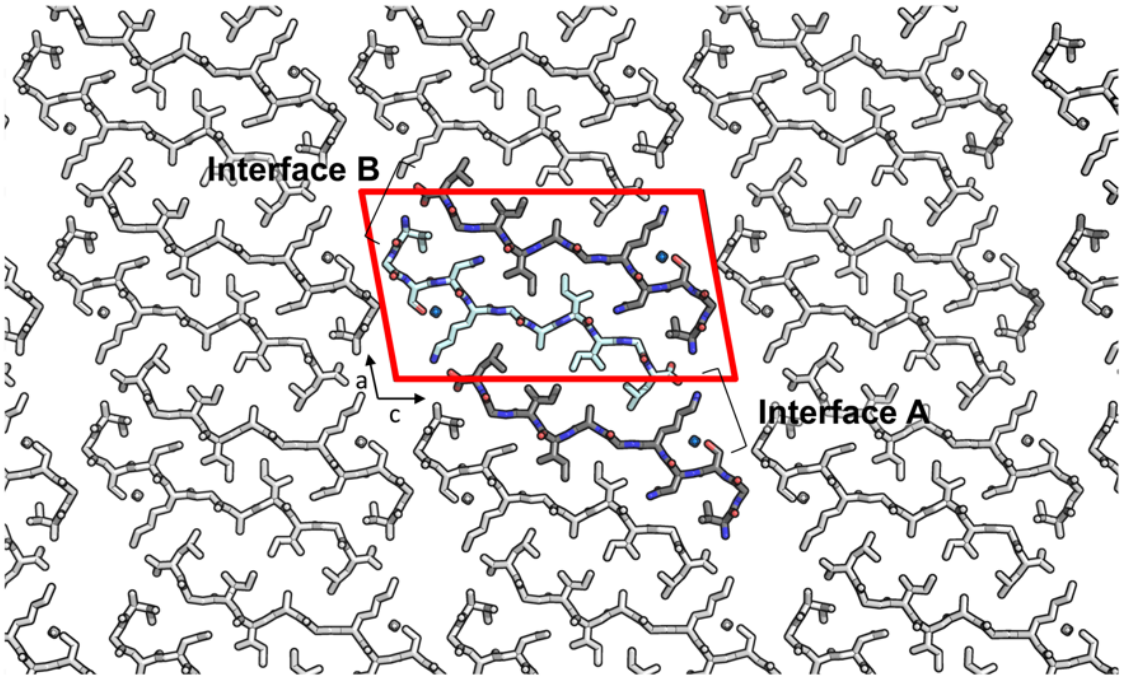


Figure 9. Crystal packing of the Aβ 24–34 WT atomic structure reveals two interfaces. View down the b axis of the unit cell, outlined in red.

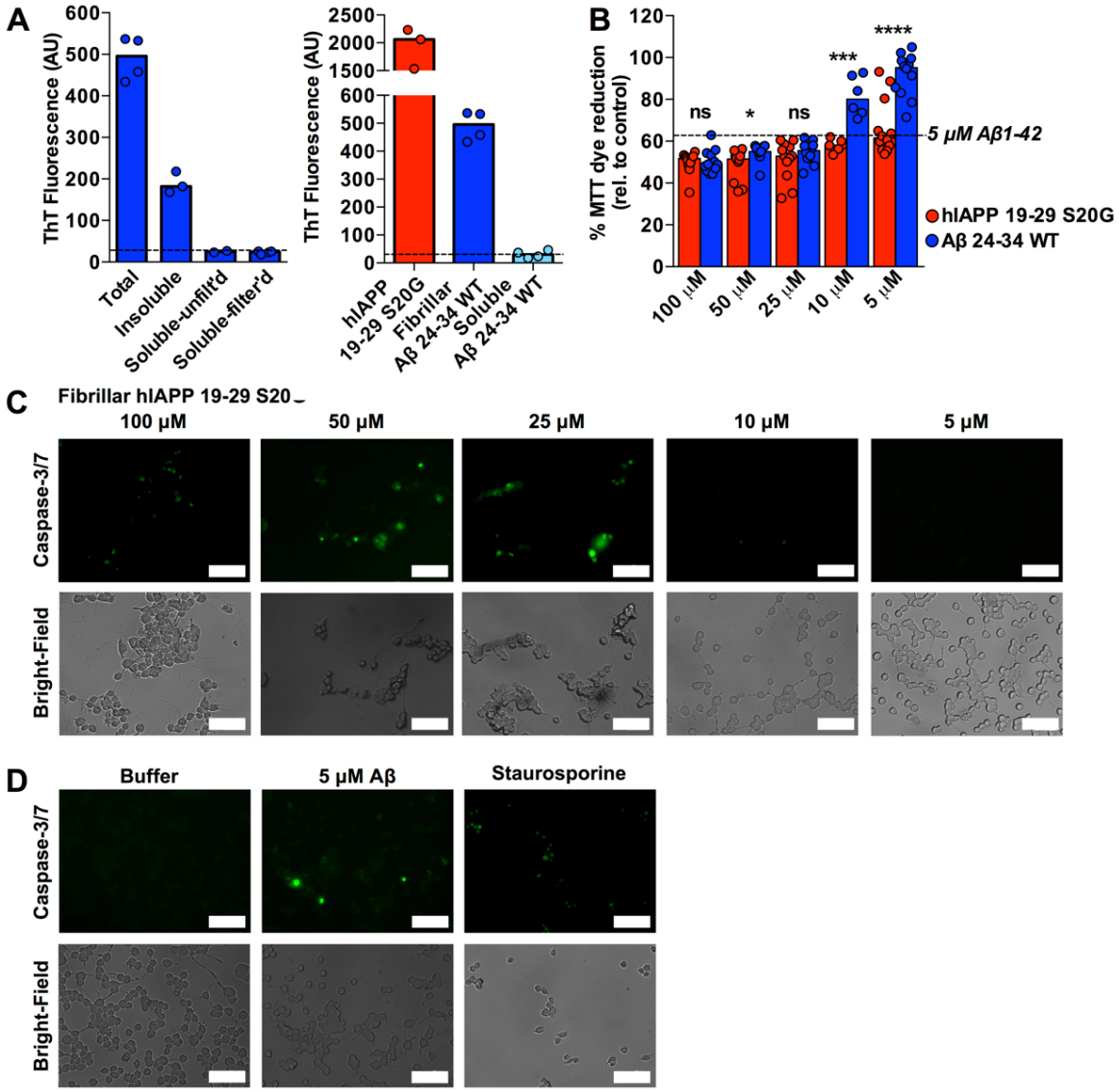


Figure 10. Fibrillar forms of Aβ 24-34 WT and hIAPP 19-29 S20G are cytotoxic to N2a cells. **A.** Samples of Aβ 24-34 WT and hIAPP 19-29 S20G that contain fibrils show high Thioflavin-T (ThT) fluorescence, whereas soluble samples show very low fluorescence. The dashed lines on both graphs represent fluorescence from buffer alone. **B.** hIAPP 19-29 S20G is more cytotoxic than Aβ 24-34 WT at select concentrations. Cytotoxicity was quantified using MTT dye reduction. Points show mean with one standard deviation (n = 12; ns = not significant; *, $p < 0.05$; ***, $p < 0.001$; ****, $p < 0.0001$ using a unpaired t-test with equal standard deviations). **C.** hIAPP 19-29 S20G activates pro-apoptotic caspases. Cells were imaged using a Zeiss fluorescent microscope. **D.** Images of cells treated with

negative and positive controls and then stained for caspase-3/7 activity. Scale bars are 50 μm.

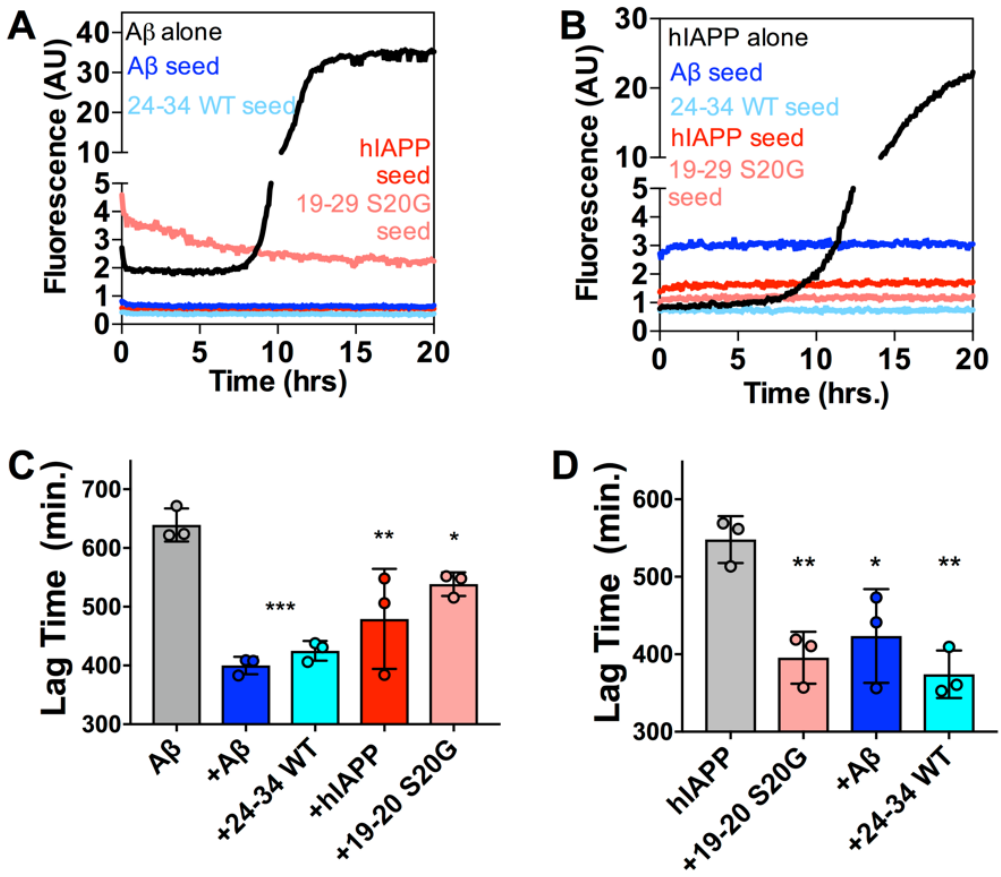


Figure 11. Extended ThT assay data. Seeds used in the ThT assay in Figure 4 do not bind ThT in conditions used for Aβ ThT assay (**A**) or in conditions used for hIAPP ThT assay (**B**). Seeding reduces lag time of aggregation of Aβ (**C**) and hIAPP (**D**). Lag times were calculated using the EC15value of each replicate. Seeding from hIAPP in (**D)** could not be calculated as aggregation had already initiated by the time of the first reading**.** Columns show mean with one standard deviation and technical replicates (n = 3; ns = not significant; *, $p < 0.0332$; **, $p < 0.0021$; ***, $p < 0.0002$ using an ordinary one-way ANOVA, values are relative to unseeded aggregation in leftmost column).

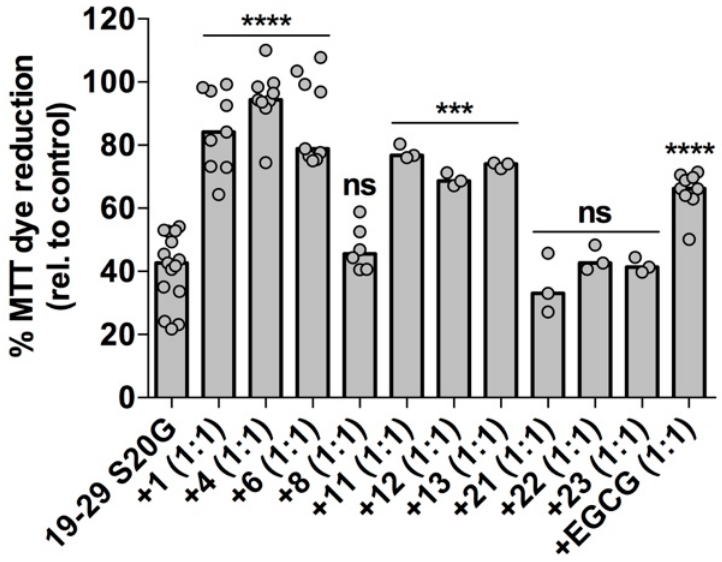


Figure 12. Other inhibitors developed with structure-based design against the hIAPP 19-29 S20G structure also reduce cytotoxicity of hIAPP 19-29 S20G. 1 mM hIAPP 19-29 S20G was incubated with equimolar concentrations of each inhibitor overnight under quiescent conditions. Samples were prepared as described in Figure 5D and then applied to HEK293 cells at 10 μM final concentration for 24 hours. Cytotoxicity was quantified using MTT dye reduction. EGCG, a flavanol know to mitigate hIAPP 19-29 S20G cytotoxicity by reducing fibril formation, was used as a positive control. Columns show mean with individual replicates(n = 3-9; ns = not significant; ***, $p < 0.0005$; ****, $p < 0.0001$ using an ordinary one-way ANOVA. Values are relative to leftmost column).

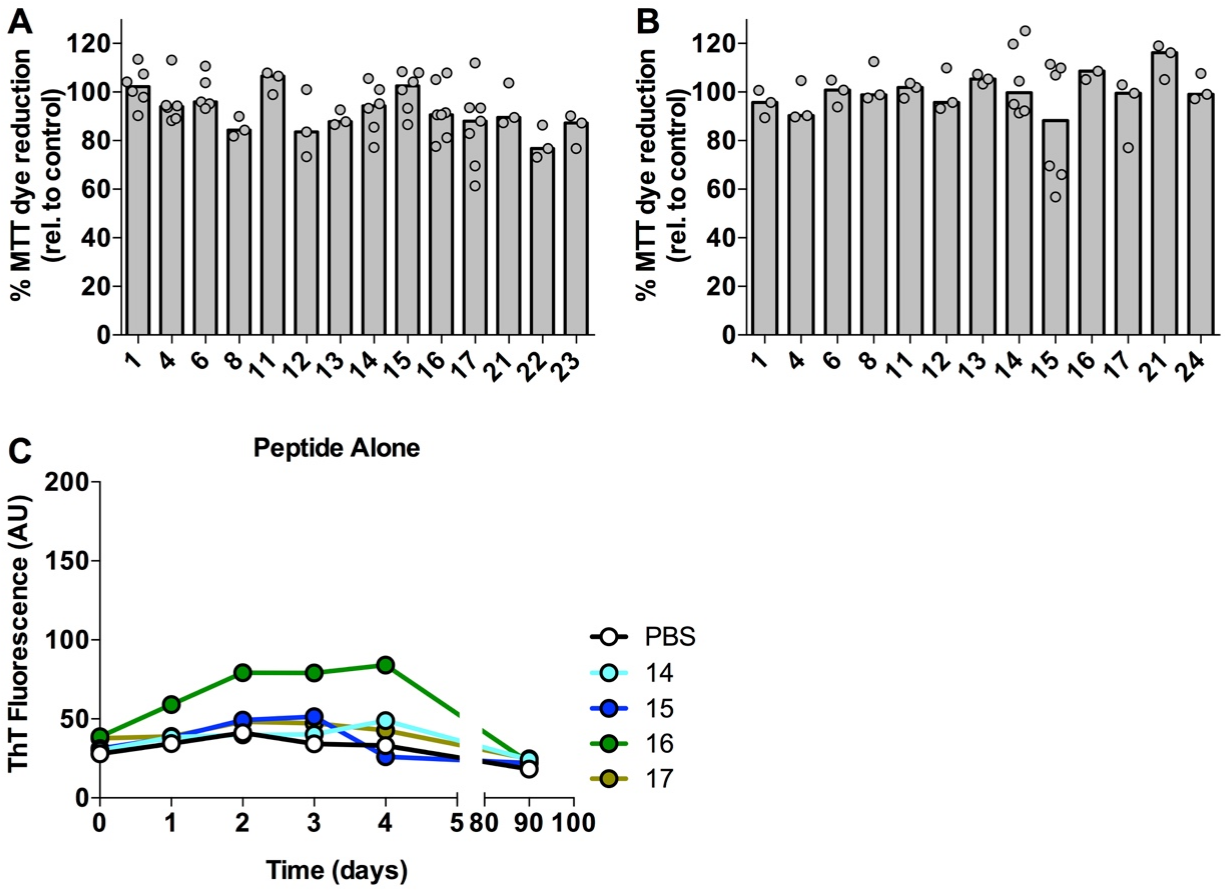


Figure 13. Inhibitors are not cytotoxic and they do not form fibrils. 10 μM of each inhibitor was applied to Rin5F cells (**A**) or N2a cells (**B**) for 24 hours and then cytotoxicity was quantified using MTT dye reduction. **C.** Inhibitors alone do not form fibrils as assessed with Thioflavin-T (ThT) binding. 100 μM of each inhibitor was incubated with 100 μM ThT at 25 °C under quiescent conditions.

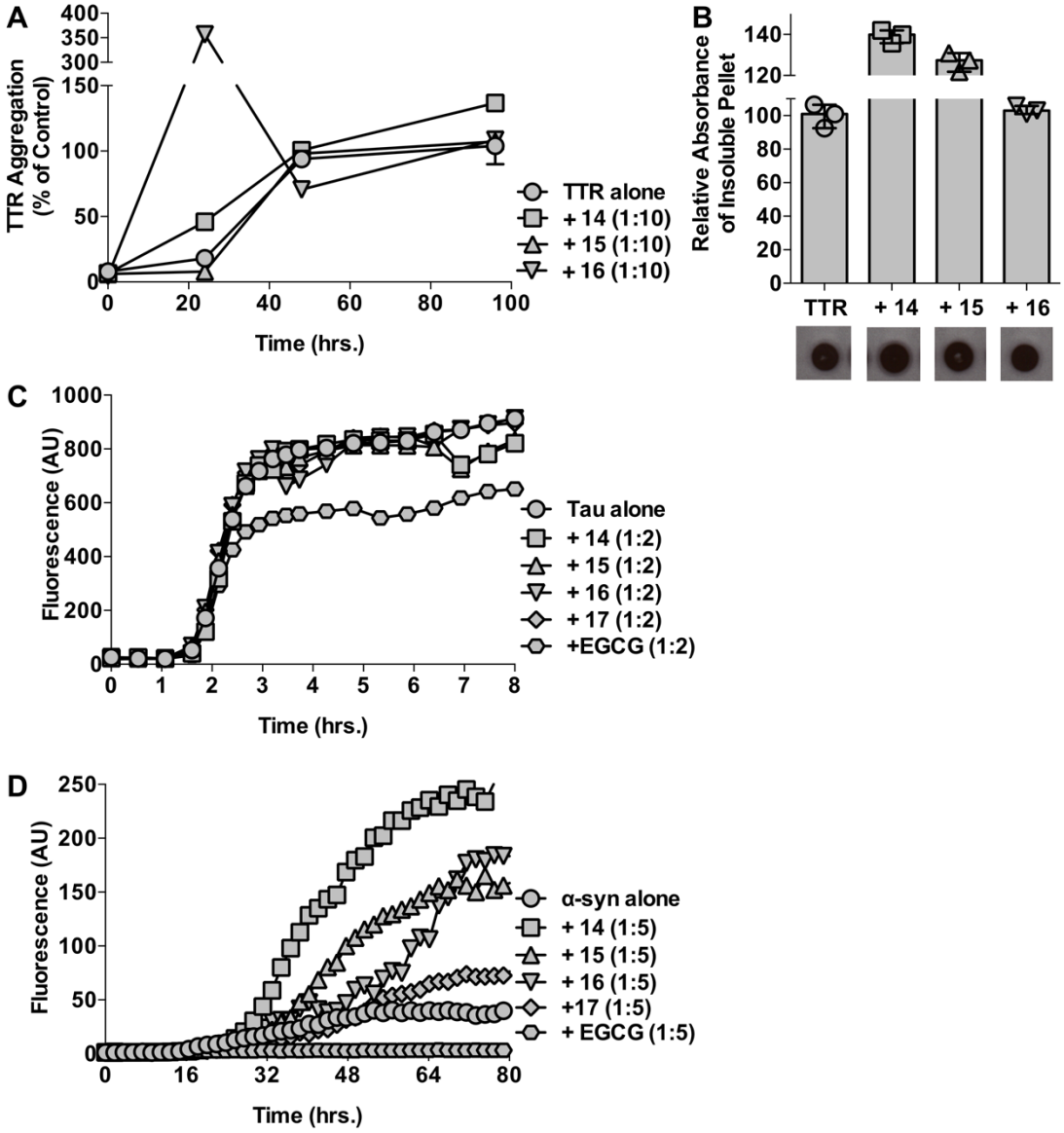


Figure 14. Peptide inhibitors p14 and p15 are specific for the design target and they do not reduce fibril formation of two other amyloid proteins, transthyretin (TTR) and tau. **A.** and **B.** Peptide inhibitors, p14 and p15, and negative control peptide p16, do not reduce TTR fibril formation**. A.** TTR fibril formation was monitored by measuring absorbance at 400 nm over a 4-day period. Points were normalized to the average of TTR alone at day 4. Individual points show median with range across triplicates. Most of the range bars are the same size or smaller than the symbols in the graph. **B.** On day 4 of the TTR aggregation assay, the insoluble fractions of the reactions were isolated with centrifugation and then

dissolved in guanidinium hydrochloride. Next the dissolved insoluble fraction was quantified by measuring absorbance at 280 nm, and by dot blot analysis with an anti-His antibody (the transthyretin protein used in these studies contained a N-terminal His-tag). Graph shows median with range. **C.** Peptides p14, p15, p16, and p17 do not reduce fibril formation of the K18 tau construct. K18 contains only the four repeat domains of the full-length protein. Small molecule epigallocatechin-3-gallate (EGCG), a known inhibitor of K18 fibril formation (72), slightly reduces fibril formation. Lines show average of 3 replicates. **D.** Peptides p14, p15, p16, and p17 do not reduce fibril formation of α-synuclein. EGCG was used as a positive control for fibril inhibition (73). Lines show average of 3 replicates.

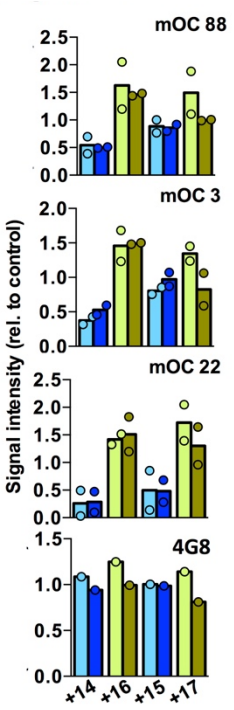


Figure 15. Quantification of antibody-binding experiments. Peptide-based inhibitors reduce the formation of Aβ1-42 assemblies recognized by certain conformational monoclonal antibodies, while negative control peptides do not. Signal intensity was normalized relative to Aβ1-42 alone at that time-point. The light-colored bars represent the 6 h reactions while the dark-colored bars represent the 24 h reaction.

REFERENCES

1. Eisenberg, D., and Jucker, M. (2012) The amyloid state of proteins in human diseases. Cell 148, 1188 –1203
2. Sunde, M., Serpell, L. C., Bartlam, M., Fraser, P. E., Pepys, M. B., and Blake, C. C. (1997) Common core structure of amyloid fibrils by synchrotron X-ray diffraction. J. Mol. Biol. 273, 729 –739
3. Rodriguez, J. A., Ivanova, M. I., Sawaya, M. R., Cascio, D., Reyes, F. E., Shi, D., Sangwan, S., Guenther, E. L., Johnson, L. M., Zhang, M., Jiang, L., Arbing, M. A., Nannenga, B. L., Hattne, J., Whitelegge, J., et al. (2015) Structure of the toxic core of α-synuclein from invisible crystals. Nature 525, 486 – 490
4. Cooper, G. J., Willis, A. C., Clark, A., Turner, R. C., Sim, R. B., and Reid, K. B. (1987) Purification and characterization of a peptide from amyloid- rich pancreases of type 2 diabetic patients. Proc. Natl. Acad. Sci. U.S.A. 84, 8628 – 8632
5. Westermark, P., Wernstedt, C., Wilander, E., Hayden, D. W., O'Brien, T. D., and Johnson, K. H. (1987) Amyloid fibrils in human insulinoma and islets of Langerhans of the diabetic cat are derived from a neuropeptide- like protein also present in normal islet cells. Proc. Natl. Acad. Sci. U.S.A. 84, 3881–3885
6. Morales, R., Moreno-Gonzalez, I., and Soto, C. (2013) Cross-Seeding of misfolded proteins: implications for etiology and pathogenesis of protein misfolding diseases. PLoS Pathog. 9, e1003537
7. Guo, J.-P., Arai, T., Miklossy, J., and McGeer, P.L.(2006)Aβ and tau form soluble complexes that may promote self aggregation of both into the insoluble forms observed in Alzheimer's disease. Proc. Natl. Acad. Sci. U.S.A. 103, 1953–1958

8. Uéda, K., Fukushima, H., Masliah, E., Xia, Y., Iwai, A., Yoshimoto, M., Otero, D. A., Kondo, J., Ihara, Y., and Saitoh, T. (1993) Molecular cloning of cDNA encoding an unrecognized component of amyloid in Alzheimer disease. Proc. Natl. Acad. Sci. U.S.A. 90, 11282–11286
9. Buxbaum, J. N., Ye, Z., Reixach, N., Friske, L., Levy, C., Das, P., Golde, T., Masliah, E., Roberts, A. R., and Bartfai, T. (2008) Transthyretin protects Alzheimer's mice from the behavioral and biochemical effects of Aβ toxicity. Proc. Natl. Acad. Sci. U.S.A. 105, 2681–2686
10. Westermark, P., Li, Z.C., Westermark, G.T., Leckström, A., and Steiner, D. F. (1996) Effects of beta cell granule components on human islet amyloid polypeptide fibril formation. FEBS Lett. 379, 203–206
11. Wiltzius, J. J., Sievers, S. A., Sawaya, M. R., and Eisenberg, D. (2009) Atomic structures of IAPP (amylin) fusions suggest a mechanism for fibrillation and the role of insulin in the process. Protein Sci. 18, 1521–1530
12. Oskarsson, M. E., Paulsson, J. F., Schultz, S. W., Ingelsson, M., Westermark, P., and Westermark, G. (2015) In vivo seeding and cross-seeding of localized amyloidosis. Am. J. Pathol. 185, 834 – 846
13. Kapurniotu, A.(2001)Amyloidogenicity and cytotoxicity of islet amyloid polypeptide. Biopolymers 60, 438 – 459
14. Andreetto, E., Yan, L. M., Tatarek-Nossol, M., Velkova, A., Frank, R., and Kapurniotu, A. (2010) Identification of hot regions of the Aβ-IAPP interaction interface as high-affinity binding sites in both cross- and self-association. Angew. Chem. Int. Ed. Engl. 49, 3081–3085

15. Hu, R., Zhang, M., Chen, H., Jiang, B., and Zheng, J. (2015) Cross-seeding interaction between β-amyloid and human islet amyloid polypeptide. ACS Chem. Neurosci. 6, 1759 –1768
16. O'Nuallain, B., Williams, A. D., Westermark, P., and Wetzel, R. (2004) Seeding specificity in amyloid growth induced by heterologous fibrils. J. Biol. Chem. 279, 17490 –17499
17. Andreetto, E., Malideli, E., Yan, L. M., Kracklauer, M., Farbiarz, K., Ta- tarek-Nossol, M., Rammes, G., Prade, E., Neumüller, T., Caporale, A., Spanopoulou, A., Bakou, M., Reif, B., and Kapurniotu, A. (2015) A hot- segment-based approach for the design of cross-amyloid interaction surface mimics as inhibitors of amyloid self-assembly. Angew. Chem. Int. Ed. Engl. 54, 13095–13100
18. Moreno-Gonzalez, I., Edwards, G., III, Salvadores, N., Shahnawaz, M., Diaz-Espinoza, R., and Soto, C. (2017) Molecular interaction between type 2 diabetes and Alzheimer's disease through cross-seeding of protein misfolding. Mol. Psychiatry. 22, 1327–1334
19. Janson, J., Laedtke, T., Parisi, J.E., O'Brien, P., Petersen, R.C., and Butler, P. C. (2004) Increased risk of type 2 diabetes in Alzheimer disease. Diabetes. 53, 474 – 481
20. Miklossy, J., Qing, H., Radenovic, A., Kis, A., Vileno, B., Làszló, F., Miller, L., Martins, R. N., Waeber, G., Mooser, V., Bosman, F., Khalili, K., Darbinian, N., and McGeer, P. L. (2010) β amyloid and hyperphosphorylated tau deposits in the pancreas in type 2 diabetes. Neurobiol. Aging 31, 1503–1515

21. Peila, R., Rodriguez, B. L., Launer, L. J., and Honolulu-Asia Aging Study (2002) Type 2 diabetes, APOE gene, and the risk for dementia and related pathologies. Diabetes 51, 1256 –1262
22. Mukherjee, A., Morales-Scheihing, D., Butler, P. C., and Soto, C. (2015) Type 2 diabetes as a protein misfolding disease. Trends Mol. Med. 21, 439 – 449
23. Akter, K., Lanza, E. A., Martin, S. A., Myronyuk, N., Rua, M., and Raffa, R. B. (2011) Diabetes mellitus and Alzheimer's disease: shared pathology and treatment? Br. J. Clin. Pharmacol. 71, 365–376
24. Lee, S. C., Hashim, Y., Li, J. K., Ko, G. T., Critchley, J. A., Cockram, C. S., and Chan, J. C. (2001) The islet amyloid polypeptide (amylin) gene S20G mutation in Chinese subjects: evidence for associations with type 2 diabetes and cholesterol levels. Clin. Endocrinol. 54, 541–546
25. Morita, S., Sakagashira, S., Ueyama, M., Shimajiri, Y., Furuta, M., and Sanke, T. (2011) Progressive deterioration of insulin secretion in Japanese type 2 diabetic patients in comparison with those who carry the S20G mutation of the islet amyloid polypeptide gene: A long-term follow-up study. J. Diabetes Investig. 2, 287–292
26. Sakagashira, S., Sanke, T., Hanabusa, T., Shimomura, H., Ohagi, S., Kumagaye, K. Y., Nakajima, K., and Nanjo, K. (1996) Missense mutation of amylin gene (S20G) in Japanese NIDDM patients. Diabetes 45, 1279 –1281 Medline
27. Lührs, T., Ritter, C., Adrian, M., Riek-Loher, D., Bohrmann, B., Döbeli, H., Schubert, D., and Riek, R. (2005) 3D structure of Alzheimer's amyloid- β (1– 42) fibrils. Proc. Natl. Acad. Sci. U.S.A. 102, 17342–17347

28. Wälti, M.A., Ravotti, F., Arai, H., Glabe, C.G., Wall, J.S., Böckmann, A., Güntert, P., Meier, B. H., and Riek, R. (2016) Atomic-resolution structure of a disease-relevant Aβ (1–42) amyloid fibril. Proc. Natl. Acad. Sci. U.S.A. 113, E4976 –E4984
29. Scheidt, H. A., Morgado, I., Rothemund, S., and Huster, D.(2012)Dynamics of amyloid β fibrils revealed by solid-state NMR. J. Biol. Chem. 287, 2017–2021
30. Colvin, M. T., Silvers, R., Ni, Q. Z., Can, T. V., Sergeyev, I., Rosay, M., Donovan, K. J., Michael, B., Wall, J., Linse, S., and Griffin, R. G. (2016) Atomic resolution structure of monomorphic Aβ42 amyloid fibrils. J. Am. Chem. Soc. 138, 9663–9674
31. Colletier, J.P., Laganowsky, A., Landau, M., Zhao, M., Soriaga, A. B., Goldschmidt, L., Flot, D., Cascio, D., Sawaya, M. R., and Eisenberg, D. (2011) Molecular basis for amyloid-polymorphism. Proc. Natl. Acad. Sci. U.S.A. 108, 16938 –16943
32. Fonte, V., Dostal, V., Roberts, C. M., Gonzales, P., Lacor, P. N., Velasco, P. T., Magrane, J., Dingwell, N., Fan, E. Y., Silverman, M. A., Stein, G. H., and Link, C. D. (2011) A glycine zipper motif mediates the formation of toxic β-amyloid oligomers in vitro and in vivo. Mol. Neurodegener. 6, 61
33. Harmeier, A., Wozny, C., Rost, B. R., Munter, L. M., Hua, H., Georgiev, O., Beyermann, M., Hildebrand, P. W., Weise, C., Schaffner, W., Schmitz, D., and Multhaup, G. (2009) Role of amyloid-β glycine 33 in oligomerization, toxicity, and neuronal plasticity. J. Neurosci. 29, 7582–7590
34. Kanski, J., Varadarajan, S., Aksenova, M., and Butterfield, D. A.(2002) Role of glycine-33 and methionine-35 in Alzheimer's amyloid β-peptide 1– 42- associated oxidative stress and neurotoxicity. Biochim. Biophys. Acta 1586, 190 –198

35. Krotee, P., Rodriguez, J. A., Sawaya, M. R., Cascio, D., Reyes, F. E., Shi, D., Hattne, J., Nannenga, B. L., Oskarsson, M. E., Philipp, S., Griner, S., Jiang, L., Glabe, C. G., Westermark, G. T., Gonen, T., et al. (2017) Atomic structures of fibrillar segments of hIAPP suggest tightly mated β-sheets are important for cytotoxicity. Elife 6, e19273
36. Hattne, J., Reyes, F. E., Nannenga, B. L., Shi, D., de la Cruz, M. J., Leslie, A. G., and Gonen, T. (2015) MicroED data collection and processing. Acta Crystallogr. A Found. Adv. 71, 353–360
37. Liu, S., Hattne, J., Reyes, F. E., Sanchez-Martinez, S., Jasondela Cruz, M., Shi, D., and Gonen, T. (2017) Atomic resolution structure determination by the cryo-EM method MicroED. Protein Sci. 26, 8–15
38. Nannenga, B. L., Shi, D., Leslie, A. G. W., and Gonen, T. (2014) High- resolution structure determination by continuous-rotation data collection in MicroED. Nat. Methods 11, 927–930
39. Shi, D., Nannenga, B. L., Iadanza, M. G., and Gonen, T. (2013) Three- dimensional electron crystallography of protein microcrystals. Elife 2, e01345
40. Lorenzo, A., and Yankner, B. A. (1996) Amyloid fibril toxicity in Alzheimer's disease and diabetes. Ann. N.Y. Acad. Sci. 777, 89–95
41. Olmsted, J. B., Carlson, K., Klebe, R., Ruddle, F., and Rosenbaum, J. (1970) Isolation of microtubule protein from cultured mouse neuroblastoma cells. Proc. Natl. Acad. Sci. U.S.A. 65, 129 –136
42. Mosmann, T. (1983) Rapid colorimetric assay for cellular growth and survival: application to proliferation and cytotoxicity assays. J. Immunol. Methods. 65, 55– 63

43. Liu, Y., Peterson, D. A., Kimura, H., and Schubert, D. (1997) Mechanism of cellular 3-(4, 5-dimethylthiazol-2-yl)-2, 5-diphenyltetrazolium bromide (MTT) reduction. J. Neurochem. 69, 581–593 Medline

44. Pike, C. J., Walencewicz-Wasserman, A. J., Kosmoski, J., Cribbs, D. H., Glabe, C. G., and Cotman, C. W. (1995) Structure-activity analyses of β-amyloid peptides: contributions of the β 25–35 region to aggregation and neurotoxicity. J. Neurochem. 64, 253–265 Medline

45. Yankner, B. A., Duffy, L. K., and Kirschner, D. A.(1990) Neurotrophicand neurotoxic effects of amyloid β protein: reversal by tachykinin neuropeptides. Science. 250, 279 –282

46. Saelices, L., Johnson, L. M., Liang, W. Y., Sawaya, M. R., Cascio, D., Ruchala, P., Whitelegge, J., Jiang, L., Riek, R., and Eisenberg, D. S. (2015) Uncovering the mechanism of aggregation of human transthyretin. J. Biol. Chem. 290, 28932–28943

47. Sievers, S. A., Karanicolas, J., Chang, H. W., Zhao, A., Jiang, L., Zirafi, O., Stevens, J. T., Münch, J., Baker, D., and Eisenberg, D. (2011) Structure- based design of non-natural amino-acid inhibitors of amyloid fibril forma- tion. Nature 475, 96 –100

48. Soragni, A., Janzen, D. M., Johnson, L. M., Lindgren, A. G., Thai-Quynh Nguyen, A., Tiourin, E., Soriaga, A. B., Lu, J., Jiang, L., Faull, K. F., Pellegrini, M., Memarzadeh, S., and Eisenberg, D. S. (2016) A designed inhibitor of p53 aggregation rescues p53 tumor suppression in ovarian carcinomas. Cancer Cell 29, 90 –103

49. Miller, S. M., Simon, R. J., Ng, S., Zuckermann, R. N., Kerr, J. M., and Moos, W. H. (1995) Comparison of the proteolytic susceptibilities of homologous L-amino acid, D-amino

acid, and N-substituted glycine peptide and peptoid oligomers. Drug Dev. Res. 35, 20 –32

50. Hatami, A., Albay, R., 3rd, Monjazeb, S., Milton, S., and Glabe, C.(2014) Monoclonal antibodies against Aβ42 fibrils distinguish multiple aggregation state polymorphisms in vitro and in Alzheimer disease brain. J. Biol. Chem. 289, 32131–32143
51. Morales, R., Duran-Aniotz, C., Diaz-Espinoza, R., Camacho, M. V., and Soto, C. (2012) Protein misfolding cyclic amplification of infectious prions. Nat. Protoc. 7, 1397–1409
52. Ross, C. D., McCarty, B. R., Hamilton, M., Ben-Hur, A., and Ross, E. D.(2009) A promiscuous prion: efficient induction of [URE3] prion formation by heterologous prion domains. Genetics 183, 929 –940
53. Tjernberg, L. O., Näslund, J. , Lindqvist, F., Johansson, J., Karlström, A. R., Thyberg, J., Terenius, L., and Nordstedt, C. (1996) Arrest of β-amyloid fibril formation by a pentapeptide ligand. J. Biol. Chem. 271, 8545– 8548
54. Shi, D., Nannenga, B. L., delaCruz, M. J., Liu, J., Sawtelle, S., Calero, G., Reyes, F. E., Hattne, J., and Gonen, T. (2016) The collection of MicroED data for macromolecular crystallography. Nat. Protoc. 11, 895–904
55. Kabsch, W.(2010)XDS.ActaCrystallogr.DBiol.Crystallogr.66, 125–132
56. McCoy, A. J.(2007) Solving structures of protein complexes by molecular replacement with Phaser. Acta Crystallogr. D Biol. Crystallogr. 63, 32– 41
57. Emsley, P., and Cowtan, K.(2004) Coot: model-building tools for molecular graphics. Acta Crystallogr. D Biol. Crystallogr. 60, 2126 –2132

58. McCoy, A. J., Grosse-Kunstleve, R. W., Storoni, L. C., and Read, R. J.(2005) Likelihood-enhanced fast translation functions. Acta Crystallogr. D Biol. Crystallogr. 61, 458 – 464
59. Diederichs, K., and Karplus, P. A. (2013) Better models by discarding data? Acta Crystallogr. D Biol. Crystallogr. 69, 1215–1222
60. Collaborative Computational Project, Number 4 (1994) The CCP4 suite: programs for protein crystallography. Acta Crystallogr. D Biol. Crystallogr. 50, 760 –763
61. Lee, B., and Richards, F. M. (1971) The interpretation of protein structures: estimation of static accessibility. J. Mol. Biol. 55, 379 – 400
62. Connolly, M. L. (1983) Solvent-accessible surfaces of proteins and nucleic acids. Science 221, 709 –713
63. Lawrence, M. C., and Colman, P. M. (1993) Shape complementarity at protein-protein interfaces. J. Mol. Biol. 234, 946 –950
64. Richards, F. M. (1977) Areas, volumes, packing, and protein structure. Annu. Rev. Biophys. Bioeng. 6, 151–176
65. Kabsch, W. (1976) A solution for the best rotation to relate two sets of vectors. Acta Crystallogr. A 32, 922–923
66. Kyte, J., and Doolittle, R. F. (1982) A simple method for displaying the hydropathic character of a protein. J. Mol. Biol. 157, 105–132
67. Thompson, M. J., Sievers, S. A., Karanicolas, J., Ivanova, M. I., Baker, D., and Eisenberg, D. (2006) The 3D profile method for identifying fibril-forming segments of proteins. Proc. Natl. Acad. Sci. U.S.A. 103, 4074 – 4078

68. Kuhlman, B., Dantas, G., Ireton, G. C., Varani, G., Stoddard, B. L., and Baker, D. (2003) Design of a novel globular protein fold with atomic-level accuracy. Science 302, 1364-1368

69. Laganowsky, A., Liu, C., Sawaya, M. R., Whitelegge, J. P., Park, J., Zhao, M., Pensalfini, A., Soriaga, A. B., Landau, M., Teng, P. K., Cascio, D., Glabe, C., and Eisenberg, D. (2012) Atomic view of a toxic amyloid small oligomer. Science 335, 1228-1231

70. Saelices, L., Johnson, L. M., Liang, W. Y., Sawaya, M. R., Cascio, D., Ruchala, P., Whitelegge, J., Jiang, L., Riek, R., and Eisenberg, D. S. (2015) Uncovering the mechanism of aggregation of human transthyretin. *J. Biol. Chem.* **290**, 28932–28943

71. Kayed, R., Head, E., Sarsoza, F., Saing, T., Cotman, C. W., Necula, M., Margol, L., Wu, J., Breydo, L., Thompson, J. L., Rasool, S., Gurlo, T., Butler, P., and Glabe, C. G. (2007) Fibril specific, conformation dependent antibodies recognize a generic epitope common to amyloid fibrils and fibrillar oligomers that is absent in prefibrillar oligomers. *Mol. Neurodegener.* **2**, 18

72. Wobst, H. J., Sharma, A., Diamond, M. I., Wanker, E. E., and Bieschke, J. (2015) The green tea polyphenol (−)-epigallocatechin gallate prevents the aggregation of tau protein into toxic oligomers at substoichiometric ratios. *FEBS Lett.* **589**, 77–83

73. Bieschke, J., Russ, J., Friedrich, R. P., Ehrnhoefer, D. E., Wobst, H., Neugebauer, K., and Wanker, E. E. (2010) EGCG remodels mature alpha-synuclein and amyloid-beta fibrils and reduces cellular toxicity. *Proc. Natl. Acad. Sci. U. S. A.* **107**, 7710–5